

**Reactivity of Targeted Covalent Inhibitor Fragments and Transition Metal-Catalyzed
Alkene Functionalization Reactions**

by

Tuğçe Gülşen Erbay

Bachelor of Science, Boğaziçi University, 2012

Master of Science, Boğaziçi University, 2014

Submitted to the Graduate Faculty of the
Dietrich School of Arts and Sciences in partial fulfillment
of the requirements for the degree of
Doctor of Philosophy

University of Pittsburgh

2021

UNIVERSITY OF PITTSBURGH

DIETRICH SCHOOL OF ARTS AND SCIENCES

This dissertation was presented

by

Tuğçe Gülşen Erbay

It was defended on

June 30, 2021

and approved by

Paul Floreancig, Professor, Chemistry, University of Pittsburgh

Karl Johnson, Professor, Chemical and Petroleum Engineering, University of Pittsburgh

Kazunori Koide, Professor, Chemistry, University of Pittsburgh

Kay Brummond, Professor, Chemistry, University of Pittsburgh

Peng Liu, Associate Professor, Chemistry, University of Pittsburgh

Copyright © by Tuğçe Gülşen Erbay

2021

Reactivity of Targeted Covalent Inhibitor Fragments and Transition Metal-Catalyzed Alkene Functionalization Reactions

Tuğçe Gülşen Erbay, PhD

University of Pittsburgh, 2021

Density functional theory (DFT) is a convenient and robust tool that has been widely applied to explore reaction mechanisms, thermodynamics, and kinetics of various organic reactions, many of which are catalyzed by transition metal complexes. The insights gained through DFT calculations provide chemists with critical information for the development of new organic reactions to achieve novel synthetic transformations. This thesis describes the applications of DFT calculations to study thio-Michael addition, Cu-catalyzed alkene hydroboration, and Pd-catalyzed alkene functionalization reactions.

Kinase activity can be modulated reversibly or irreversibly by reactions of the targeted covalent inhibitors with the nucleophilic residues in protein active sites. Thiol reactivity studies were performed to support α -methylene- γ -lactams as a tunable surrogate for the highly reactive α -methylene- γ -lactones. A series of *N*-substituted α -methylene- γ -lactams with different electronic properties were synthesized and the reactivity of the α -methylene towards glutathione was determined via mass spectrometry. DFT calculations were performed to identify a robust method for the accurate prediction of the reactivity difference between covalent modifier fragments. These studies revealed that the M06-2X functional with SMD solvation model and methyl thiolate as a model nucleophile reliably predicts the relative reactivities of the α -

methylene- γ -lactams, and quasiharmonic approximations improve the agreement between the experiment and computation.

In the following chapter, DFT calculations were applied to study the Cu-catalyzed hydroboration of benzyldenecyclobutanes and benzyldenecyclopropanes that tolerates a wide variety of heterocycles prevalent in clinical and preclinical drug development, giving access to valuable synthetic intermediates. Computational studies provided insight into how the rigidity and steric environment of the bisphosphine ligands influence the relative activation energies of β -carbon elimination versus protodecupration from the benzylcopper intermediate. Energy decomposition analysis calculations revealed that electron-deficient *P*-aryl groups on the bisphosphine ligands enhance the T-shaped π/π interactions with the substrate and stabilize the migratory insertion transition state.

Lastly, two Pd-catalyzed, transient directing group-mediated alkene functionalization reactions, an enantioselective Heck hydroarylation and a Pd-catalyzed C–H activation that achieves atropisomeric synthesis of 1,3-dienes are presented. The reaction mechanisms, rate- and selectivity-determining steps, and origins of enantioinduction and atroposelectivity were studied using DFT calculations.

Table of Contents

1.0 Introduction.....	1
2.0 Thiol Reactivity of <i>N</i>-Aryl α-Methylene-γ-lactams: A Reactive Group for Targeted Covalent Inhibitor Design.....	7
2.1 Introduction	7
2.2 Synthesis of <i>N</i>-aryl α-Methylene-γ-lactams	13
2.3 Experimental Determination of Reaction Rates for the Conjugate Addition of GSH to α-Methylene-γ-lactams 5a–m.....	16
2.4 Correlation of the GSH Reactivity of the <i>N</i>-Aryl α-Methylene-γ-lactams with the Hammett Parameters, ^1H NMR, ^{13}C NMR Shifts and IR Frequencies.....	18
2.4.1 Computational Methods	21
2.4.2 Results and Discussion.....	22
2.4.2.1 <i>Syn</i> vs <i>Anti</i> Addition of the Thiolate and the Impact of Solvation Models on the Geometry	22
2.4.2.2 Impact of the Nucleophile on the Computed Activation Barriers of GSH Addition and Calculation Accuracy Determination	24
2.4.2.3 Impact of the DFT Functional and Solvation Models on Computed Activation Barriers and the Calculation Accuracy	27
2.4.2.4 Coupled Cluster Calculations.....	33
2.5 Conclusions	35
2.6 Synthesis and Characterization of Compounds.....	36
2.6.1 General Information	36

2.6.2 Synthesis of the α -Methylene- γ -lactam (3)	37
2.6.3 General Procedure: <i>N</i> -Arylation of Lactams 5a–5m	40
3.0 Cu-Catalyzed Hydroboration of Benzyldenecyclopropanes and Benzyldenecyclobutanes	48
3.1 Introduction	49
3.2 Computational Methods	53
3.3 Ligand Effects on the Pathway Selectivity of Cu-Catalyzed Hydroboration of Benzyldenecyclopropanes	54
3.4 The Influence of the Ligand–Substrate Interactions on the Product Selectivity and Rates of Cu-Catalyzed Hydroboration of Benzyldenecyclobutanes	64
3.4.1 Comparison of BCB to BCP	66
3.4.2 Origins of Ligand and Substrate Effects on Reactivity	72
3.5 Conclusions	75
4.0 Transient Directing Group Strategies in Pd-Catalyzed Functionalization of Alkenes	77
4.1 Introduction	77
4.2 A Transient-Directing-Group Strategy that Enables Enantioselective Reductive Heck Hydroarylation of Alkenes	81
4.2.1 Computational Methods	85
4.2.2 Mechanism of C–H Activation	85
4.2.3 Origin of Enantioselectivity	91
4.2.4 Conclusions	93

4.3 C(alkenyl)–H Activation via Transient-Directing-Group Strategy for Atropoisomeric Synthesis	94
4.3.1 Computational Methods	96
4.3.2 Mechanism of C–H Activation and the Origins of the Atroposelectivity	96
4.3.3 Conclusions	103
Appendix A ¹³ C and ¹ H NMR Shifts (ppm) of <i>N</i> -Aryl Acrylamides	104
Appendix B DFT-Calculated and Experimentally-Determined Barriers of Thiolate Additions to the α -Methylene- γ -lactams.....	105
Appendix C IR Spectra of <i>N</i> -Aryl α -Methylene- γ -Lactams.....	108
Bibliography	121

List of Tables

Table 2.1. Coupling of aryl iodides with 3-methylene-2-pyrrolidinone (3) affording N-aryl α -methylene- γ -lactams 5a–m.	15
Table 2.2. Measured rates of GSH addition, derived half-lives, and spectroscopic data.	17
Table 2.3. Summary of the results of the distortion-interaction analysis.	26
Table 2.4. Comparison of the activation electronic energies calculated with cc-pVDZ-F12 and cc-pVTZ-F12 basis sets.	35
Table 3.1. Summary of ligand optimization with representative substrates.	55
Table 3.2. Summary of ligand optimization with representative BCB substrate 1d.	64

List of Figures

Figure 2.1. Examples of a) drugs and b) natural products equipped with covalent reactive groups, and c) α -methylene- γ -lactams.	9
Figure 2.2. Base-catalyzed thio-Michael addition to α,β -unsaturated carbonyl compounds.	10
Figure 2.3. Summary of the experimental and computational studies on the GSH reactivity of the <i>N</i> -aryl α -methylene- γ -lactams.	13
Figure 2.4. The relationship of Hammett parameters σ_p^- , σ_m or σ_p with the rate of GSH addition to <i>N</i> -aryl α -methylene- γ -lactams with a) <i>para</i> - and <i>ortho</i> -, b) <i>meta</i> -, and c) <i>para</i> - and <i>ortho</i> -substitutions on the aryl ring.....	19
Figure 2.5. Correlation of $\log k_{\text{GSH}}$ with a) ^{13}C NMR and b) ^1H NMR shifts.	20
Figure 2.6. Correlations of the a) ^1H NMR shift (ppm) of $\text{H}^{1\beta}$, b) ^{13}C NMR shift (ppm) of the carbonyl carbon, and c) IR resonances (cm^{-1}) of the carbonyl group of the <i>N</i> -aryl lactams to experimentally-determined values of $\log k_{\text{GSH}}$. Compound 5g (<i>p</i> -NMe ₂) is excluded due to lack of rate data.	21
Figure 2.7. <i>syn</i> and <i>anti</i> transition states of the thio-Michael addition of the methyl thiolate to the <i>N</i> -phenyl α -methylene- γ -lactam 5a.	23
Figure 2.8. Transition states of the thio-Michael additions to the <i>N</i> -phenyl lactam 5a with methyl thiolate a) calculated using PCM solvation model in water, and b) in the gas phase.....	24

Figure 2.9. Transition state structures of the thio-Michael additions to the <i>N</i> -phenyl α -methylene- γ -lactam 5a with a) cysteamine thiolate, b) with glutathione (-2 charged with both a thiolate and carboxylate) as the nucleophile.	25
Figure 2.10. Correlation of the a) DFT-M06-2X-SMD calculated reactivity and b) DFT-M06-2X-PCM calculated reactivity to the experimentally-determined reactivity (left), and the correlation of the DFT-calculated enthalpies to the experimentally-determined reactivity (right).	29
Figure 2.11. Correlation of the DFT-M06-2X-SMD-calculated reactivity to the experimentally-determined reactivity (left) and the correlation of the DFT-calculated enthalpies to the experimentally-determined reactivity (right).	30
Figure 2.12. Correlation of the a) DFT-B3LYP-SMD-calculated reactivity and b) DFT-B3LYP-PCM-calculated reactivity to the experimentally-determined reactivity (left), and the correlation of the DFT-calculated enthalpies to the experimentally-determined reactivity (right).	31
Figure 2.13. Correlation of the DFT-M062X-SMD-calculated reactivity to the experimentally-determined reactivity (left) and the correlation of the DFT-calculated enthalpies to the experimentally-determined reactivity (right).	32
Figure 2.14. Correlation of the CC and DFT-calculated electronic energies of activation for the methyl thiolate addition to <i>N</i> -aryl lactams.	34
Figure 3.1. a) Biologically relevant cyclopropane- and cyclobutane-containing molecules. b) Tertiary boronic esters are useful in synthetic chemistry to construct C–C and C–Heteroatom bonds. Adapted with permission from Acc. Chem. Res. 2014, 47, 3174–3183. Copyright 2014 American Chemical Society.	50

Figure 3.2. a) Tuning of ligand sphere enables pathway selectivity in Cu-catalyzed hydroboration of BCPs. b) Ligand–substrate interaction effects on the rates of migratory insertion in BCBs are elaborated using EDA methods.	51
Figure 3.3. Ligand effects on the β -carbon elimination transition states.....	61
Figure 3.4. Alternative β -carbon elimination transition state with BINAP-supported catalyst.	62
Figure 3.5. Ligand effects on the protodecupration transition states.	63
Figure 3.6. Comparison of a) β -carbon elimination and b) protodecupration transition states of BCB and BCPs.....	68
Figure 3.7. Protodecupration (left) and β -carbon elimination (right) transition states with 4- CF_3 -dppbz ligand.	70
Figure 3.8. Summary of the a) ligand–substrate interaction effects on the reactivity of migratory insertion b) ligand effects, and c) substrate effects (L = 4-F-dppbz).	73
Figure 3.9. Edge-ring and face-ring interactions.	74
Figure 4.1. General comparison of auxiliary-based and TDG approaches for alkene functionalization. b) Pioneering examples of using chiral TDGs in transition metal catalysis.	79
Figure 4.2. a) General depiction of a reductive Heck reaction facilitated by an in situ formed imine using a chiral TDG strategy. b) Catalytic C(alkenyl)–H activation enabled by TDG.....	81
Figure 4.3. Optimized reaction conditions, X-ray crystal structure, deuterium incorporation and control experiments.	84
Figure 4.4. Oxidative addition transition states.	90

Figure 4.5. Decarboxylation transition states.....	90
Figure 4.6. Origin of enantioselectivity in migratory insertion.	92
Figure 4.7. a) Optimized reaction conditions, b) Synthesis of atropisomeric 1,3-diene 5, c) TDG and the acids used in reactions, and d) X-ray crystal structure of 5, e) Stoichiometric reaction to form the palladacycle complex.	95
Figure 4.8. Isomers of the π -alkene reactant complex with different π -facial selectivity....	98
Figure 4.9. Comparison of the C–H activation transition states with the Pd bound to the opposite faces of the alkene, and summary of distortion-interaction analyses of the two transition states.	101
Figure 4.10. Migratory insertion transition states with <i>tert</i> -butyl acrylate.	102

List of Schemes

Scheme 2.1. Synthesis of 3-methylene-2-pyrrolidinone (3).	13
Scheme 3.1. Proposed reaction mechanism for hydroboration of benzylidenecyclopropanes.	56
Scheme 3.2. Computed reaction energy profiles of the hydroboration of benzylidenecyclopropane 1 with dppe (top)- and (S)-BINAP (bottom)-supported Cu catalysts.....	58
Scheme 3.3. Alternative diastereomeric TS with the (S)-BINAP-supported Cu catalyst. ...	60
Scheme 3.4. Summary of pathway selectivity.....	60
Scheme 3.5. Proposed reaction mechanism of hydroboration of benzylidenecyclobutanes.	65
Scheme 3.6. Reaction energy profile of the dppe-supported Cu-catalyzed hydroboration of 1d.	66
Scheme 3.7. Reaction energy profile of the 4-CF ₃ -dppbz-supported-Cu-catalyzed hydroboration of 1d.	69
Scheme 3.8. Reaction energy profile of the dppbz (top) and 4-F-dppbz (bottom)-supported- Cu-catalyzed hydroboration of 1d.....	71
Scheme 4.1. State of the art in the asymmetric hydroarylation of styrenes.	82
Scheme 4.2. Proposed catalytic cycle.....	86
Scheme 4.3. Calculated reaction energy profile of hydroarylation of alkene 1a to form the (S)-enantiomer of the product.....	87
Scheme 4.4. Calculated reaction energy profile of hydroarylation of alkene 1a to form the (R)-enantiomer of the product.	89

Scheme 4.5. Proposed catalytic cycle.....	97
Scheme 4.6. Calculated reaction energy profile of C–H activation of the (<i>Z</i>)-alkene 1 with 3,4,5-trifluorobenzoic acid (acid 1) with <i>tert</i> -butyl acrylate as the coupling partner.	100

1.0 Introduction

Density functional theory (DFT) is a robust tool to study reaction mechanisms, thermodynamics, and kinetics, and has been used extensively to study a wide array of organic reactions and transition metal-catalyzed reactions. Understanding the reaction pathways where the isolation and characterization of intermediates are not possible, especially in organometallic reactions, and the origin of effects of ligands and substrates have been proven useful and contributed to the design of new reactions. Computational studies can provide a detailed understanding of the complex reaction mechanisms and reveal the origin of reactivity and selectivity. In this thesis, state-of-the-art DFT methods are applied to various organic and transition metal-catalyzed reactions.

Recent developments of modern DFT methods allow calculations of reaction thermochemistry and kinetics with reasonable chemical accuracy. While it is one of the holy grails of computational chemistry to achieve such high accuracy in calculations, DFT has been shown to perform well for a wide range of properties, such as reaction thermodynamics and kinetics, geometries, inter- and intramolecular interactions. However, the application of DFT to the rate and selectivity predictions of real-life chemical problems requires a thorough understanding of the reaction mechanism and the reliability of chosen DFT methods in the system under investigation. To assess the accuracy and robustness of DFT methods in the application to a particular type of system, careful benchmark studies against experimental data and higher-level computational results, such as those from coupled cluster (CC) theory calculations, are needed. The coupled cluster methods can achieve chemical accuracy (within 1 kcal/mol for energetics). However, practical applications of the coupled cluster methods are limited to relatively small molecules

because they are computationally highly demanding, and as the systems under investigation become larger, this requirement increases exponentially. Alternatively, DFT is more efficient and it can be applied to systems with much greater size. Therefore, assessing the performance of DFT methods can predict the reliability of DFT methods and identify the best-performing functionals and basis sets in these applications.

DFT methods have been widely applied to study the mechanisms and the effects of catalysts on reactivity and selectivity of transition metal-catalyzed reactions. Although non-covalent interactions between the ancillary ligand on transition metal catalyst and the substrate are well known and have been utilized to achieve a wide variety of transformations, computational methods to quantify the nature of non-covalent ligand–substrate interactions are rare. To date, various steric and electronic descriptors such as Sterimol parameters, Tolman’s electronic parameters (TEP), cone angles, ligand bite angles, buried volumes alongside steric models and quadrant diagram analyses have been used to rationalize ligand effects. Alternatively, energy decomposition analysis (EDA) calculations have been used to quantitatively describe the nature of catalyst–substrate interactions in transition states by dissecting the interaction energies into chemically meaningful terms.

DFT calculations have also been utilized to study the origin of chirality induction in transition metal-catalyzed enantioselective reactions. These calculations often rely on understanding the steric and other non-bonding interactions between the substrate and the chiral ligand based on the computed transition state structures. Quadrant diagram is a powerful tool for the analysis of the steric interactions with chiral ligands in the transition states. On the other hand, the realm of transition metal-catalyzed enantioselective reactions promoted by chiral directing groups is underexplored. It is surmised that the mode of asymmetric induction in reactions with

chiral directing groups can be fundamentally different from those with chiral ligands, especially in cases where the chiral center on the directing group is placed relatively far away from the new chiral center, suggesting that the enantioselectivity may not be simply controlled by steric repulsions, and other factors, such as the strain effects of the metallacycle intermediates, need to be probed using DFT calculations.

We performed a combined experimental and computational study on the thio-Michael addition to an α,β -unsaturated carbonyl, namely an α -methylene- γ -lactam, where the reactivity of the alkene is electronically tuned and used to react with a biological nucleophile and form a covalent bond. Incorporation of fragments that react with a targeted nucleophilic residue enabled development of successful drugs particularly for the treatment of cancer. In this study, we proposed the α -methylene- γ -lactam as a novel targeted covalent inhibitor fragment and demonstrated the tunable reactivity of the methylenyl group through substitution on the nitrogen of the lactam.

We synthesized *N*-arylated α -methylene- γ -lactams and determined their reactivity towards glutathione using liquid chromatography-mass spectroscopy (LC-MS) methods. While the thio-Michael addition is well known and various experimental protocols have been established to determine the reactivity towards biological nucleophiles, the DFT calculations in many of these studies lack the thorough consideration of a strategy, such that the DFT functional and solvation model that would accurately grasp the reactivity differences between the covalent inhibitor fragments, and the potential influence of the model nucleophile are not carefully considered. To address this, we performed DFT calculations of transition states of the nucleophilic additions to the α -methylene- γ -lactams with different functionals, solvation models, and model nucleophiles, and benchmarked the calculated barriers against the experimentally-determined reactivity data. We investigated the influence of the chosen DFT methods on the transition state geometries and

the calculated barriers, and examined the impact of different model nucleophiles on the predicted reactivity trends. We benchmarked the performance of various DFT methods against highly accurate coupled cluster (CC) methods. This is the first study that combines experimentally-determined reactivity, CC methods and DFT together to demonstrate the utility of DFT as a robust computational method for activation energy prediction, and identifies the most appropriate DFT functional and solvation model for the accurate prediction of the reactivity difference between covalent modifier fragments.

Next, a copper catalyzed hydroboration reaction of benzyldenecyclobutanes and benzyldenecyclopropanes is presented. Boronic ester is one of the most versatile functional groups in the organic synthesis. This reaction provides access to tertiary boronic esters that enables synthesis of molecules with strained cyclopropyl or cyclobutyl motifs relevant to drug research. We performed DFT calculations to understand the mechanism of hydroboration, to identify the rate-determining step of the reaction, and to explain the observed pathway selectivity. In addition, we aimed to elaborate on the ligand and substrate effects on the reactivity.

At the outset, we investigated the reaction energy profiles of hydroboration of benzyldenecyclopropanes with different bisphosphine-supported Cu catalysts that yielded significantly different products (alkenylboronates and cyclopropylboronic esters), which was interesting, as the commonly used steric and electronic parameters did not explain the ligand influence on the reaction outcome, that more complex steric and conformational factors were at play. Our detailed studies of the reaction energy profiles and elaborate structural analyses of the transition states revealed the factors that influenced the pathway selectivity.

Expanding the experimental methodology to benzyldenecyclobutanes yielded two different and interesting outcomes. First, the reaction did not lead to ring-opening products, even

though the ring strain energies of cyclopropane and cyclobutane are comparable. The reaction energy profiles, and analyses of transition state structures explained why the pathway selectivity is reversed to disfavor ring-opening in the hydroboration of benzyldenecyclobutanes.

Second, experimental kinetics studies demonstrated that the reaction rates were affected by modifications of the aryl groups on the ligands, and the aryl substituents on the substrate. We examined the DFT-calculated transition state geometries of the rate-determining step, and identified T-shaped π/π interactions, however, the underlying factors that led to the observed rate differences were still elusive. Using a ligand–substrate interaction model developed by our group and the Energy Decomposition Analysis (EDA) methods, it was possible to break the complex catalyst–substrate interactions down to their distortion, through-bond, and through-space energy components. Through-space interactions could be dissected further to reveal the non-covalent interactions, namely the electrostatic interaction, Pauli repulsion, dispersion interaction, intrafragment polarization, and interfragment charge transfer energies. This refined approach allowed us to pinpoint the exact sources of the observed reactivity changes. The insights we obtain through EDA contribute to the rational design of ligands and offer exciting opportunities to incorporate required substrate recognition motifs to boost reactivity.

The final chapter is focused on the transient directing group (TDG)-mediated Pd-catalyzed reactions. TDG strategies in organocatalysis have recently gained interest, and the computational studies on the additions to the carbon–carbon double bonds are very limited. In the first section of this chapter, the DFT studies on a remarkable enantioselective Heck hydroarylation is presented. The mechanisms of Heck-type hydroarylation reactions have been studied, however, the use of a TDG may change the rate- or selectivity-determining steps. Furthermore, the mode of enantioselective induction by the chiral TDG was unclear. Through computations, we explained

the asymmetric induction by the chiral TDG that could otherwise not been understood with experiment.

Last but not least, we explored a TDG-mediated Pd-catalyzed functionalization of a C(sp²)-H bond to access aryl-substituted 1,3-dienes substrates with high atroposelectivity. The C(sp²)-H activations with TDG-mediated transition metal catalysis are underexplored and challenging, considering the aforementioned challenges with the TDG strategy, and the rigidity and high strain of the C(sp²)-H bond activation transition states. We performed DFT calculations to understand the reaction mechanism and the origins of the observed atroposelectivity.

2.0 Thiol Reactivity of *N*-Aryl α -Methylene- γ -lactams: A Reactive Group for Targeted Covalent Inhibitor Design

Erbay, T. G., Dempe, D. P. Godugu, B., Liu, P., Brummond, K. M. “Thiol Reactivity of *N*-Aryl α -Methylene- γ -lactams: A Reactive Group for Targeted Covalent Inhibitor Design”. *J. Org. Chem.* **2021**, <https://doi.org/10.1021/acs.joc.1c01335>.

In this work, I synthesized the compounds, designed and carried out DFT calculations and analyzed the computational results. Rate experiments of the thiolate addition to the α -methylene- γ -lactams were performed by Daniel P. Dempe.

2.1 Introduction

Kinases play a key role in regulation of biological processes, and their dysfunction is associated with a variety of pathological conditions.¹ The therapeutic potential of targeting kinases has long been recognized, however an abundance of nucleophilic residues and the highly conserved binding pocket have made this challenging.²⁻³ Targeted covalent inhibitors (TCIs) have emerged as a way to selectively modulate the kinase activity by targeting the specific non-catalytic, accessible nucleophilic amino acids near the ATP binding pocket.⁴⁻⁶ The discovery of osimertinib, an epidermal growth factor receptor (EGFR) tyrosine kinase inhibitor (**Figure 2.1a**), represents a successful example of TCI development, such that an α,β -unsaturated acrylamide functionality installed on a non-covalent core provided the effective inhibition of the kinase activity via an irreversible thio-Michael addition coupled with specificity towards the binding site.⁷ However,

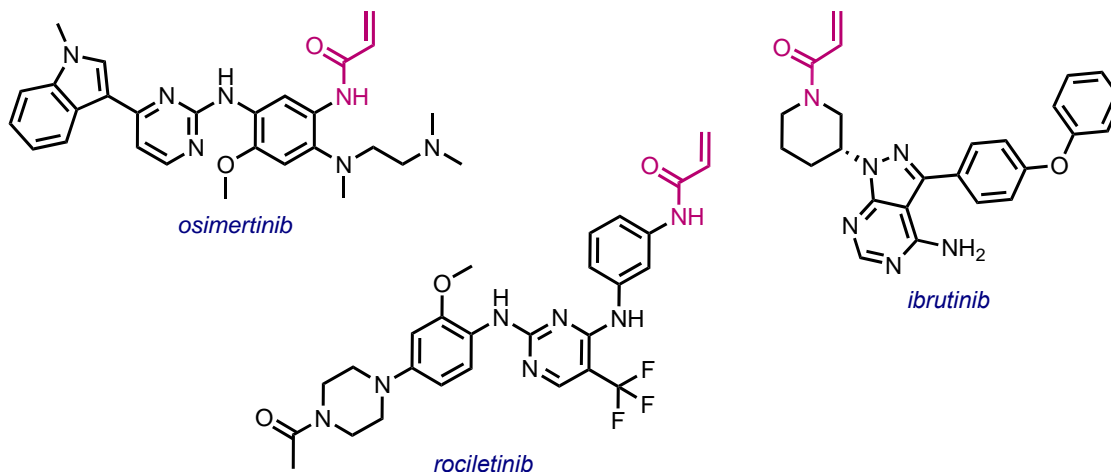
development of resistance to osimertinib has been reported recently, where an EGFR mutation of the targeted cysteine residue (Cys797) is replaced with a less nucleophilic serine prevents covalent bond formation and reduces drug efficacy,⁸⁻¹⁰ demonstrating the necessity to discover novel covalent modifiers. To overcome resistance that occurs due to point mutations and other TCI limitations, new reactive groups in combination with a deeper understanding of how the structure and electronics impact electrophilic reactivity are needed for designing more effective covalent ligands.

To date, α,β -unsaturated carbonyls are the most commonly used covalent reactive groups with *N*-aryl acrylamides (**Figure 2.1a**) having the most success, in part due to the readily tuned electrophilic reactivity towards thiols.⁶ Herein, we present α -methylene- γ -lactams (**Figure 2.1c**) as a tunable surrogate to Nature's warhead α -methylene- γ -lactone, which is a common motif in a large number of natural products (**Figure 2.1b**). The biological activity of natural products equipped with an α -methylene- γ -lactone is attributed to the electrophilic exocyclic methylene unit reacting via a Michael addition with biological nucleophiles.¹¹⁻¹² Several experimental and computational studies of the Michael addition reactivity of *N*-aryl acrylamides have been reported.¹³⁻¹⁵ On the other hand, reactivities of α -methylene- γ -lactams have not been investigated experimentally or computationally.

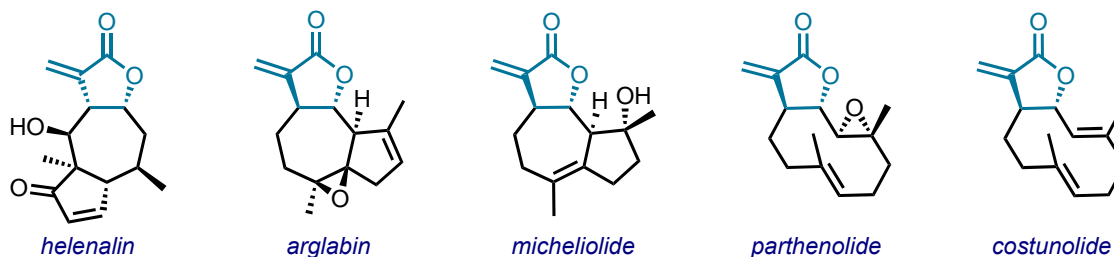
DFT calculations have been used to facilitate the TCI fragment design of various acrylamides, α,β -unsaturated ketones, aldehydes, and esters.¹³⁻¹⁸ DFT calculations provided insights to the structural and electronic factors that influence the reactivity by the assessment of the ground state properties of Michael acceptors.¹⁹ DFT-calculated physical descriptors, such as electrophilicity indices, HOMO–LUMO energies, and atomic charges have been used towards the development of quantitative structure-activity relationship (QSAR) models for the reactivity

prediction of TCI fragments.²⁰⁻²² DFT methods have also been used to calculate thio-Michael addition transition states and to predict the relative reactivity trends via transition state theory (TST).^{13-17, 20, 23}

a) Examples to the covalent modifier drugs with α,β -unsaturated carbonyl group



b) Natural products with α -methylene- γ -lactone moiety



c) α -methylene- γ -lactams

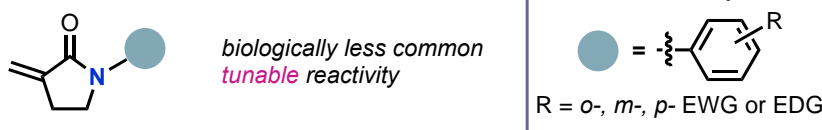


Figure 2.1. Examples of a) drugs and b) natural products equipped with covalent reactive groups, and c) α -methylene- γ -lactams.

The base-catalyzed thio-Michael additions to α,β -unsaturated carbonyl compounds can occur via two different mechanisms: 1,2-olefin addition, and 1,4-conjugate addition (**Figure 2.2**).

In the 1,2-addition, a carbanion is formed upon nucleophilic attack of thiolate to the β -carbon of the Michael acceptor. A direct proton transfer to the α -carbon yields the Michael adduct.²⁴ In the 1,4-conjugate addition, the nucleophilic attack to form the enolate intermediate is followed by the O-protonation to give an enol. Subsequent tautomerization yields the corresponding Michael adduct. Schüürmann et al. investigated the 1,2-addition to the alkenyl group of unsaturated carbonyl as a potential alternative to the 1,4-conjugated mechanism.²⁰ Transition state calculations of methane thiol addition to 35 α,β -unsaturated aldehydes, ketones and esters with and without the initial protonation of the carbonyl group suggested that a 1,2-addition to the olefin pathway is likely for esters. Paasche et al. showed that if a 1,4-conjugate addition mechanism is followed, the final tautomerization step to form the carbonyl compound is kinetically and thermodynamically unfavorable for α,β -unsaturated esters and amides.²⁵

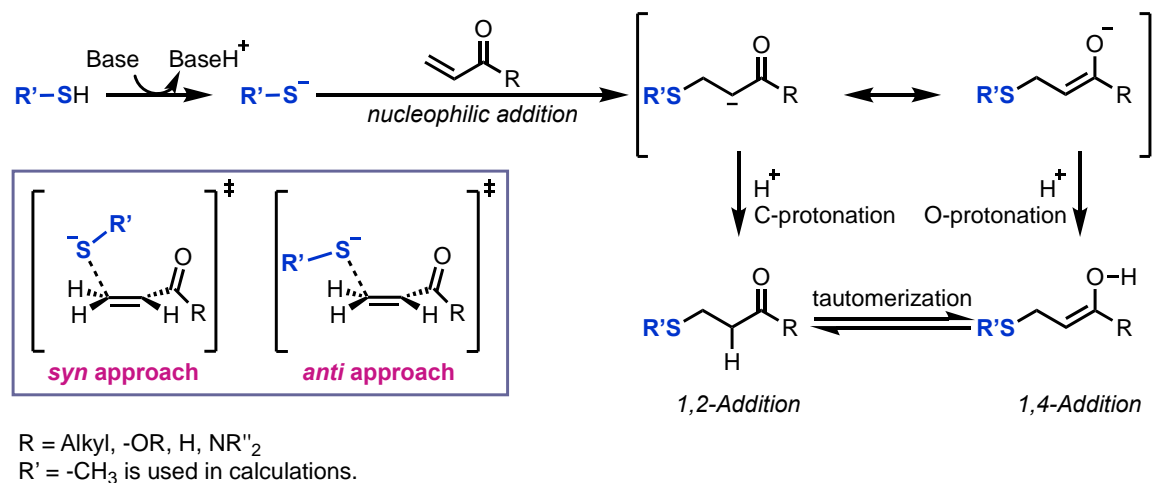


Figure 2.2. Base-catalyzed thio-Michael addition to α,β -unsaturated carbonyl compounds.

In 2011, Houk and Krenske studied the transition state structures of nucleophilic additions to the α,β -unsaturated ketones using methyl thiolate as the model nucleophile.¹⁶ Under the experimental conditions, the thiol deprotonation is expected to be facile and the resulting thiolate

anion is a stronger nucleophile than thiol itself, hence is used as the active nucleophile. Gas phase optimizations of the transition state structures revealed that the methyl thiolate may attack the β -carbon of the α,β -unsaturated ketone via two different orientations of the methyl group, either *syn* or *anti* to the C–C double bond (**Figure 2.2**). The energetics of the computed transition state structures showed that the *syn* approach was more favorable than the *anti* approach by ~2–3 kcal/mol. The *syn* preference results from (i) the minimized repulsion between the sulfur lone pairs and the electron density of the C–C double bond, (ii) an attractive electrostatic interaction between the methyl thiolate hydrogens and the carbonyl oxygen. The latter interaction was shown to be less important when the optimizations were performed in solution. Solution-phase transition state calculations of methyl thiolate addition to *N*-aryl acrylamides performed by Cee and coworkers were consistent with Houk and Krenske’s report on α,β -unsaturated ketones, the *syn* TS is favored in the addition of the nucleophile to the C–C double bond of the *N*-aryl acrylamide.¹³ DFT calculations were also performed to evaluate kinetic barriers and thermodynamic preferences of additions of a model nucleophile (usually methyl thiolate ion) to different Michael acceptors, which is expected to be the rate-determining step of the thio-Michael additions.¹³⁻¹⁸ Good correlations between DFT-calculated activation energies (E_a) and experimentally-determined rate constants (k) were obtained.²⁶ However, the deviations between the absolute values of DFT-calculated free energies of activation ($\Delta G^\ddagger_{\text{DFT}}$) and the experimentally derived $\Delta G^\ddagger_{\text{Experiment}}$ from the Eyring equation (eq 1) were much larger. This has limited the applications of DFT methods to quantitatively predict kinetic profiles of new TCIs. In addition, such DFT models have yet to be applied to the lactam reactivity predictions.

$$k = \frac{\kappa k_B T}{h} e^{\frac{-\Delta G^\ddagger_{\text{Experiment}}}{RT}} \quad (\text{eq 1})$$

In Cee's computational study, the methyl thiolate addition to a series of *N*-aryl acrylamides were calculated at the B3LYP level of theory using IEFPCM solvation model. They demonstrated a linear correlation between the calculated $\Delta G^\ddagger_{\text{DFT}}$ and the experimental reactivity of *N*-aryl acrylamides towards glutathione (GSH) ($\log k_{\text{GSH}}$) with an $R^2 = 0.75$ and a slope of -0.25 .¹³ Similarly, Flanagan et al. calculated the ΔG^\ddagger at the B3LYP level of theory with the SMD solvation model and found a correlation with the reaction half-lives of various acrylamides with GSH with an $R^2 = 0.91$.¹⁴ These studies demonstrated the utility of the application of transition state theory via DFT calculations to predict relative reactivity of TCI fragments. However, accurate calculation of ΔG^\ddagger using DFT methods remains a challenging task. The performance of the DFT calculations is affected by multiple factors, such as the density functional, solvation model, and the choice of the model system (i.e. the active nucleophile).

We hypothesized that the electrophilic reactivity of the α -methylene- γ -lactam can be modulated by extending the conjugation to substitution on the lactam nitrogen. To test our hypothesis, we prepared a series of electronically different *N*-aryl α -methylene- γ -lactams and determined their reactivity towards GSH using mass spectrometry. We performed DFT calculations to establish a computational methodology for robust prediction of the relative reactivity trends of *N*-aryl α -methylene- γ -lactams. We systematically evaluated the predicted reactivity trends from different computational methods, including different functionals (M06-2X, B3LYP), solvation models (SMD, IEFPCM, hereinafter referred to as PCM), and using different nucleophiles (methyl thiolate, cysteamine thiolate, and GSH). Comparison of the computed activation free energies and the experimental rate constants revealed a level of theory that gives reliable predictions of relative reactivities of the *N*-aryl α -methylene- γ -lactams (**Figure 2.3**).

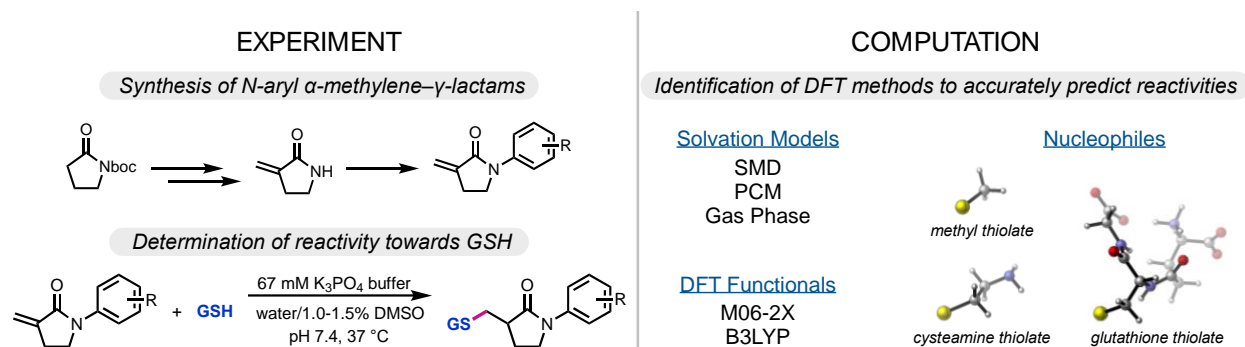
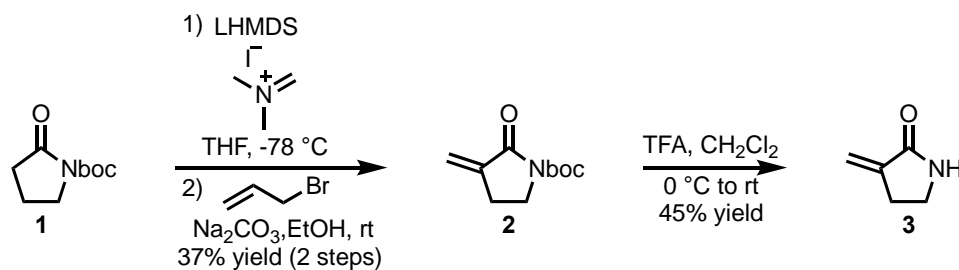


Figure 2.3. Summary of the experimental and computational studies on the GSH reactivity of the *N*-aryl α -methylene- γ -lactams.

2.2 Synthesis of *N*-aryl α -Methylene- γ -lactams

Thirteen electronically different α -methylene- γ -lactams were prepared by a late-stage *N*-arylation of lactam **3**, which is synthesized in four steps from commercially available 2-pyrrolidinone (**Scheme 2.1**).²⁷ Aryl substituents representing a broad range of Hammett values were chosen, along with those groups providing a direct comparison of structural and electronic properties with acyclic *N*-aryl acrylamides.



Scheme 2.1. Synthesis of 3-methylene-2-pyrrolidinone (**3**).

The nitrogen of 2-pyrrolidinone was boc-protected using boc-anhydride and catalytic 4-(*N,N*-dimethylamino)pyridine (DMAP) to form **1** in 83% yield. Installation of the α -methylene

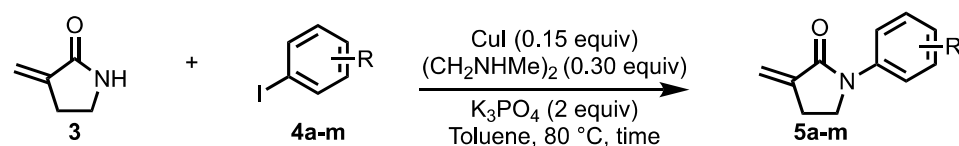
group was accomplished via a two-step process. First, the boc-protected 2-pyrrolidinone **1** was deprotonated with lithium bis(trimethylsilyl)amide (LHMDS) (1.3 equiv) and alkylated with *N,N*-dimethylmethyle iminium iodide, evidenced by crude ¹H NMR. The quaternary ammonium salt was obtained by adding allyl bromide in ethanol, which was subjected to sodium carbonate (Na₂CO₃) to effect an elimination reaction affording the boc-protected α-methylene-γ-lactam **2** (37% yield over two steps). This lactam was reacted with trifluoroacetic acid (TFA) in methylene chloride (CH₂Cl₂) to afford the 3-methylene-2-pyrrolidinone (**3**) in 45% yield (**Scheme 2.1**).

N-arylations of lactam **3** with *para*-, *meta*-, and *ortho*-substituted aryl iodides were achieved using a modified procedure previously reported by Buchwald.²⁸ The aryl iodide equivalents, reaction times, and yields are depicted in Table 2.1. The reaction of lactam **3** with CuI (0.15 equiv), *N,N'*-dimethyl ethylenediamine (0.3 equiv), iodobenzene **4a** (3 equiv) and potassium triphosphate (2 equiv) in toluene at 80 °C afforded the *N*-arylation product **5a** in 81% yield (Table 2.1, entry 1). Subsequent experiments with different aryl iodides revealed that using less aryl iodide (1.5 equiv) resulted in an easier purification of the *N*-arylated product.

Next, the *N*-arylation reaction of lactam **3** with aryl iodides **4b–m** having electron-donating or -withdrawing groups was investigated. Reaction of aryl iodides substituted at the *para*- position with groups that are electron-withdrawing gave *N*-arylation products with yields ranging from 65–79% (Table 2.1, entries 2, 3, 5, and 6). Reaction of lactam **3** with aryl iodides having electron-donating groups, 1-iodo-4-methoxybenzene **4d** and 1-iodo-4-(*N,N*-dimethylamino)benzene **4g**, afforded **5d** and **5g** in 26% and 72% yield, respectively (Table 2.1, entries 4 and 7). The low yield for **5d** was due to purification issues stemming from excess aryl iodide co-eluting with the product. Reaction of lactam **3** with aryl iodides substituted at the *meta*- position afforded products **5h–5j** in 31–60% yield (entries 8–10). Due to the light sensitivity of 1-fluoro-3-iodobenzene **4i**, the reaction

flask was wrapped with aluminum foil affording the *N*-arylation product **5i** in 60% yield after 24 h (Table 2.1, entry 9). Reaction of lactam **3** with aryl iodides substituted at the *ortho*- position afforded products **5k–5m** in 60–81% yield (entries 11–13). The *N*-arylation reaction with 1-fluoro-2-iodobenzene **4l** under the standard conditions gave **5l** in 81% yield (Table 2.1, entry 12). The reaction of 1-iodo-2-nitrobenzene **4m** was slow due to steric effects; however, the *N*-arylation product **5m** was obtained in 80% yield after 72 h (Table 2.1, entry 13).

Table 2.1. Coupling of aryl iodides with 3-methylene-2-pyrrolidinone (**3**) affording *N*-aryl α -methylene- γ -lactams **5a–m**.

				
entry	R	Arl equiv	time	% yield ^a
1	H (5a)	3	24 h	81
2	<i>p</i> -CF ₃ (5b)	3	25 h	79
3	<i>p</i> -CN (5c)	1.6	18 h	69
4	<i>p</i> -OMe (5d)	3	24 h	26
5	<i>p</i> -F (5e)	3	23 h	65
6	<i>p</i> -NO ₂ (5f)	1.5	24 h	68
7	<i>p</i> -NMe ₂ (5g)	1.5	21.5 h	72
8	<i>m</i> -OMe (5h)	1.5	24 h	57
9	<i>m</i> -F (5i)	1.5	24 h	60
10	<i>m</i> -NO ₂ (5j)	1.5	18.5 h	31
11	<i>o</i> -OMe (5k)	1.5	23 h	60
12	<i>o</i> -F (5l)	1.5	25 h	81
13	<i>o</i> -NO ₂ (5m)	1.5	72 h	80

^aIsolated yields.

2.3 Experimental Determination of Reaction Rates for the Conjugate Addition of GSH to α -Methylene- γ -lactams **5a–m**

Reactions were performed with a large excess of GSH to ensure pseudo-first-order kinetics and rate constants, and reaction half-lives were determined in a manner analogous to that reported by Cee et al. with minor modifications,¹³ using liquid chromatography and mass spectrometry (LC-MS) methods. Lactams **5a–m** were reacted in batches over the span of 9.3 h with 10 mM GSH in 67 mM potassium phosphate buffer, pH = 7.4, with 1–1.5% DMSO at 37 °C. These conditions were selected to mimic intracellular GSH concentration and to benchmark reactivities with those previously reported for *N*-aryl acrylamides.^{13-14, 29} Included in each batch were 2–4 *N*-aryl α -methylene- γ -lactams, phenacetin as a stable internal standard, and *N*-phenyl acrylamide (NPA) as a positive control. Lactam stability was monitored with control batches prepared as described above, but excluding GSH.

Peak area ratios were determined by dividing the total ion count (TIC) peak area of the parent compound by that of the internal standard, phenacetin. For each batch, a calibration curve was obtained by measuring the peak area ratio of seven standard solutions of compound **5a** ranging in concentration from 0.2–2.0 μ M. A linear concentration-response relationship was assumed for the internal standard and the lactams. The relative concentrations for each lactam were calculated by fitting the measured peak area ratio to the calibration curve. From these relative concentrations, percent compound remaining was determined relative to time zero and the natural log was plotted against time. The pseudo-first-order rate constant ($k_{pseudo1st}$) was obtained as the slope of the line-of-best-fit following eq 2 and the half-lives were determined with eq 3.

$$\ln([analyte]_t) = -k_{pseudo1st}t + \ln([analyte]_o) \quad (\text{eq 2})$$

$$t_{1/2} = \frac{\ln 2}{k_{pseudo1st}} \quad (\text{eq 3})$$

The measured pseudo-first order rate constants for the reactions of NPA and lactams **5a–f** and **5h–m** with GSH are presented in Table 2.2. The mean half-life of NPA (119 min, entry 1) was within the range of half-lives for the same compound reported previously.^{13-14, 29}

Table 2.2. Measured rates of GSH addition, derived half-lives, and spectroscopic data.

up to four lactam reactivities measured at once

entry	compound	Hammett Parameter ^b σ _p ⁻ or σ _m	t _{1/2} (min)	k _{pseudo1st} (min ⁻¹ × 10 ⁻³)	log k _{GSH} (M ⁻¹ s ⁻¹)	H ^{β1} δ (ppm)	H ^{β2} δ (ppm)	C ^β δ (ppm)	C=O λ ⁻¹ (cm ⁻¹)
1	NPA	-	119	5.83	-2.01	-	-	-	-
2	H (5a)	0.00	1386	0.50	-3.08	5.46	5.90	115.8	1673
3	<i>p</i> -CF ₃ (5b)	0.65	525	1.32	-2.66	5.53	5.96	117.0	1685
4	<i>p</i> -CN (5c)	1.00	207	3.35	-2.25	5.54	5.97	117.4	1691
5	<i>p</i> -OMe (5d)	-0.26	2888	0.24	-3.40	5.42	5.86	115.3	1681
6	<i>p</i> -F (5e)	-0.03	1873	0.37	-3.21	5.47	5.90	116.0	1681
7	<i>p</i> -NO ₂ (5f)	1.27	73	9.52	-1.80	5.57	6.00	117.7	1692
8	<i>p</i> -NMe ₂ (5g)	-0.12	-	-	-	5.39	5.83	114.7	1668
9	<i>m</i> -OMe (5h)	0.12	2166	0.32	-3.28	5.46	5.89	116.0	1676
10	<i>m</i> -F (5i)	0.34	835	0.83	-2.86	5.50	5.93	116.6	1679
11	<i>m</i> -NO ₂ (5j)	0.71	450	1.54	-2.59	5.55	5.98	117.1	1682
12	<i>o</i> -OMe (5k)	-0.26	4077	0.17	-3.55	5.41	5.80	115.2	1685
13	<i>o</i> -F (5l)	-0.03	1777	0.39	-3.19	5.49	5.88	116.1	1685
14	<i>o</i> -NO ₂ (5m)	1.27	333	2.08	-2.46	5.51	5.86	117.1	1693

Relative to the electronically neutral **5a** (t_{1/2} = 1386 min), the electron-donating methoxy group on the *para*-, *meta*-, and *ortho*-positions of the aryl slowed the rate of reaction as evidenced by the half-lives (t_{1/2} = 2888 min, 2166 min, and 4077 min, respectively). The fluoro group slowed the reaction when positioned *para*- or *ortho*- (t_{1/2} = 1873 min and 1777 min, respectively). With its π-donating ability diminished in the *meta*- position, the inductive nature of the fluoro group resulted in a shorter half-life (t_{1/2} = 835 min). Electron-withdrawing groups, such as *para*-, *meta*-,

and *ortho*-NO₂ and *para*-CF₃ and *para*-CN groups accelerated the reaction. Measurement of the half-life for the reaction of the *para*-dimethylamino-substituted lactam **5g** was unsuccessful due to the insolubility of a dimethylammonium salt of the lactam formed under the acidic chromatography conditions, evidenced by a substantial increase in the column pressure.

2.4 Correlation of the GSH Reactivity of the *N*-Aryl α -Methylene- γ -lactams with the Hammett Parameters, ¹H NMR, ¹³C NMR Shifts and IR Frequencies

To evaluate factors affecting the reactivities of the *N*-aryl α -methylene- γ -lactams, the observed initial reaction rate (*k*) values were compared with the Hammett parameters and spectroscopic data of the compounds. As illustrated in **Figure 2.4**, for each compound, the rate of Michael addition reaction with GSH is closely associated with its Hammett parameter. The influence of resonance on reactivity is demonstrated by the better correlation with σ_p^- than σ_p for *para*- and *ortho*-substituted *N*-aryl α -methylene- γ -lactams ($R^2 = 0.98$ and 0.93 , respectively) and with σ_m for *meta*-substituted *N*-aryl α -methylene- γ -lactams ($R^2 = 0.81$). The reactivities of the *ortho*-substituted compounds can be correlated to the σ_p^- , except *ortho*-NO₂. We attribute this to the strong influence of the steric effects on the conformation of the lactam, which is also evidenced by peak broadening in the ¹H NMR spectrum, indicating the hindered rotation about the N–C(sp²) bond.

The positive ρ values for σ_p^- and σ_m (1.01 and 0.86, respectively) agree with the computed mechanistic pathway of thiolate addition to the *N*-aryl α -methylene- γ -lactams, showing electron withdrawing groups stabilizing the developing negative charge in the transition state (*vide infra*). The ρ value of 1.01 for *para*- and *ortho*-substituted lactams demonstrates that they are sensitive to

the substituent effects, whereas the smaller ρ value for *meta*-substituted lactams (0.86) suggests that these compounds are slightly less sensitive to the substituent effects. The greater ρ value for *para*- and *ortho*-substituted lactams is consistent with the sensitivity of the Michael addition to the resonance effects.

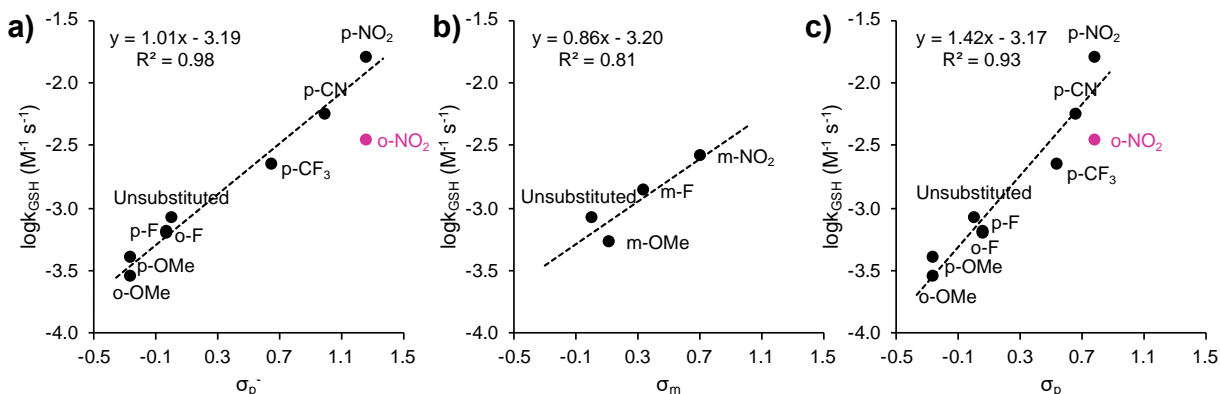


Figure 2.4. The relationship of Hammett parameters σ_p^- , σ_m or σ_p with the rate of GSH addition to *N*-aryl α -methylene- γ -lactams with a) *para*- and *ortho*-, b) *meta*-, and c) *para*- and *ortho*-substitutions on the aryl ring. The reactivities of lactams with *para*- and *ortho*-substitution on the aryl ring correlate well to the σ_p^- , and lactams with *meta*-substitution on the aryl ring correlate well to the σ_m . *ortho*-NO₂ is excluded from the linear fitting line.

Because reaction rate is controlled by the substituent's effect on the electronic nature of the molecule, it was predicted that simple spectroscopic characterization methods that probe the effective electronic environment around key atoms or bonds could be utilized to establish trends with the rate of reaction. Indeed ¹H NMR, ¹³C NMR, and infrared spectroscopy (IR) showed varying degrees of parity with the measured rate constants.

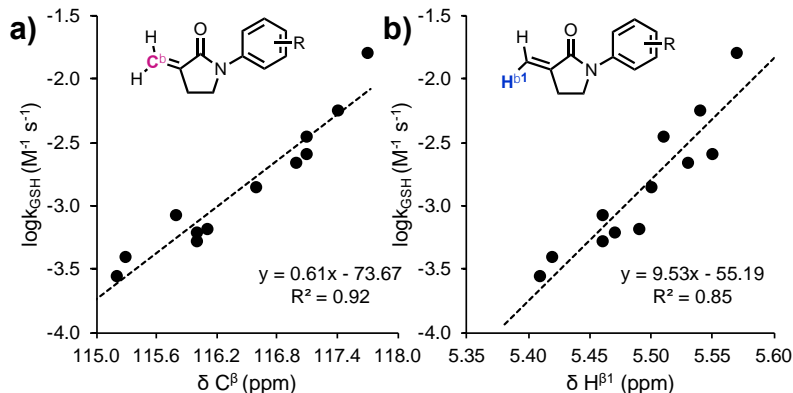


Figure 2.5. Correlation of $\log k_{\text{GSH}}$ with a) ^{13}C NMR and b) ^1H NMR shifts.

The highest degrees of correlation were observed for the ^{13}C NMR shifts of the C^β ($R^2 = 0.92$, **Figure 2.5a**) and the ^1H NMR shifts of the methylenyl proton $H^{\beta 1}$ ($R^2 = 0.85$, **Figure 2.5b**). For the *N*-aryl acrylamides with the same substitution patterns, the correlation of the GSH reactivity and the ^{13}C NMR of the C^β and ^1H NMR shifts of the methylenyl proton have similar fitting of data, $R^2 = 0.90$ and 0.84 , respectively (see Appendix A).¹³ A weaker correlation was observed for the ^1H NMR shift of $H^{\beta 2}$ and the ^{13}C NMR of the carbonyl carbon ($R^2 = 0.63$ and 0.62 respectively, **Figures 2.6a** and **2.6b**). As predicted, electron-donating groups increased the sp^3 -character of the $\text{C}=\text{O}$ bond, as shown by lower IR frequencies. However, these data displayed the weakest correlation with reaction rate ($R^2 = 0.43$, **Figure 2.6c**). Experimental studies of our *N*-aryl α -methylene- γ -lactams showed a ten-fold reactivity attenuation with GSH compared to the *N*-aryl acrylamides.¹³

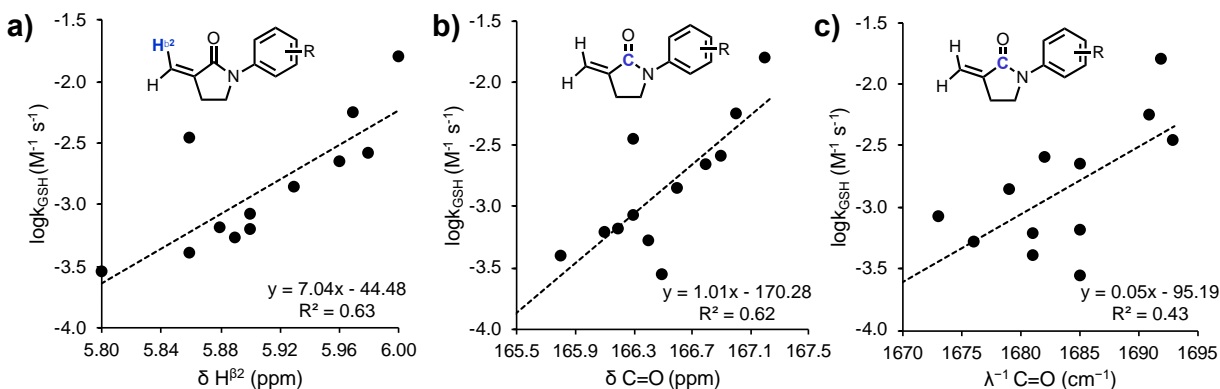


Figure 2.6. Correlations of the a) ^1H NMR shift (ppm) of $\text{H}^{1\beta}$, b) ^{13}C NMR shift (ppm) of the carbonyl carbon, and c) IR resonances (cm^{-1}) of the carbonyl group of the *N*-aryl lactams to experimentally-determined values of $\log k_{\text{GSH}}$. Compound **5g** (*p*- NMe_2) is excluded due to lack of rate data.

2.4.1 Computational Methods

Geometry optimizations and single point energy calculations were carried out using Gaussian 16.³⁰ Geometries of intermediates and transition states were optimized using the M06-2X³¹ and B3LYP³²⁻³³ functionals with the 6-31+G(d) basis set. Vibrational frequency calculations were performed for all the stationary points to confirm if each optimized structure is a local minimum or a transition state structure. Truhlar's quasiharmonic approximations³⁴ were applied for entropy calculations using 100 cm^{-1} as the frequency cutoff using Goodvibes v2.0.1.³⁵ Solvation energy corrections were calculated in water with the SMD³⁶ and PCM³⁷⁻³⁸ solvation models based on the geometries optimized in solution. The M06-2X and B3LYP functionals with the 6-311+G(d,p) basis set were used for single point energy calculations in water, with SMD and IEFPCM solvation models.

Optimization of **TS1s_gas** was performed in the gas phase using the M06-2X functional with the 6-31+G(d) basis set, and the single point energy calculations were performed using the

M06-2X functional with the 6-311+G(d,p) basis set. Images of transition state structures were generated using CYLview.³⁹

Coupled cluster (CC) calculations were performed using MOLPRO⁴⁰⁻⁴¹ software to assess the performance of the DFT-calculated energies. These energy calculations were performed with structures optimized using DFT at the M06-2X/6-31+G(d)(SMD) level of theory. The electronic energies of activation of methyl thiolate addition to *N*-aryl α -methylene- γ -lactams were calculated in the gas phase, using local density-fitted CCSD(T) methods (DF-LCCSD(T)-F12)⁴²⁻⁴⁵ with the cc-pVDZ-F12 basis set. These results were used to compare with the electronic energies of activation calculated in the gas phase at the M06-2X/6-311+G(d,p) level of theory.

2.4.2 Results and Discussion

2.4.2.1 *Syn* vs *Anti* Addition of the Thiolate and the Impact of Solvation Models on the Geometry

We first compared the optimized transition state geometries and activation energies of the reaction of *N*-phenyl α -methylene- γ -lactam **5a** with methyl thiolate (**Figure 2.7**). Regardless of the computational method used, the thio-Michael addition transition state always favors thiolate approach with a *syn* orientation placing the methyl group on the thiolate *syn*-periplanar with the C–C double bond of the Michael acceptor. For example, the *syn* TS (**TS1s**, **Figure 2.7**) is preferred over the *anti* TS (**TS1a**) by 2.5 kcal/mol at the M06-2X/6-311+G(d,p)(SMD)//M06-2X/6-31+G(d)(SMD) level of theory when methyl thiolate was used as the nucleophile. This preference is consistent with the previous computational study by Houk and Krenske on methyl thiolate addition to α,β -unsaturated ketones.¹⁶

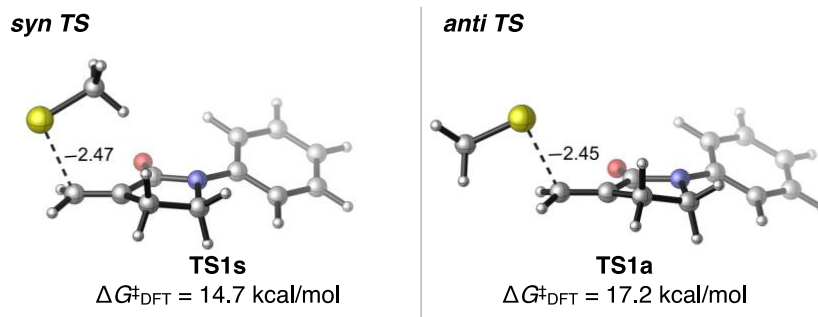


Figure 2.7. *syn* and *anti* transition states of the thio-Michael addition of the methyl thiolate to the *N*-phenyl α -methylene- γ -lactam **5a**.

Transition states and activation free energies (ΔG^\ddagger) were calculated at the M06-2X/6-311+G(d,p)(SMD)//M06-2X/6-31+G(d)(SMD) level of theory. All geometry optimizations and single point energy calculations were performed in water. All energies are with respect to the corresponding thiolate and **5a**.

Solvation model greatly impacts the transition state geometries and the activation energy barriers. The $C^\beta \cdots S$ distance in the methyl thiolate addition to **5a** is 0.14 Å shorter in the PCM-optimized transition state (**TS1s_PCM**, **Figure 2.8a**) than the SMD-optimized transition state (**TS1s**, **Figure 2.7**), and the barriers of the thiolate additions are 18.6 and 14.7 kcal/mol, respectively.

Calculations in the gas phase not only significantly underestimate the activation free energy (compare $\Delta G^\ddagger_{\text{DFT}} = -1.7$ kcal/mol and $\Delta G^\ddagger_{\text{Experiment}} = 22.9$ kcal/mol for **5a**) but also predict much earlier transition state as evidenced by the significantly longer $C^\beta \cdots S$ distance than those optimized in solvent (**TS1s_gas**, **Figure 2.8b**). The earlier transition state predicted by the gas phase calculations is consistent with the greater nucleophilicity of the negatively charged thiolate ion in the gas phase, where a more exothermic reaction leads to an earlier transition state, based on the Hammond's postulate. These results indicate that a suitable solvation model should be used in both geometry optimizations and single point energy calculations.

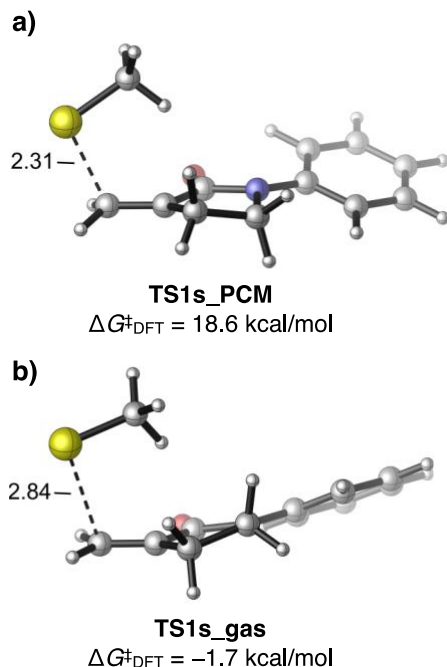


Figure 2.8. Transition states of the thio-Michael additions to the *N*-phenyl lactam **5a** with methyl thiolate a) calculated using PCM solvation model in water, and b) in the gas phase.

Transition states and activation free energies (ΔG^\ddagger) were calculated at the a) M06-2X/6-311+G(d,p)(PCM)//M06-2X/6-31+G(d)(PCM) level of theory and b) M06-2X/6-311+G(d,p)//M06-2X/6-31+G(d) level of theory in the gas phase (right). All geometry optimizations and single point energy calculations were performed in water, except for **TS1s_gas**. All energies are with respect to the corresponding thiolate and **5a**.

2.4.2.2 Impact of the Nucleophile on the Computed Activation Barriers of GSH Addition and Calculation Accuracy Determination

Next, we investigated whether using a more realistic model nucleophile, such as the cysteamine thiolate or the deprotonated glutathione (hereon referred to as glutathione), would affect the predicted transition state geometries and the agreement between computed and experimental ΔG^\ddagger values. We surmised that these more realistic models would be able to identify and describe the potential H-bonding interactions between groups on the nucleophile (the primary amine (NH₂) of cysteamine or a secondary amide of GSH) and the *N*-aryl α -methylene- γ -lactam,

and the steric effects of the glutathione. If these factors are prominent in determining the transition state energies, the use of these thiolates should afford better agreement with experiment than the use of methyl thiolate.

Similar to the methyl thiolate addition, the *syn* additions of the cysteamine thiolate and the glutathione are favored (TS2s and TS3s, Figure 2.9).

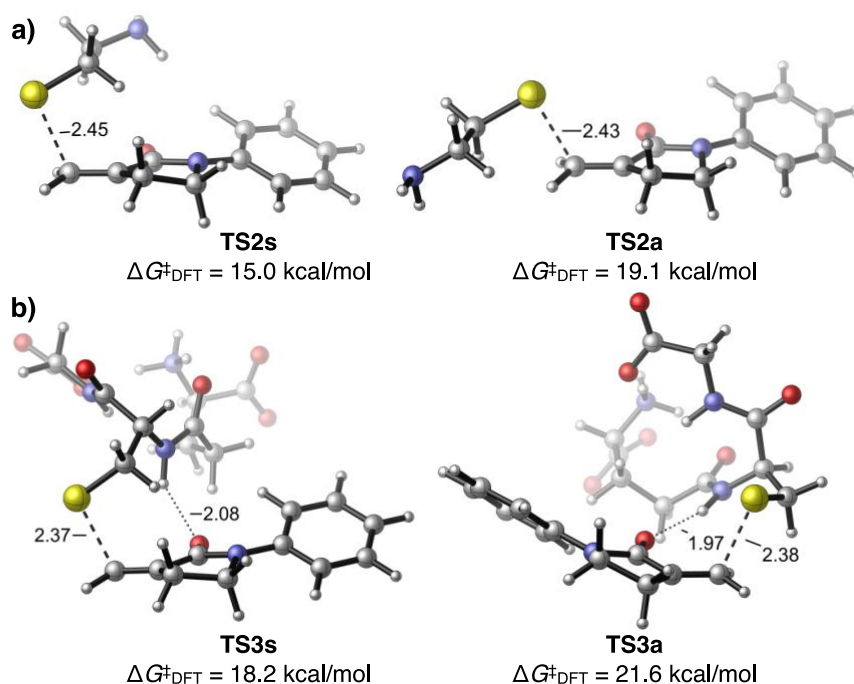


Figure 2.9. Transition state structures of the thio-Michael additions to the *N*-phenyl α -methylene- γ -lactam **5a** with a) cysteamine thiolate, b) with glutathione (–2 charged with both a thiolate and carboxylate) as the nucleophile.

Transition states and activation free energies (ΔG^\ddagger) were calculated at the M06-2X/6-311+G(d,p)(SMD)//M06-2X/6-31+G(d)(SMD) level of theory. All geometry optimizations and single point energy calculations were performed in water. All energies are with respect to the corresponding thiolate and **5a**.

We did not observe strong H-bonding interactions between the NH₂ on the cysteamine thiolate and **5a** in TS2s, demonstrated by the distance between closest proton on the primary amine

(NH₂) of the nucleophile and the carbonyl oxygen (2.84 Å). On the other hand, H-bonding interactions with one of the amide groups on glutathione are present in both *syn* and *anti* transition states (2.08 and 2.38 Å for **TS3s** and **TS3a** respectively, **Figure 2.9b**). Therefore, the potential H-bonding interactions with these more realistic nucleophiles do not alter the preference for *syn* transition states.

Distortion-interaction analysis of the *syn* and *anti* transition states with glutathione demonstrated that the *syn* TS (**TS3s**) has stronger ΔE_{int} than the *anti* TS (**TS3a**) (−9.3 and −6.1 kcal/mol for **TS3s** and **TS3a**, respectively, see Table 2.3). These results suggest the dominant factor favoring the *syn* TS is the diminished closed-shell repulsions between a S lone pair on the nucleophile and the π electrons on C–C double bond of the Michael acceptor.

Table 2.3. Summary of the results of the distortion-interaction analysis.

Calculations were performed at the M06-2X/6-311+G(d,p)(SMD)//M06-2X/6-31+G(d)(SMD) level of theory in water.

TS	$\Delta G_{\text{DFT}}^\ddagger$ (kcal/mol)	$\Delta E_{\text{Dist}}^{\text{Lactam}}$ (kcal/mol)	$\Delta E_{\text{Dist}}^{\text{Nucleophile}}$ (kcal/mol)	ΔE_{int} (kcal/mol)
TS1s	14.7	6.7	0.2	-5.1
TS1a	17.2	7.4	-0.1	-2.1
TS2s	15.0	7.5	-0.4	-6.7
TS2a	19.1	8.0	-0.1	-2.5
TS3s	18.2	9.2	2.1	-9.3
TS3a	21.6	9.6	1.8	-6.1

Comparing to the reaction with methyl thiolate, using cysteamine thiolate as the model nucleophile afforded only a slight increase in the predicted ΔG^\ddagger values. On the other hand, the computed activation free energy with glutathione ($\Delta G^\ddagger = 18.2$ kcal/mol) is 3.5 kcal/mol higher than that with methyl thiolate. The $\Delta G_{\text{DFT}}^\ddagger$ of **TS3s** (18.2 kcal/mol) is closer to the $\Delta G_{\text{Experiment}}^\ddagger$ for this substrate (22.9 kcal/mol). We attribute this to the greater distortion of both the lactam and the nucleophile

in **TS3s** than in **TS1s** (Table 2.3), and the increase in steric repulsions about the forming C^β...S bond due to a later transition state with GSH (the C^β...S distances in **TS3s** and **TS1s** are 2.37 and 2.47 Å, respectively, **Figure 2.9** and **Figure 2.7**).

2.4.2.3 Impact of the DFT Functional and Solvation Models on Computed Activation

Barriers and the Calculation Accuracy

Next, we calculated the barriers to the Michael addition of methyl thiolate to 12 different *N*-aryl α-methylene-γ-lactams using different computational methods, including different density functionals (M06-2X, B3LYP) and solvation models (SMD, PCM). These functionals were selected because of the use of B3LYP in previous studies and the broad applications of the hybrid-meta-GGA functional M06-2X in recent computational organic chemistry literature.^{13, 16-17} Furthermore, we calculated thermal corrections to Gibbs free energies using both the harmonic oscillator model and Truhlar's quasiharmonic approximation to account for the challenges in computing contributions to entropies from low vibrational frequencies. Because the thiolate identity did not affect the preferred Michael addition mechanism (*vide supra*), the methyl thiolate was used in these calculations to reduce computational cost.

The use of M06-2X with the SMD solvation model and quasiharmonic approximation provided the best correlation with the experimental reactivities of *N*-aryl α-methylene-γ-lactams (**Figure 2.10a**). At this level of theory, not only does the correlation of the calculated and experimental reactivities provides one of the highest fitting-of-data ($R^2 = 0.95$), but also the slope of the linear fitting is closest to unity (0.83). A similar correlation between $\Delta H^\ddagger_{\text{DFT}}$ and $\Delta G^\ddagger_{\text{Experiment}}$ was observed ($R^2 = 0.96$, **Figure 2.10a**), which indicates entropic effects do not affect the relative reactivity trends and thus the computed activation free energies from quasiharmonic approximation and activation enthalpies may both be used to predict the relative reactivity trend

of different α -methylene- γ -lactam TCIs. On the other hand, the use of the PCM solvation model instead of SMD gave a linear fitting line with a much smaller slope (0.43) and a moderate correlation of data ($R^2 = 0.84$, **Figure 2.10b**). We believe this is due to the differences in the TS geometries optimized with PCM. The PCM-optimized transition states have 0.16 Å shorter $C^\beta \cdots S$ distances on average than those optimized with the SMD solvation model (**Figure 2.8a**).

Interestingly, when the PCM solvation model was employed, the use of quasiharmonic approximation did not improve the correlation between the $\Delta G^\ddagger_{\text{DFT}}$ and $\Delta G^\ddagger_{\text{Experiment}}$, regardless of the choice of functional (**Figures 2.10b** and **2.12b**). The improvement to the $\Delta G^\ddagger_{\text{DFT}}$ with quasiharmonic approximation in SMD-optimized transition states is due to the longer distance between the sulfur and the lactam carbon in the transition states, as the greater distance in the transition state leads to a greater number of small vibrational frequencies, which, in turn, give larger errors to the calculated entropies using the harmonic oscillator model. This is also supported by the high fitting-of-data ($R^2 = 0.96$) and the slope close to unity (0.87) of the correlation of the calculated enthalpies and experimental activation free energies (**Figure 2.10a**, right panel).

We tested whether this computational approach could be applied to other types of Michael acceptors, such as *N*-aryl acrylamides. We computed the Gibbs free energies of activation of the methyl thiolate addition to various *N*-aryl acrylamides and compared these predicted values with the activation free energies reported in a previous experimental study from Cee et al. (**Figure 2.11**).¹³

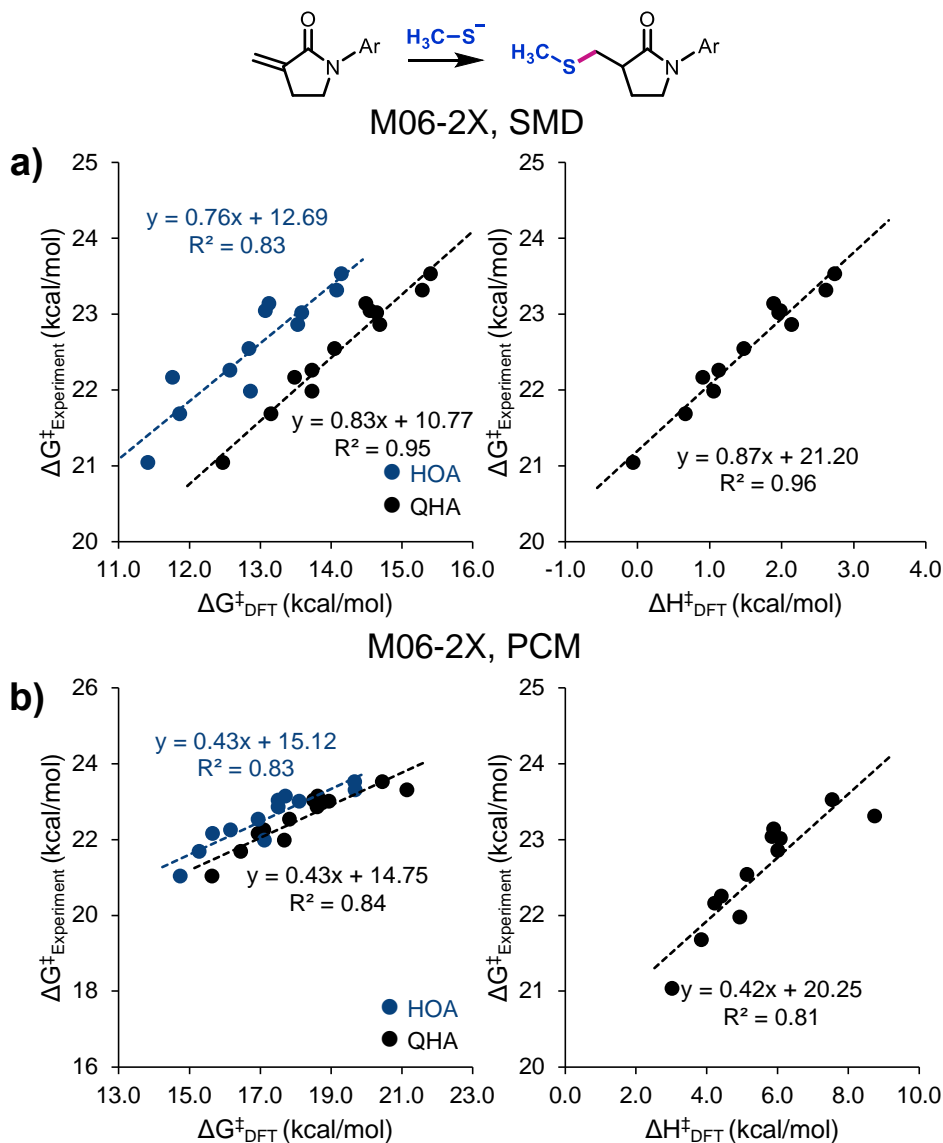


Figure 2.10. Correlation of the a) DFT-M06-2X-SMD calculated reactivity and b) DFT-M06-2X-PCM calculated reactivity to the experimentally-determined reactivity (left), and the correlation of the DFT-calculated enthalpies to the experimentally-determined reactivity (right).

Experimental ΔG^\ddagger values were derived from the Eyring equation. The free energy of activation of the Michael additions of methyl thiolate to the *N*-aryl α -methylene- γ -lactams were calculated at the a) M06-2X/6-311+G(d,p)(SMD)//M06-2X/6-311+G(d)(SMD) b) M06-2X/6-311+G(d,p)(PCM)//M06-2X/6-311+G(d)(PCM) levels of theory. All optimizations and single point calculations were performed in water. (HOA: harmonic oscillator approximation, QHA: quasiharmonic approximation).

The calculations gave a high fitting of data ($R^2 = 0.87$) and a slope of the linear fitting close to unity (0.89). These results suggest that this level of theory may be applied to reactivity prediction for other substrates.

The previously used hybrid-GGA functional B3LYP with the SMD solvation model provided a high R^2 value of 0.96, but the slope was significantly lower than unity (0.45, **Figure 2.12a**). These results indicate that B3LYP is capable of qualitatively predicting the reactivity trend, but would underestimate the reactivity difference between two TCIs.

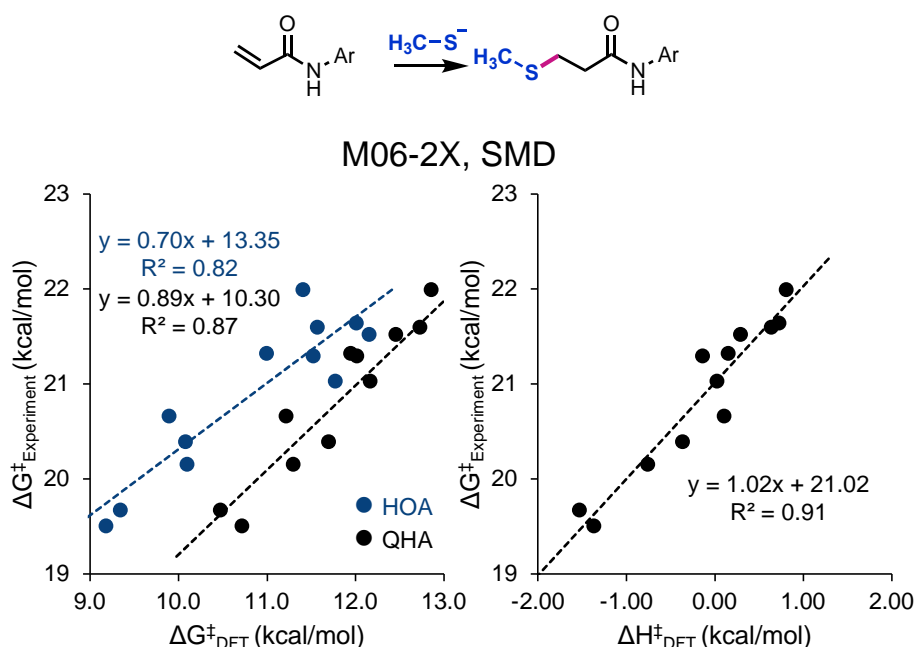


Figure 2.11. Correlation of the DFT-M06-2X-SMD-calculated reactivity to the experimentally-determined reactivity (left) and the correlation of the DFT-calculated enthalpies to the experimentally-determined reactivity (right).

Experimental ΔG^\ddagger values were derived from the Eyring equation using the data from reference 13. The free energy of activation of the Michael additions of methyl thiolate to the *N*-aryl acrylamides were calculated at the M06-2X/6-311+G(d,p)(SMD)//M06-2X/6-31+G(d)(SMD) level of theory. All optimizations and single point calculations were performed in water. (HOA: harmonic oscillator approximation, QHA: quasiharmonic approximation).

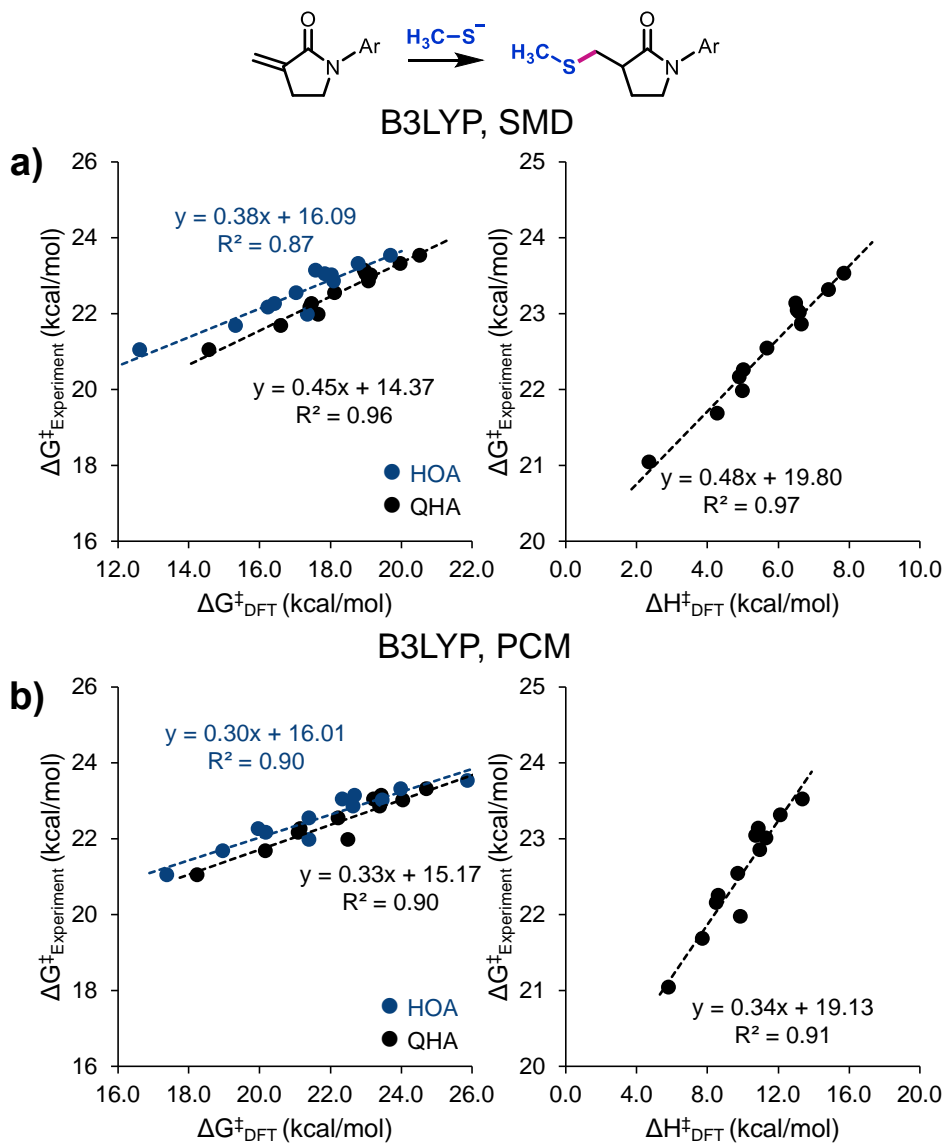


Figure 2.12. Correlation of the a) DFT-B3LYP-SMD-calculated reactivity and b) DFT-B3LYP-PCM-calculated reactivity to the experimentally-determined reactivity (left), and the correlation of the DFT-calculated enthalpies to the experimentally-determined reactivity (right).

Experimental ΔG^\ddagger values were derived from the Eyring equation. The free energy of activation of the Michael additions of methyl thiolate to the *N*-aryl α -methylene- γ -lactams were calculated at the a) B3LYP/6-311+G(d,p)(SMD)//B3LYP/6-311+G(d)(SMD) b) B3LYP/6-311+G(d,p)(PCM)//B3LYP/6-311+G(d)(PCM) levels of theory. All optimizations and single point calculations were performed in water. (HOA: harmonic oscillator approximation, QHA: quasiharmonic approximation).

Next, we explored whether the use of deprotonated cysteamine instead of methyl thiolate as the nucleophile in the transition state calculations would affect the predicted reactivity trend of different Michael acceptors (**Figure 2.13**). We calculated the activation free energies of Michael addition of the cysteamine thiolate to the twelve different *N*-aryl α -methylene- γ -lactams at the M06-2X/6-311+G(d,p)(SMD)//M06-2X/6-31+G(d)(SMD) level of theory.

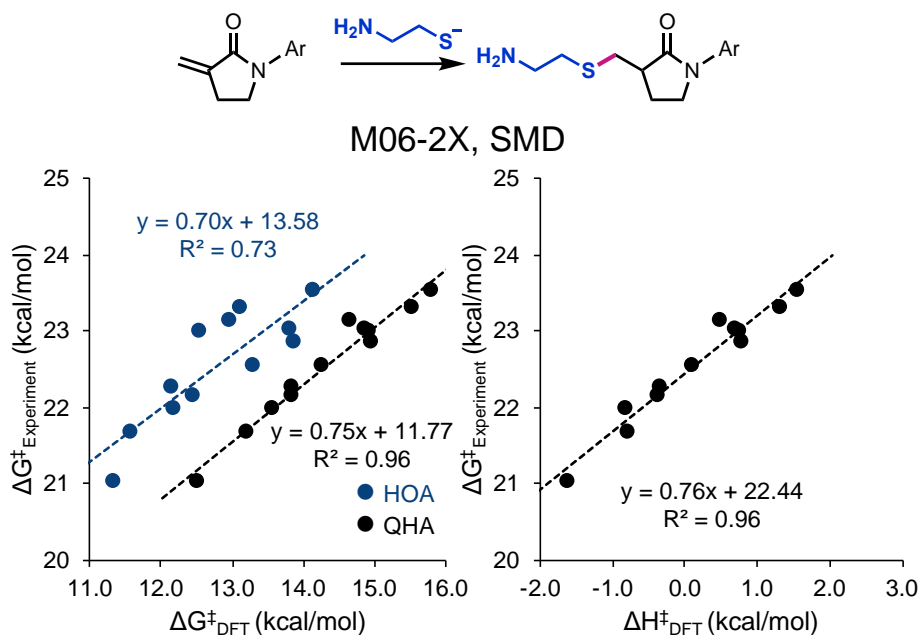


Figure 2.13. Correlation of the DFT-M062X-SMD-calculated reactivity to the experimentally-determined reactivity (left) and the correlation of the DFT-calculated enthalpies to the experimentally-determined reactivity (right).

The free energy of activation of the Michael additions of cysteamine thiolate to the *N*-aryl α -methylene- γ -lactams were calculated at the M06-2X/6-311+G(d,p)(SMD)//M06-2X/6-31+G(d)(SMD) level of theory. All optimizations and single point calculations were performed in water. (HOA: harmonic oscillator approximation, QHA: quasiharmonic approximation)

Experimentally-determined reactivities and DFT-calculated activation barriers showed good correlations for predicted reactivity both the cysteamine thiolate and methyl thiolate when using the quasiharmonic approximation ($R^2 = 0.96$ and 0.95 , respectively). A good correlation between the Gibbs free energies of activation derived from experimental rate constants ($\Delta G^\ddagger_{\text{Experiment}}$) and the computed enthalpies of activation ($\Delta H^\ddagger_{\text{DFT}}$) was observed, indicating the experimental reactivity trend is not due to entropic effects.

The slope of the fitted line was slightly smaller with cysteamine thiolate than that with methyl thiolate (0.75 and 0.83 , respectively). The correlation of $\Delta H^\ddagger_{\text{DFT}}$ and $\Delta G^\ddagger_{\text{Experiment}}$ with cysteamine thiolate has high fitting-of-data ($R^2 = 0.96$), but a smaller slope than that with methyl thiolate (0.76 and 0.87 , respectively). Overall, a larger model thiolate having an NH_2 group afforded activation barriers in closer alignment with experiment (~ 1 kcal/mol higher in energy than methyl thiolate) but did not improve the accuracy of the predicted relative reactivities of *N*-aryl α -methylene- γ -lactams.

2.4.2.4 Coupled Cluster Calculations

The electronic energies of activation computed using local (L) density-fitted (DF) coupled-cluster (CC) singles (S) and doubles (D) augmented by perturbative treatment of triples method with F12 approximations⁴⁶ (DF-LCCSD(T)-F12) and M06-2X were summarized in the correlation plots in **Figure 2.14**. Excellent correlation between the energies from the two different levels of theories was obtained ($R^2 = 1.00$), albeit with a systematic underestimation of the barriers of the methyl thiolate addition (**Figure 2.14**). These results suggest that M06-2X-computed energies can reliably predict the relative reactivities of different *N*-aryl α -methylene- γ -lactams. The major source of error of the DFT-computed activation Gibbs free energies in solution likely originates

from solvation energy corrections and thermal corrections, such as entropies calculated using the harmonic oscillator approximations.

We also compared the effects of basis sets on the energies of the DF-LCCSD(T)-F12 calculations. Although a relatively small basis set (cc-pVDZ-F12) was used in the benchmark calculations shown in Table 2.4, the use of a larger triple-zeta basis set did not significantly affect the computed activation electronic energies. Due to computational cost, the triple-zeta basis set calculations were only performed for **5a**, **5i**, and **5l**, three substrates with the smallest number of atoms used in this study. These results are consistent with previous reports that indicate the explicitly correlated F12 coupled cluster theory is less sensitive to the size of the basis set.⁴⁵

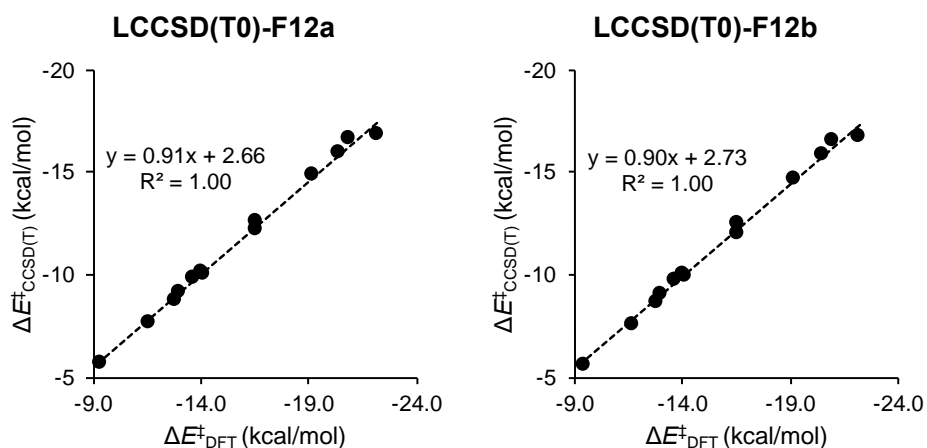


Figure 2.14. Correlation of the CC and DFT-calculated electronic energies of activation for the methyl thiolate addition to *N*-aryl lactams.

The energy of activation of the Michael additions of methyl thiolate to the *N*-aryl α -methylene- γ -lactams were calculated using the coupled cluster methods LCCSD(T0)-F12a LCCSD(T0)-F12b, and DFT method M06-2X/6-311+G(d,p) in the gas phase, on the structures optimized at the M06-2X/6-31+G(d)(SMD) level of theory in water.

Table 2.4. Comparison of the activation electronic energies calculated with cc-pVDZ-F12 and cc-pVTZ-F12 basis sets.

All energies are in kcal/mol and with respect to the methyl thiolate anion and *N*-aryl α -methylene- γ -lactam reactants.

		LCCSD(T0)-F12a	LCCSD(T0)-F12b
m-F	VTZ	-13.0	-13.0
	VDZ	-12.6	-12.5
	$\Delta\Delta E^\ddagger$	-0.4	-0.5
o-F	VTZ	-9.3	-9.3
	VDZ	-8.8	-8.7
	$\Delta\Delta E^\ddagger$	-0.5	-0.6
H	VTZ	-10.7	-10.7
	VDZ	-10.2	-10.1
	$\Delta\Delta E^\ddagger$	-0.5	-0.6

2.5 Conclusions

In this work we present the α -methylene- γ -lactam as a novel covalent reactive group that can be incorporated as a TCI fragment to react with cysteine residues. Thirteen electronically different α -methylene- γ -lactams were prepared by a late-stage *N*-arylation, synthesized in four steps from commercially available 2-pyrrolidinone. The electrophilicity of the α -methylene group can be tuned by modifying the nitrogen substituent as demonstrated by GSH reactivity studies. Experimental studies of our *N*-aryl α -methylene- γ -lactams showed a ten-fold reactivity attenuation with GSH compared to the *N*-aryl acrylamides. Characterization of the thiol reactivity of this lactam warhead will be valuable in the rational design of covalent inhibitors for several enzyme classes. The reactivity of the *N*-aryl α -methylene- γ -lactams towards GSH shows good correlation with the ^{13}C NMR shifts of the C^β resonance of the methylene ($R^2 = 0.92$) and with the Hammett parameters σ_p^- for the *para*- and *ortho*- ($R^2 = 0.98$), and σ_m for the *meta*- aryl substitution ($R^2 =$

0.81). The positive ρ values for σ_p^- and σ_m support the anionic mechanism of thiolate addition to the *N*-aryl α -methylene- γ -lactams.

A computational protocol was established for predicting relative reactivities of the *N*-aryl α -methylene- γ -lactams. Systematic studies with different density functionals (B3LYP, M06-2X), different solvation models (PCM, SMD), and model nucleophiles (methyl thiolate, cysteamine thiolate, and glutathione) demonstrated that the use of the M06-2X functional with the SMD solvation model, and the methyl thiolate nucleophile serves this purpose efficiently. The application of quasiharmonic approximations improve the linear correlation between the experiment and computation. Consistent with the benchmark studies on the *N*-aryl α -methylene- γ -lactams, calculations with the *N*-aryl acrylamides that have the same substitution patterns as our *N*-aryl α -methylene- γ -lactams resulted in the best performance with the same level of theory with quasiharmonic approximations.

2.6 Synthesis and Characterization of Compounds

2.6.1 General Information

Unless otherwise stated, all reactions were performed in flame-dried glassware under an atmosphere of dry nitrogen. All commercially available starting materials were used as received, without further purification. Reaction solvents tetrahydrofuran (THF) and dichloromethane (DCM) were purified via pressure filtration through an alumina column. Toluene was distilled from CaH₂ before use. Column chromatography was performed using 40-63 μ m, 60 Å pore size silica gel. TLC was performed on Silicycle glass backed 60 Å plates containing F₂₅₄ indicator. ¹H

NMR and ^{13}C NMR spectra were obtained using a Bruker Avance 500 MHz spectrometer. Spectra were referenced to chloroform (^1H : 7.26 ppm and ^{13}C : 77.16 ppm) and DMSO (^1H : 2.50 ppm and ^{13}C : 39.51 ppm). Chemical shifts are reported in ppm, multiplicities are indicated by singlet (s), doublet (d), triplet (t), quartet (q), doublet of doublets (dd), doublet of triplets (dt), triplet of doublets (td), multiplet (m). Coupling constants are reported in hertz. All NMR spectra were obtained at room temperature. Mass spectrometry was obtained via a Thermo Scientific Q-Exactive Orbitrap high resolution mass spectrometer. IR spectra were obtained using a Nicolet Avatar E.S.P. 360 FT-IR.

2.6.2 Synthesis of the α -Methylene- γ -lactam (3)

***N*-boc-lactam (1).** The synthesis of **1** was performed in a manner similar to that previously reported by Craven et al.²⁷ A 25 mL, single-necked, round-bottom flask equipped with a 2 cm Teflon-coated magnetic stir bar and a rubber septum was placed in an ice bath, and acetonitrile (6 mL) was added via syringe. 2-pyrrolidinone (1.0 g, 1 equiv, 0.89 mL, 11.8 mmol) was added via syringe, then di-*tert*-butyl-dicarbonate (2.69 g, 1.05 equiv, 12.3 mmol) and 4-*N,N*-dimethylaminopyridine (0.13 g, 0.09 equiv, 1.06 mmol) were added. The solution was maintained at 0 °C for 30 min, then the ice bath was removed, and the reaction mixture was allowed to warm to rt. After 2.5 h at rt, the TLC showed complete disappearance of 2-pyrrolidinone. The reaction mixture was transferred to a 250 mL separatory funnel and diluted with ethyl acetate (13 mL). 1 M HCl (25 mL) was added, the mixture was shaken, and the layers were separated. The aqueous layer was extracted with ethyl acetate (3 \times 13 mL). The combined organic layers were dried over MgSO_4 , filtered, and concentrated by rotary evaporation. The crude residue was purified by silica gel flash column chromatography (2 \times 20 cm SiO_2 column, 75% ethyl acetate/hexanes) to furnish

the title compound **1** in 83% yield (1.8 g). Characterization data corresponds to the literature.²⁷ ¹H NMR (500 MHz, CDCl₃): δ 3.74-3.66 (m, 2 H), 2.48-2.42 (m, 2H), 2.04-1.90 (m, 2 H), 1.48-1.44 (m, 9H); TLC: R_f = 0.31 (50% ethyl acetate/hexanes) [silica gel, UV, KMnO₄].

***N*-boc- α -methylene- γ -lactam (**2**).** The synthesis of **2** was performed in a manner similar to that previously reported by Craven et al.²⁷ A 100 mL, two-necked, round-bottom flask equipped with a 1 cm Teflon-coated magnetic stir bar and a rubber septum was charged with *N*-boc-lactam **1** (1.8 g, 9.7 mmol, 1 equiv). THF (28 mL) was added via syringe, and the flask was placed in a dry ice/acetone bath (−78 °C). Lithium bis(trimethylsilyl)amide (LHMDS) (1.0 M in THF, 12.8 mL, 12.6 mmol, 1.3 equiv) was added via syringe dropwise over 20 min, and the solution was maintained at −78 °C. After 1 h, dimethylmethylenediammonium iodide (2.7 g, 14.6 mmol, 1.5 equiv) was added and the reaction mixture was maintained at −78 °C for 2.5 h. The reaction was warmed to 0 °C by replacing the dry ice/acetone bath with an ice bath. After 30 min, sat. aq. NH₄Cl (75 mL) and H₂O (20 mL) were added to the reaction flask and the mixture was transferred to a separatory funnel and diluted with ethyl acetate (50 mL). The aqueous layer was separated and extracted with ethyl acetate (3 × 50 mL). The combined organic layers were dried over MgSO₄, filtered, and concentrated using rotary evaporation to give dimethyl(methylamine) intermediate as evidenced by ¹H NMR of the residue (2.18 g).

The crude residue (2.18 g, 9.0 mmol, 1 equiv) was transferred to a 100 mL, two-necked, round-bottom flask equipped with a 1 cm Teflon-coated stir bar and two septa. Ethanol (40 mL) and 3-bromo-1-propene (6.2 mL, 72.0 mmol, 8 equiv) were added sequentially via syringe. Sodium carbonate (5.72 g, 54.0 mmol, 6 equiv) was added in a single portion. The mixture was maintained at rt for 18 h, at which time TLC showed complete disappearance of the starting material. The mixture was poured into a Büchner funnel (6 cm) and the solid was removed via

vacuum filtration. The filtrate was transferred to a separatory funnel and sat. aq. NH_4OH (20 mL), H_2O (20 mL), and ethyl acetate (30 mL) were added. The mixture was shaken, the aqueous layer was separated and extracted with ethyl acetate (3×20 mL). The combined organic layers were dried over MgSO_4 , filtered, and concentrated by rotary evaporation to give a residue (1.22 g). The residue was purified by silica gel flash column chromatography (2×20 cm SiO_2 column, 50% ethyl acetate/hexanes) to furnish the title compound **2** in 37% yield (0.71 g) over two steps. Characterization data corresponds to the literature.²⁷ ^1H NMR (500 MHz, CDCl_3): δ 6.09 (t, $J = 3.0$ Hz, 1 H), 5.41 (t, $J = 2.5$ Hz, 1 H), 3.68 (t, $J = 7.5$ Hz, 2 H) 2.77-2.65 (m, 2H), 1.48 (s, 9H); TLC: $R_f = 0.43$ (50% ethyl acetate/hexanes) [silica gel, KMnO_4].

α -methylene- γ -lactam (3). The synthesis of **3** was performed in a manner similar to that previously reported by Craven et al.²⁷ A 50 mL, two-necked, round-bottom flask equipped with a 1 cm Teflon-coated magnetic stir bar and a rubber septum was charged with **2** (0.65 g, 3.28 mmol, 1 equiv). Dichloromethane (25 mL) and trifluoroacetic acid (1.26 mL, 16.4 mol, 5 equiv) were added successively via syringe and the reaction solution was maintained at rt for 2.5 h, at which point TLC showed complete disappearance of starting material. Sat. aq. K_2CO_3 was added dropwise until pH = 10 (pH test strips), and the solution was diluted with H_2O (10 mL). The mixture was transferred to a separatory funnel, and the aqueous layer was separated and extracted with dichloromethane (3×20 mL). The combined organic layers were dried over MgSO_4 , filtered, and concentrated by rotary evaporation. The crude residue was purified by silica gel flash column chromatography (2×20 cm SiO_2 column, acetone) to furnish the title compound **3** in 45% yield (0.319 g). Characterization data corresponds to the literature.²⁷ ^1H NMR (500 MHz, CDCl_3): δ 6.53 (br s, 1H) 6.00 (t, $J = 2.5$ Hz, 1 H), 5.39-5.36 (m, 1 H), 3.44 (t, $J = 6.5$ Hz, 2 H), 2.90-2.84 (m, 2H); TLC: $R_f = 0.18$ (ethyl acetate) [Silica gel, KMnO_4].

2.6.3 General Procedure: *N*-Arylation of Lactams **5a–5m**

The synthesis of lactams **5a–5m** was performed in a manner similar to that previously reported.²⁸ A 5 mL, single-necked, round-bottom flask equipped with a 1 cm Teflon-coated magnetic stir bar and a rubber septum with a nitrogen inlet needle was charged with copper(I) iodide (0.15 equiv) and potassium triphosphate (2 equiv). The aryl iodide (1.5–3 equiv) and *N,N*-dimethylethylenediamine (0.3 equiv), were added to the flask via syringe. In the case that the aryl iodide is solid, it was added along with the copper(I) iodide and potassium phosphate. In a separate scintillation vial, 3-methylene-2-pyrrolidinone (1 equiv) was dissolved in toluene (0.1 M, degassed by bubbling with argon for 20 min), and this solution was transferred all at once to the reaction flask via syringe. The flask was placed in a preheated oil bath (80 °C). After complete disappearance of 3-methylene-2-pyrrolidinone was observed by TLC, the resulting suspension was allowed to cool to rt, and passed through a 1 × 1 cm pad of silica gel, eluting with ethyl acetate. The filtrate was concentrated by rotary evaporation and the residue was purified by silica gel flash column chromatography.

3-Methylene-1-phenyl-2-pyrrolidinone (5a). The synthesis of **5a** was performed according to the General Procedure, using copper(I) iodide (9 mg, 0.05 mmol, 0.15 equiv), potassium triphosphate (0.13g, 0.62 mmol, 2 equiv), iodobenzene (**4a**) (0.1 mL, 0.93 mmol, 3 equiv), *N,N*-dimethylethylenediamine (10 μL, 0.09 mmol, 0.3 equiv), 3-methylene-2-pyrrolidinone (**3**) (30 mg, 0.31 mmol, 1 equiv), and toluene (3 mL), 80 °C, 24 h. Purified by silica gel flash column chromatography (1 × 20 cm, 15% ethyl acetate/hexanes). The title compound **5a** was obtained as a white solid (43 mg, 81% yield). ¹H NMR (400 MHz, DMSO-*d*₆): δ 7.78-7.76 (m, 2 H), 7.43-7.38 (m, 2 H), 7.19-7.15 (m, 1 H), 5.91-5.89 (m, 1 H), 5.47-5.45 (m, 1 H), 3.87 (t, *J* = 6.8 Hz, 2 H), 2.89-2.84 (m, 2 H); ¹³C NMR (100 MHz, DMSO-*d*₆): δ 166.2, 141.1, 139.6, 128.7,

124.3, 119.4, 115.8, 44.6, 23.2; HRMS (TOF MS ES+) m/z : $[M+H]^+$ Calcd for $C_{11}H_{12}NO$ 174.0913; Found 174.0916; IR (ATR) 2907, 1673, 1650, 753 cm^{-1} ; TLC: R_f = 0.67 (ethyl acetate) [silica gel, UV, $KMnO_4$]; mp = 67–71 °C.

3-Methylene-1-[(4-trifluoromethyl)phenyl]-2-pyrrolidinone (5b). The synthesis of **5b** was performed according to the General Procedure, using copper(I) iodide (9 mg, 0.05 mmol, 0.15 equiv), potassium triphosphate (0.13 g, 0.62 mmol, 2 equiv), 1-iodo-4-(trifluoromethyl)benzene (**4b**) (250 mg, 0.93 mmol, 3 equiv), *N,N*-dimethylethylenediamine (10 μ L, 0.09 mmol, 0.3 equiv), 3-methylene-2-pyrrolidinone (**3**) (30 mg, 0.31 mmol, 1 equiv), and toluene (3 mL), 80 °C, 25 h. Purified by silica gel flash column chromatography (1 \times 20 cm, 15% ethyl acetate/hexanes). The title compound **5b** was obtained as a white solid (59 mg, 79% yield). 1H NMR (500 MHz, DMSO- d_6): δ 8.00 (d, J = 8.5 Hz, 2 H), 7.77 (d, J = 8.5 Hz, 2 H), 5.98-5.94 (m, 1 H), 5.55-5.51 (m, 1 H), 3.92 (t, J = 6.5 Hz, 2 H), 2.91-2.88 (m, 2 H); ^{13}C NMR (125 MHz, DMSO- d_6) δ 166.8, 143.0, 140.6, 125.9 (q, J = 3.5 Hz), 124.3 (q, J = 270 Hz), 124.1 (q, J = 32 Hz), 119.1, 117.0, 44.5, 23.0; HRMS (TOF MS ES+) m/z : $[M+H]^+$ Calcd for $C_{12}H_{11}NOF_3$ 242.0787; Found 242.0800; IR (ATR) 2907, 1685, 1655, 850 cm^{-1} ; TLC: R_f = 0.75 (ethyl acetate) [silica gel, UV, $KMnO_4$]; mp = 135–136 °C.

3-Methylene-1-[(4-cyano)phenyl]-2-pyrrolidinone (5c). The synthesis of **5c** was performed according to the General Procedure, using copper(I) iodide (9 mg, 0.05 mmol, 0.15 equiv), potassium triphosphate (0.13 g, 0.62 mmol, 2 equiv), 4-iodobenzonitrile (**4c**) (113 mg, 0.49 mmol, 1.6 equiv), *N,N*-dimethylethylenediamine (10 μ L, 0.09 mmol, 0.3 equiv), 3-methylene-2-pyrrolidinone (**3**) (30 mg, 0.31 mmol, 1 equiv), and toluene (3 mL), 80 °C, 18 h. Purified by silica gel flash column chromatography (1 \times 20 cm, 30% ethyl acetate/hexanes). The title compound **5c** was obtained as a white solid (42 mg, 69% yield). 1H NMR (400 MHz, DMSO- d_6): δ 8.02- 7.97

(m, 2 H), 7.90-7.86 (m, 2 H), 6.00-5.95 (m, 1 H), 5.56-5.53 (m, 1 H), 3.91 (t, $J = 7.2$ Hz, 2 H), 2.91-2.86 (m, 2 H); ^{13}C NMR (100 MHz, DMSO- d_6): δ 167.0, 143.5, 140.5, 133.1, 119.2, 118.9, 117.4, 106.0, 44.5, 23.0; HRMS (TOF MS ES+) m/z : $[\text{M}+\text{H}]^+$ Calcd for $\text{C}_{12}\text{H}_{11}\text{N}_2\text{O}$ 199.0866; Found 199.0871; IR (ATR) 2899, 2228, 1691, 1658, 832 cm^{-1} ; TLC: $R_f = 0.63$ (ethyl acetate) [silica gel, UV, KMnO_4]; mp = 126–126.5 $^\circ\text{C}$.

3-Methylene-1-[(4-methoxy)phenyl]-2-pyrrolidinone (5d). The synthesis of **5d** was performed according to the General Procedure using copper(I) iodide (9 mg, 0.05 mmol, 0.15 equiv), potassium triphosphate (0.13 g, 0.62 mmol, 2 equiv), 1-iodo-4-methoxybenzene (**4d**) (0.22 g, 0.93 mmol, 3 equiv), *N,N*-dimethylethylenediamine (10 μL , 0.09 mmol, 0.3 equiv), 3-methylene-2-pyrrolidinone (**3**) (30 mg, 0.31 mmol, 1 equiv) and toluene (3 mL), 80 $^\circ\text{C}$, 24 h. Purified by silica gel flash column chromatography (1 \times 20 cm, 15% ethyl acetate/hexanes). The title compound **5d** was obtained as a white solid (17 mg, 26% yield). ^1H NMR (500 MHz, DMSO- d_6): δ 7.70-7.65 (m, 2 H), 6.99-6.95 (m, 2 H), 5.88-5.84 (m, 1 H), 5.44-5.41 (m, 1 H), 3.85-3.80 (m, 1 H), 3.75 (s, 3 H), 2.88-2.82 (m, 2 H); ^{13}C NMR: (125 MHz, DMSO- d_6) δ 165.8, 156.1, 141.2, 132.8, 121.1, 115.3 (d, $J = 5$ Hz), 113.9, 55.2 (d, $J = 4.6$ Hz), 44.9, 23.2; HRMS (TOF MS ES+) m/z : $[\text{M}+\text{H}]^+$ Calcd for $\text{C}_{12}\text{H}_{14}\text{NO}_2$ 204.1019; Found 204.1026; IR (ATR) 2914, 1681, 1650, 1249, 833 cm^{-1} ; TLC: $R_f = 0.68$ (ethyl acetate) [silica gel, UV, *p*-anisaldehyde]; mp = 106–107 $^\circ\text{C}$.

3-Methylene-1-[(4-fluoro)phenyl]-2-pyrrolidinone (5e). The synthesis of **5e** was performed according to the General Procedure using copper(I) iodide (9 mg, 0.05 mmol, 0.15 equiv), potassium triphosphate (0.13 g, 0.62 mmol, 2 equiv), 1-fluoro-iodobenzene (**4e**) (107 μL , 0.93 mmol, 3 equiv), *N,N*-dimethylethylenediamine (10 μL , 0.09 mmol, 0.3 equiv), 3-methylene-2-pyrrolidinone (**3**) (30 mg, 0.31 mmol, 1 equiv) and toluene (3 mL), 80 $^\circ\text{C}$, 23 h. Purified by silica gel flash column chromatography (1 \times 20 cm, 15% ethyl acetate/hexanes). The title compound **5e**

was obtained as a white crystalline solid (38 mg, 65% yield). ^1H NMR (500 MHz, DMSO- d_6): δ 7.82-7.77 (m, 2 H), 7.28-7.22 (m, 2 H), 5.90 (td, $J = 2.5, 1.0$ Hz, 1 H), 5.47 (td, $J = 2.5, 1.0$ Hz, 1 H), 3.86 (t, $J = 6.5$ Hz, 2 H), 2.89-2.84 (m, 2 H); ^{13}C NMR (125 MHz, DMSO- d_6): δ 166.1, 158.7 ($J = 240$ Hz), 140.9, 136.0 ($J = 2.0$ Hz), 121.4 ($J = 7.8$ Hz), 116.0, 115.4 ($J = 22$ Hz), 44.8, 23.1; HRMS (TOF MS ES+) m/z : $[\text{M}+\text{H}]^+$ Calcd for $\text{C}_{11}\text{H}_{11}\text{NOF}$ 192.0819; Found 192.0824; IR (ATR) 2915, 1681, 1651, 1392, 831, 737 cm^{-1} ; TLC: $R_f = 0.74$ (ethyl acetate) [silica gel, UV, KMnO_4]; mp = 86–87 $^\circ\text{C}$.

3-Methylene-1-[(4-nitro)phenyl]-2-pyrrolidinone (5f). The synthesis of **5f** was performed according to the General Procedure using copper(I) iodide (9 mg, 0.05 mmol, 0.15 equiv), potassium triphosphate (0.13 g, 0.62 mmol, 2 equiv), 1-iodo-4-nitrobenzene (**4f**) (115 mg, 0.46 mmol, 1.5 equiv), *N,N*-dimethylethylenediamine (10 μL , 0.09 mmol, 0.3 equiv), 3-methylene-2-pyrrolidinone (**3**) (30 mg, 0.31 mmol, 1 equiv) and toluene (3 mL), 80 $^\circ\text{C}$, 24 h. The nitrogen inlet was replaced with an Ar-filled balloon before placing the flask in the oil bath. Purified by silica gel flash column chromatography (1 \times 20 cm, 20% ethyl acetate/hexanes, 30% ethyl acetate/hexanes, and 50% ethyl acetate/hexanes). The title compound **5f** was obtained as a yellow solid (46 mg, 68% yield). ^1H NMR (500 MHz, DMSO- d_6): δ 8.33-8.28 (m, 2 H), 8.08-8.04 (m, 2 H), 6.05-5.95 (m 1 H), 5.59-5.56 (m, 1 H), 3.96 (t, $J = 6.5$ Hz, 2 H), 2.93-2.88 (m, 2 H); ^{13}C NMR (125 MHz, DMSO- d_6) δ 167.1, 145.2, 142.7, 140.3, 124.6, 118.8, 117.7, 44.7, 22.9; HRMS (TOF MS ES+) m/z : $[\text{M}+\text{H}]^+$ Calcd for $\text{C}_{11}\text{H}_{11}\text{N}_2\text{O}_3$ 219.0764; Found 219.0774; IR (ATR) 2909, 1692, 1652, 1505, 817 cm^{-1} ; TLC: $R_f = 0.41$ (50% ethyl acetate/hexanes) [silica gel, UV, KMnO_4]; mp = 171–173 $^\circ\text{C}$.

3-Methylene-1-[(4-(*N,N*-dimethyl)phenyl]-2-pyrrolidinone (5g). The synthesis of **5g** was performed according to the General Procedure using copper(I) iodide (9 mg, 0.05 mmol, 0.15

equiv), potassium triphosphate (0.13 g, 0.62 mmol, 2 equiv), 1-iodo-4-*N,N*-dimethylaniline (**4g**) (114 mg, 0.46 mmol, 1.5 equiv), *N,N*-dimethylethylenediamine (10 μ L, 0.09 mmol, 0.3 equiv), 3-methylene-2-pyrrolidinone (**3**) (30 mg, 0.31 mmol, 1 equiv) and toluene (3 mL), 80 $^{\circ}$ C, 21.5 h. Purified by silica gel flash column chromatography (1 \times 20 cm, 30% ethyl acetate/hexanes). The title compound **5g** was obtained as a pale yellow solid (48 mg, 72% yield). ^1H NMR (500 MHz, DMSO- d_6): δ 7.60-7.54 (m, 2 H), 6.80-6.72 (m, 2 H), 5.84 – 5.80 (m, 1 H), 5.40-5.37 (m, 1 H), 3.80 (t, J = 6.5 Hz, 2 H), 2.89 (s, 6 H), 2.85-2.80 (m, 2 H); ^{13}C NMR (125 MHz, DMSO- d_6): δ 165.5, 147.8, 141.4, 129.3, 120.9, 114.7, 112.4, 44.9, 40.3, 23.3; HRMS (TOF MS ES+) m/z : [M+H] $^{+}$ Calcd for $\text{C}_{13}\text{H}_{16}\text{N}_2\text{O}$ 217.1341; Found 217.1350; IR (ATR) 2894, 1668, 1649, 1176, 808 cm^{-1} ; TLC: R_f = 0.68 (ethyl acetate) [silica gel, UV, KMnO_4]; mp = 108.5–110 $^{\circ}$ C.

3-Methylene-1-[(3-methoxy)phenyl]-2-pyrrolidinone (5h). The synthesis of **4h** was performed according to the General Procedure, using copper(I) iodide (9 mg, 0.05 mmol, 0.15 equiv), potassium triphosphate (0.13 g, 0.62 mmol, 2 equiv), 3-methylene-2-pyrrolidinone (**3**) (30 mg, 0.31 mmol, 1 equiv), *N,N*-dimethylethylenediamine (10 μ L, 0.09 mmol, 0.3 equiv), 3-iodoanisole (**4h**) (53 μ L, 0.46 mmol, 1.5 equiv), and toluene (3 mL), 80 $^{\circ}$ C, 24 h. Purified by silica gel flash column chromatography (1 \times 20 cm, 30% ethyl acetate/hexanes). The title compound **5h** was obtained as a white solid (36 mg, 57% yield). ^1H NMR (400 MHz, DMSO- d_6): δ 7.49-7.45 (m 1 H), 7.35-7.25 (m, 2 H), 6.79-6.74 (m, 1 H), 5.92-5.88 (m, 1 H), 5.48-5.44 (m, 1 H), 3.86 (t, J = 6.4 Hz, 2 H), 3.76 (s, 3 H), 2.89-2.82 (m, 2 H); ^{13}C NMR (100 MHz, DMSO- d_6): δ 166.4, 159.5, 141.2, 140.8, 129.6, 116.0, 111.6, 109.8, 105.6, 55.1, 44.8, 23.1; HRMS (TOF MS ES+) m/z : [M+H] $^{+}$ Calcd for $\text{C}_{12}\text{H}_{14}\text{NO}_2$ 204.1019; Found 204.1026; IR (ATR) 2914, 1676, 1650, 1278, 873, 668 cm^{-1} ; TLC: R_f = 0.79 (ethyl acetate) [silica gel, UV, KMnO_4]; mp = 69–70.5 $^{\circ}$ C.

3-Methylene-1-[(3-fluoro)phenyl]-2-pyrrolidinone (5i). The synthesis of **5i** was performed according to the General Procedure using copper(I) iodide (9 mg, 0.05 mmol, 0.15 equiv), potassium triphosphate (0.13 g, 0.62 mmol, 2 equiv), 3-methylene-2-pyrrolidinone (**3**) (30 mg, 0.31 mmol, 1 equiv), *N,N*-dimethylethylenediamine (10 μ L, 0.09 mmol, 0.3 equiv), 1-fluoro-3-iodobenzene (**4i**) (55 μ L, 0.46 mmol, 1.5 equiv) and toluene (3 mL), 80 °C, 24 h. The reaction flask was wrapped with aluminum foil before being placed in the oil bath. Purified by silica gel flash column chromatography (1 \times 20 cm, 30% ethyl acetate/hexanes). The title compound **5i** was obtained as a white solid (35 mg, 60% yield). ¹H NMR (400 MHz, DMSO-*d*₆): δ 7.78 (app dt, *J* = 12.0 and 2.0 Hz, 1 H), 7.57-7.52 (m, 1 H), 7.48-7.41 (m, 1 H), 7.06-6.97 (m, 1 H), 5.94 – 5.90 (m, 1 H), 5.52 – 5.48 (m, 1 H), 3.87 (t, *J* = 6.8 Hz, 2 H), 2.90-2.84 (m, 2 H); ¹³C NMR (100 MHz, DMSO-*d*₆): δ 166.6, 162.1 (d, *J* = 240 Hz), 141.2 (d, *J* = 10.9 Hz), 140.8, 130.4 (d, *J* = 9.4 Hz), 116.6, 114.8 (d, *J* = 2.8 Hz), 110.8 (d, *J* = 21.0 Hz), 106.2 (d, *J* = 26.3 Hz), 44.7, 23.0; HRMS (TOF MS ES⁺) *m/z*: [M+H]⁺ Calcd for C₁₁H₁₁NOF 192.0819; Found 192.0824; IR (ATR) 2905, 1679, 1653, 1172, 868, 681 cm⁻¹; TLC: *R*_f = 0.68 (ethyl acetate) [silica gel, UV, KMnO₄]; mp = 82–83 °C.

3-Methylene-1-[(3-nitro)phenyl]-2-pyrrolidinone (5j). The synthesis of **5j** was according to the General Procedure using copper(I) iodide (9 mg, 0.05 mmol, 0.15 equiv), potassium triphosphate (0.13 g, 0.62 mmol, 2 equiv), 1-iodo-3-nitrobenzene (**4j**) (115 mg, 0.46 mmol, 1.5 equiv), *N,N*-dimethylethylenediamine (10 μ L, 0.09 mmol, 0.3 equiv), 3-methylene-2-pyrrolidinone (**3**) (30 mg, 0.31 mmol, 1 equiv) and toluene (3 mL), 80 °C, 18.5 h. The nitrogen inlet was then replaced with an Ar-filled balloon before placing the flask in the oil bath. Purified by silica gel flash column chromatography (1 \times 20 cm, 30% ethyl acetate/hexanes). The title compound **5j** was obtained as a fine yellow powder (20 mg, 31% yield). ¹H NMR (500 MHz,

DMSO- d_6): δ 8.84 (app t, J = 2.5 Hz, 1 H), 8.07 (dd, J = 8.0, 2.0 Hz, 1 H), 8.02 (dd, J = 8.0, 2.0 Hz, 1 H), 7.71 (t, J = 8.0 Hz, 1 H), 6.00-5.95 (m, 1 H), 5.57-5.52 (m, 1 H), 3.95 (t, J = 7.0 Hz, 2 H), 2.95-2.86, (m, 2H); ^{13}C NMR (125 MHz, DMSO- d_6): δ 166.9, 147.9, 140.5, 140.4, 130.2, 124.9, 118.6, 117.1, 113.4, 44.6, 23.0; HRMS (TOF MS ES+) m/z : $[\text{M}+\text{H}]^+$ Calcd for $\text{C}_{11}\text{H}_{11}\text{N}_2\text{O}_3$ 219.0764; Found 219.0775; IR (ATR) 3127, 2980, 1682, 1656, 1526, 894 cm^{-1} ; TLC: R_f = 0.46 (ethyl acetate) [silica gel, UV, KMnO_4]; mp = 139.3–141.7 $^\circ\text{C}$.

3-Methylene-1-[(2-methoxy)phenyl]-2-pyrrolidinone (5k). The synthesis of **5k** was performed according to the General Procedure, using copper(I) iodide (9 mg, 0.05 mmol, 0.15 equiv), potassium triphosphate (0.13 g, 0.62 mmol, 2 equiv), 3-methylene-2-pyrrolidinone (**3**) (30 mg, 0.31 mmol, 1.0 equiv), *N,N*-dimethylethylenediamine (10 μL , 0.09 mmol, 0.3 equiv), 2-iodoanisole (**4k**) (60 μL , 0.46 mmol, 1.5 equiv) and toluene (3 mL), 80 $^\circ\text{C}$, 23 h. Purified by silica gel flash column chromatography (1 \times 15 cm, 30% ethyl acetate/hexanes). The title compound **5k** was obtained as a light yellow/transparent oil that solidified on standing (38 mg, 60% yield). ^1H NMR (400 MHz, DMSO- d_6): δ 7.37-7.07 (m, 3 H), 7.03-6.94 (m, 1H), 5.84-5.77 (m, 1H), 5.44-5.40 (m, 1H), 3.78 (s, 3H), 3.68 (t, J = 6.8 Hz, 2H), 2.93-2.84 (m, 2H); ^{13}C NMR (100 MHz, DMSO- d_6): δ 166.5, 154.6, 140.4, 128.8, 128.4, 127.3, 120.5, 115.2, 112.4, 55.6, 46.0, 24.2; HRMS (TOF MS ES+) m/z : $[\text{M}+\text{H}]^+$ Calcd for $\text{C}_{12}\text{H}_{14}\text{NO}_2$ 204.1019; Found 204.1027; IR (ATR) 2907, 1685, 1658, 1276, 762 cm^{-1} ; TLC: R_f = 0.23 (50% ethyl acetate/hexanes) [silica gel, UV, KMnO_4]; mp = 81.5–83 $^\circ\text{C}$.

3-Methylene-1-[(2-fluoro)phenyl]-2-pyrrolidinone (5l). The synthesis of **5l** was performed according to the General Procedure using copper(I) iodide (9 mg, 0.05 mmol, 0.15 equiv), tripotassium phosphate (0.13 g, 0.62 mmol, 2 equiv), 3-methylene-2-pyrrolidinone (**3**) (30 mg, 0.31 mmol, 1 equiv), *N,N*-dimethylethylenediamine (10 μL , 0.09 mmol, 1 equiv), 2-

fluoriodobenzene **4l** (54 μ L, 0.46 mmol, 1.5 equiv) and toluene (3 mL) 80 °C, 25 h. Purified by silica gel flash column chromatography (1 \times 15 cm, 30% ethyl acetate/hexanes). The title compound **5l** was obtained as a white crystalline solid (48 mg, 81% yield). ^1H NMR (400 MHz, DMSO- d_6): δ 7.51 (app ddd, J = 15.6, 7.6, 1.6 Hz, 1H), 7.41-7.22 (m, 3H), 5.90-5.86 (m, 1H), 5.50-5.47 (M, 1H), 3.79 (t, J = 6.8 Hz, 2H), 2.96-2.88 (m, 2H); ^{13}C NMR (100 MHz, DMSO- d_6): δ 166.2, 156.6 (d, J = 249.2 Hz), 139.8, 128.8 (d, J = 8.0 Hz), 127.7 (d, J = 1.8 Hz), 126.5 (d, J = 12.1 Hz), 124.8 (d, J = 3.6 Hz), 116.5 (d, J = 20.0 Hz), 116.1, 46.1, 24.3; HRMS (TOF MS ES+) m/z : $[\text{M}+\text{H}]^+$ Calcd for $\text{C}_{11}\text{H}_{11}\text{NOF}$ 192.0819; Found 192.0824; IR (ATR) 2906, 1685, 1657, 1261, 756, 668 cm^{-1} ; TLC: R_f = 0.80 (ethyl acetate) [silica gel, UV, KMnO_4]; mp = 80–82 °C.

3-Methylene-1-[(2-nitro)phenyl]-2-pyrrolidinone (5m). The synthesis of **5m** was performed according to the General Procedure using copper(I) iodide (9 mg, 0.05 mmol, 0.15 equiv), potassium triphosphate (0.13 g, 0.62 mmol, 2 equiv), 1-iodo-3-nitrobenzene (**4m**) (115 mg, 0.46 mmol, 1.5 equiv), *N,N*-dimethylethylenediamine (10 μ L, 0.09 mmol, 0.3 equiv), 3-methylene-2-pyrrolidinone (**3**) (30 mg, 0.31 mmol, 1 equiv), and toluene (3 mL) 80 °C, 72 h. Purified by silica gel flash column chromatography (1 \times 20 cm, 30% ethyl acetate/hexanes). The title compound **5m** was obtained as a yellow oil (54 mg, 80% yield). ^1H NMR (400 MHz, DMSO- d_6): δ 7.99 (dd, J = 8.0, 1.6 Hz, 1 H), 7.83-7.78 (m, 1 H), 7.68 (dd, J = 8.4, 1.6 Hz, 1 H), 7.57-7.51 (m, 1 H), 5.87-5.84 (m, 1 H), 5.53-5.50 (m, 1 H), 3.97 (t, J = 6.8 Hz, 2 H), 2.97-2.91 (m, 2 H); ^{13}C NMR (100 MHz, DMSO- d_6): δ 166.3, 145.0, 139.4, 134.1, 131.5, 127.5, 126.2, 125.1, 117.1, 45.9, 24.2; HRMS (TOF MS ES+) m/z : $[\text{M}+\text{H}]^+$ Calcd for $\text{C}_{11}\text{H}_{11}\text{N}_2\text{O}_3$ 219.0764; Found 219.0762; IR (ATR) 2895, 1693, 1658, 1525, 755 cm^{-1} ; TLC: R_f = 0.25 (50% ethyl acetate/hexanes) [silica gel, UV, KMnO_4]; mp = 111–114.5 °C.

3.0 Cu-Catalyzed Hydroboration of Benzyldenecyclopropanes and Benzyldenecyclobutanes

Medina, J. M., Kang, T., Shao, **Erbay, T. G.**, H., Gallego, G. M., Yang, S., Tran-Dubé, M., Richardson, P. F., Derosa, J., Helsel, R., Patman, R. L., Wang, F., Ashcroft, C., Braganza, J. F., McAlpine, I., Liu, P., Engle, K. M. “Cu-Catalyzed Hydroboration of Benzyldenecyclopropanes: Reaction Optimization, (Hetero)Aryl Scope, and Origins of Pathway Selectivity”. *ACS Catal.* **2019**, *9*, 11130–11136.

Kang, T., **Erbay, T. G.**, Xu, K. L., Gallego, G. M., Burtea, A., Nair, S. K., Patman, R. L., Zhou, R., Sutton, S. C., McAlpine, I. J., Liu, P., Engle, K. M. “Multifaceted Substrate–Ligand Interactions Promote the Copper-Catalyzed Hydroboration of Benzyldenecyclobutanes and Related Compounds”. *ACS Catal.* **2020**, *10*, 13075–13083.

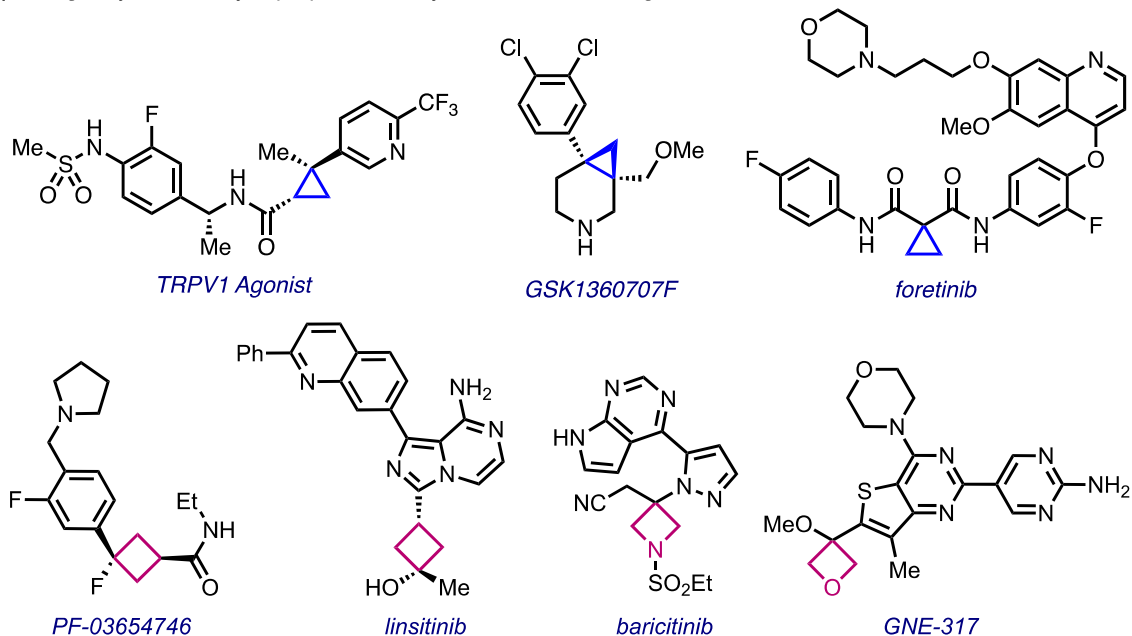
In this work, I designed and carried out the DFT calculations and analyzed the computational results. Synthesis of compounds and kinetic studies were carried out by Medina, J. M., Kang, T., Gallego, G. M., Yang, S., Tran-Dubé, M., Richardson, P. F., Derosa, J., Helsel, R., Burtea, A., Nair, S. K., Zhou, R., Sutton, S. C., Patman, R. L., Wang, F., Ashcroft, C., Braganza, J. F., McAlpine, I., Engle, K. M. at the Scripps Research Institute and Pfizer Oncology Medicine.

3.1 Introduction

Conformationally constrained small carbocyclic ring systems are among the most important motifs in modern organic chemistry and drug discovery.⁴⁷⁻⁴⁸ Cyclopropane (CP) and cyclobutane (CB) substructures are of special importance as they can provide a molecule with unique properties, such as increased potency, metabolic stability, and brain permeability, as well as attenuated pK_a and lipophilicity,⁴⁹⁻⁵⁰ and are present in a wide range of biologically relevant molecules and pharmaceuticals (**Figure 3.1a**).⁵¹⁻⁵⁶ Accessing CP and CB motifs with diverse substitution patterns is often a challenging aspect of the synthesis of such compounds. Organoboron chemistry, particularly the boronic ester synthesis is a useful tool in synthetic chemistry to construct carbon–carbon and carbon–heteroatom bonds,⁵⁷ and facilitates the preparation of versatile building blocks that can be further elaborated (**Figure 3.1b**).⁵⁸

Using the copper-catalyzed hydroboration of benzyldenecyclopropanes (BCPs) and benzyldenecyclobutanes (BCBs), a convenient and reliable method that proceeds under mild conditions and exhibits broad functional group tolerance to access tertiary cyclopropyl- and cyclobutylboronates bearing diverse $-\text{CH}_2\text{Ar}/\text{Het}$ substitution at the α -position was developed by the Engle Group (**Figure 3.2a**).⁵⁹⁻⁶⁰ The Cu-catalyzed hydroboration of BCPs undergoes via two competitive reaction pathways from the common intermediate **IM3**.⁶¹ Alkenylboronates **2** are generated if β -carbon elimination of **IM** is preferred over protodecupration (path A, Ligand 1 = dppe), whereas direct protodecupration of **IM** would generate cyclopropylboronic esters **3** (path B, Ligand 2 = *rac*-BINAP) (**Figure 3.2a**). By tuning the ligand sphere around the metal, it is possible control the pathway selectivity of this process and enable straightforward access to both types of building blocks.

a) Biologically relevant cyclopropane- and cyclobutane-containing molecules



b) Examples to the utility of tertiary boronic ester in organic synthesis

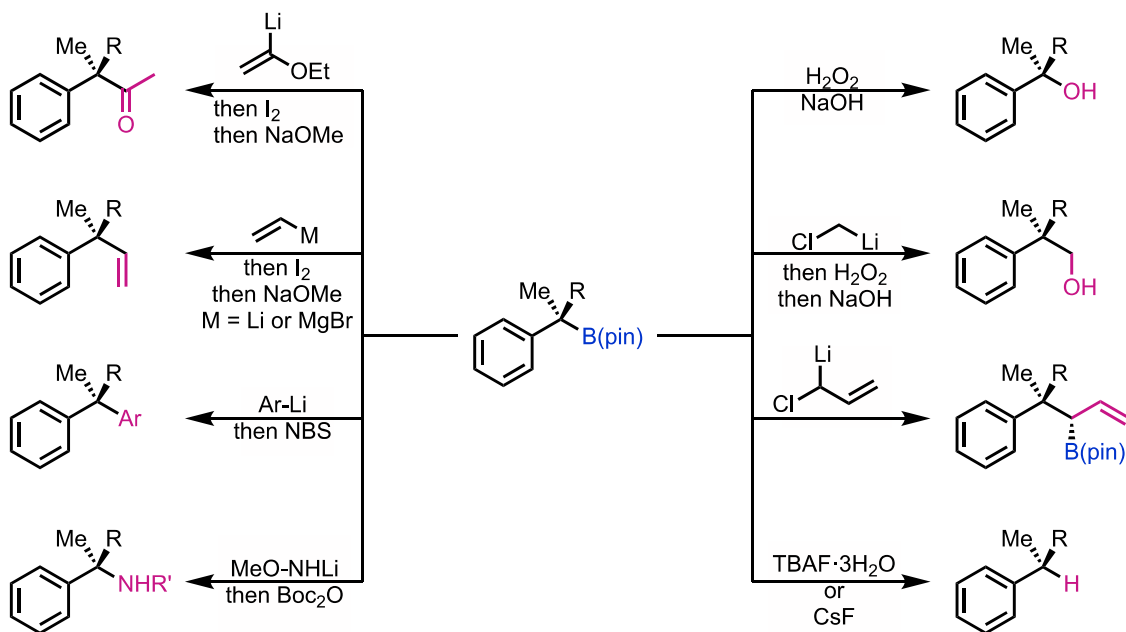
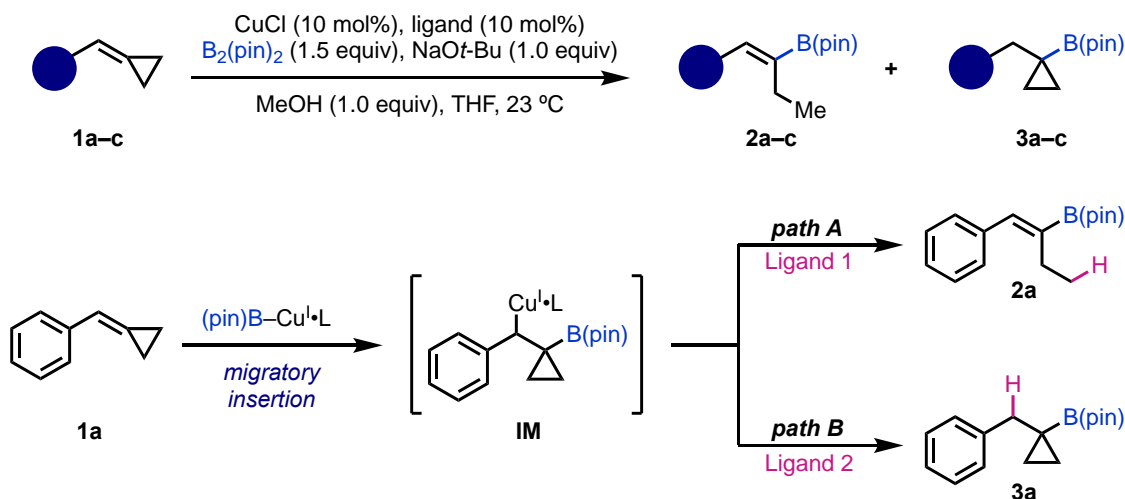


Figure 3.1. a) Biologically relevant cyclopropane- and cyclobutane-containing molecules. b) Tertiary boronic esters are useful in synthetic chemistry to construct C–C and C–Heteroatom bonds. Adapted with permission from Acc. Chem. Res. 2014, 47, 3174–3183. Copyright 2014 American Chemical Society.

Experimental studies showed that with BCB substrates, the alkenylboronate product **2d** is not observed, and the reaction yields the protodecupration product, boronic ester **3d** only (**Figure 3.2b**).

a. Pathway selectivity in Cu-catalyzed hydroboration of BCPs



b. Ligand-substrate interaction effects on the rates of migratory insertion in BCBs

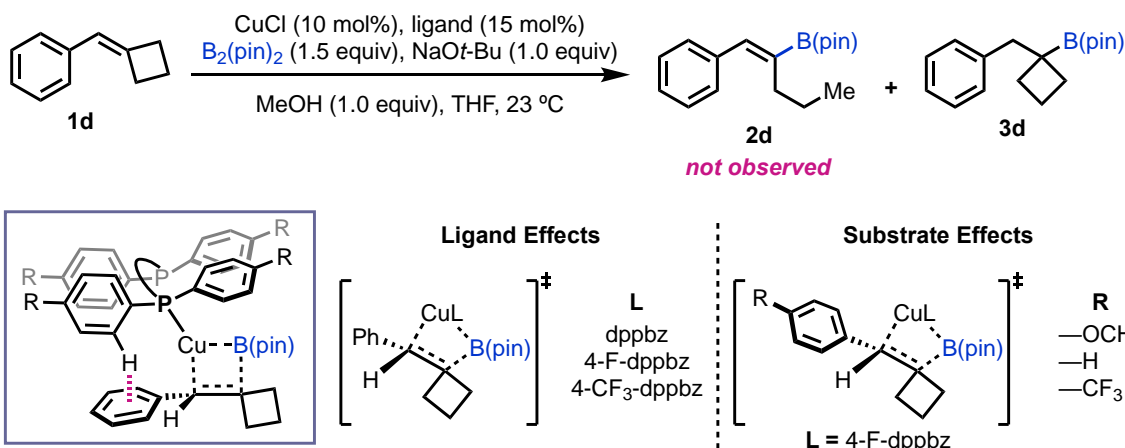


Figure 3.2. a) Tuning of ligand sphere enables pathway selectivity in Cu-catalyzed hydroboration of BCPs. b) Ligand–substrate interaction effects on the rates of migratory insertion in BCBs are elaborated using EDA methods.

Ligand screening studies demonstrated that dppbz ligands successfully effect the hydroboration of BCBs, and the electron withdrawing groups installed on the ligand improve the rate of migratory insertion, along with the reaction yields.

To understand the ligand–substrate interactions on the reactivity of Cu-catalyzed hydroboration of benzyldenecyclobutanes, the energy decomposition analysis (EDA) approach is utilized. Exploiting non-covalent ligand–substrate interactions are important for catalyst design. π -stacking interactions, cation- and anion- π interactions, XH- π interactions (where X = B, N, O, or a halogen), and lone pair- π interactions have been utilized to achieve various transformations, modify product outcomes, and improve the reaction yields.⁶² However, computational methods to understand the nature of non-covalent ligand–substrate interactions, in particular, the exact contributions from different types of interactions, are rare. The EDA methods have been utilized to develop a quantitative understanding of contributions to chemical bonding as well as non-bonding interactions,⁶³⁻⁶⁴ to understand the reaction pathways,⁶⁵ chemical bonding in extending systems for materials science,⁶⁶ to understand biomolecular systems,⁶⁷ and more recently, to improve the reactivity in transition metal-catalyzed reactions.⁶⁸⁻⁶⁹ Studies of computational models to analyze the influence of different catalyst–substrate interactions quantitatively for CuH-catalyzed hydroamination of olefins, utilizing EDA methods to enhance the reactivity of the copper catalysts have been reported by our group recently.⁶⁸⁻⁶⁹

The interesting pathway selectivity in the hydroboration of BCPs with different bisphosphine ligands, and the increased reaction rates of the hydroboration of BCBs with modified dppbz ligands prompted us to seek for a thorough, computational understanding of the factors affecting the experimental outcomes. In this chapter, the mechanism of hydroboration of benzyldenecyclopropanes (BCPs) and benzyldenecyclobutanes (BCBs), the influence of the

ligands on the pathway selectivity in the hydroboration of BCPs (**Figure 3.2a**), and the influence of ligand–substrate interactions on the reaction rates of the BCBs (**Figure 3.2b**) are studied using DFT and EDA methods.

3.2 Computational Methods

Geometry optimizations and single point energy calculations were carried out using Gaussian 16.³⁰ Geometries of intermediates and transition states were optimized using the M06L functional³¹ with a mixed basis set of LANL2DZ for Cu and 6-31G(d) for other atoms in the gas phase. Vibrational frequency calculations were performed for all the stationary points to confirm if each optimized structure is a local minimum or a transition state structure. Solvation energy corrections were calculated in THF solvent with the SMD solvation model³⁶ based on the gas-phase optimized geometries. The M06 functional with a mixed basis set of SDD for Cu and 6-311+G(d,p) for other atoms was used for single point energy calculations.⁷⁰ Gibbs free energies were calculated at the standard conditions (298K, 1 mol/L) using Cramer and Truhlar’s quasiharmonic approximation³⁴ using Goodvibes v2.0.1.³⁵ Images of structures were generated using CYLview.³⁹ Energy decomposition analysis calculations were performed using the second generation ALMO-EDA method implemented in Q-Chem 5.2,⁷¹ using the M06 functional with a mixed basis set of SDD for Cu and 6-311+G(d,p) with SMD solvation model in THF.

The computed activation energy for each reaction is dissected using the following equation:

$$\Delta E^\ddagger = \Delta E_{\text{dist}} + \Delta E_{\text{int-bond}} + \Delta E_{\text{int-space}}$$

where the distortion energy (ΔE_{dist}) is the sum of the energies required to distort the LCu–B(pin) complex and the substrate into their transition state geometries. The through-space interaction

energy between the phosphine ligand and the benzyldenecyclobutane substrate ($\Delta E_{\text{int-space}}$) is calculated from the interaction energy of a hypothetical supramolecular complex of the ligand and the substrate at the transition state geometry in the absence of the CuB(pin) moiety.

$$\Delta E_{\text{int-space}} = E_{\text{ligand+substrate}} - E_{\text{ligand}} - E_{\text{substrate}}$$

The rest of the catalyst/substrate interaction energy is defined as the through-bond interaction ($\Delta E_{\text{int-bond}}$) between the LCuB(pin) and the substrate in the transition state.

$$\Delta E_{\text{int-bond}} = \Delta E^{\ddagger} - \Delta E_{\text{dist}} - \Delta E_{\text{int-space}}$$

Using the second-generation ALMO-EDA method implemented in Q-Chem 5.2, the through-space interaction energy ($\Delta E_{\text{int-space}}$) is further dissected according to the following equation:

$$\Delta E_{\text{int-space}} = \Delta E_{\text{elstat}} + \Delta E_{\text{pauli}} + \Delta E_{\text{disp}} + \Delta E_{\text{pol}} + \Delta E_{\text{ct}}$$

where ΔE_{elstat} , ΔE_{pauli} , ΔE_{disp} , ΔE_{pol} , and ΔE_{ct} correspond to several different types of non-covalent interactions, namely electrostatic, Pauli repulsions, dispersion interactions, intrafragment polarization, and interfragment charge transfer, respectively.

3.3 Ligand Effects on the Pathway Selectivity of Cu-Catalyzed Hydroboration of Benzyldenecyclopropanes

The summary of experimental results for the hydroboration of representative substrates are presented in Table 3.1. At first glance, despite the results varied from substrate to substrate, a clear correlation between the electron-donating character of the ligand and the propensity for β -carbon elimination, which leads to formation of alkenylboronates **2**, is observed. The bisphosphine ligands containing two $-\text{PPh}_2$ arms with varied natural bite angles (β_n) showed discrepancy between

outcomes, such as dppm (entry 1) with a small bite angle ($\beta_n = 72^\circ$) favors the formation of product **3**, whereas dppe ($\beta_n = 85^\circ$, entry 3), which is known to bind copper with a larger bite angle than dppm and dppbz favored formation of alkenylboronates **2**.

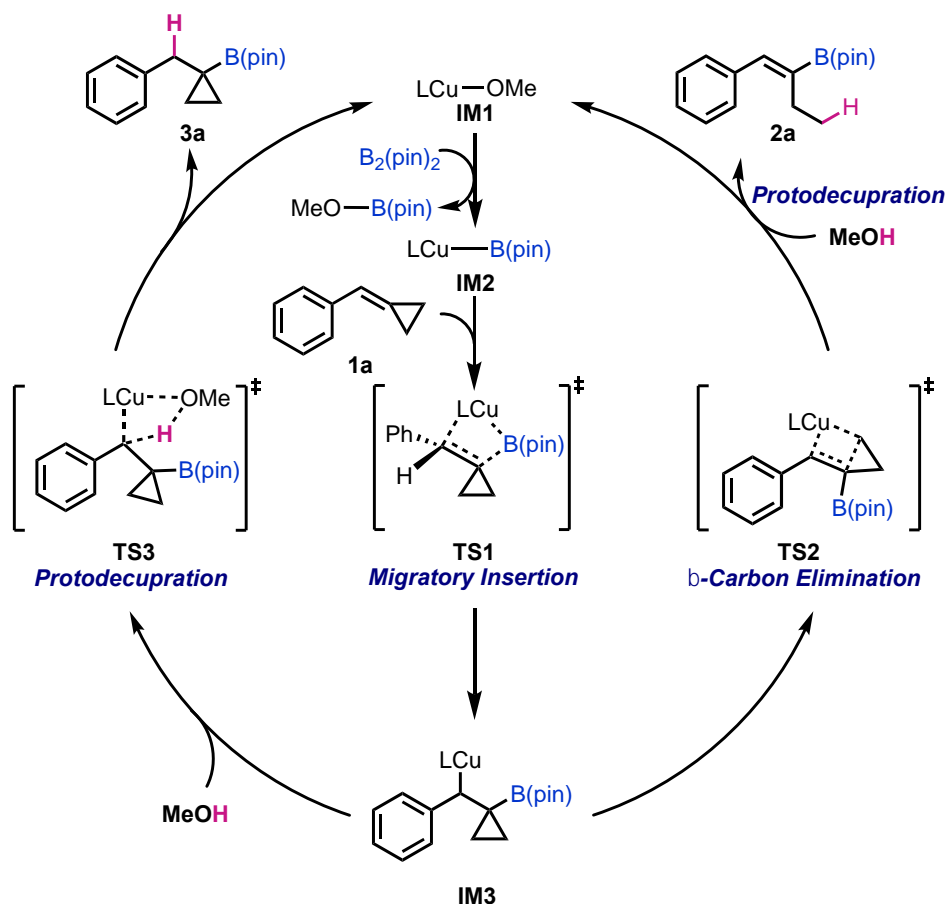
Table 3.1. Summary of ligand optimization with representative substrates.

entry	ligand	β_n	product ratio (2 : 3) in % yield		
1	dppm	72°	21 : 70	6 : 93	0 : 55
2	dppbz	83°	88 : 0	72 : 32	66 : 21
3	dppe	85°	93 : 0	76 : 6	70 : 16
4	<i>rac</i> -BINAP	92°	0 : 79	6 : 83	0 : 91
5	xantphos	111°	0 : 71	0 : 34	0 : 41

Larger bite angle ligands (entries 4 and 5) such as *rac*-BINAP ($\beta_n = 92^\circ$) and xantphos ($\beta_n = 111^\circ$) switched the selectivity to favor product **3**. To understand the discrepancy between outcomes obtained with seemingly related bisphosphine ligands under otherwise identical reaction conditions, we pursued a further understanding of the ligand effects with computational studies.

The proposed mechanisms of the Cu-catalyzed hydroboration of benzylidenecyclopropanes (BCP) are presented in **Scheme 3.1**. The LCu(I)–OR complex first

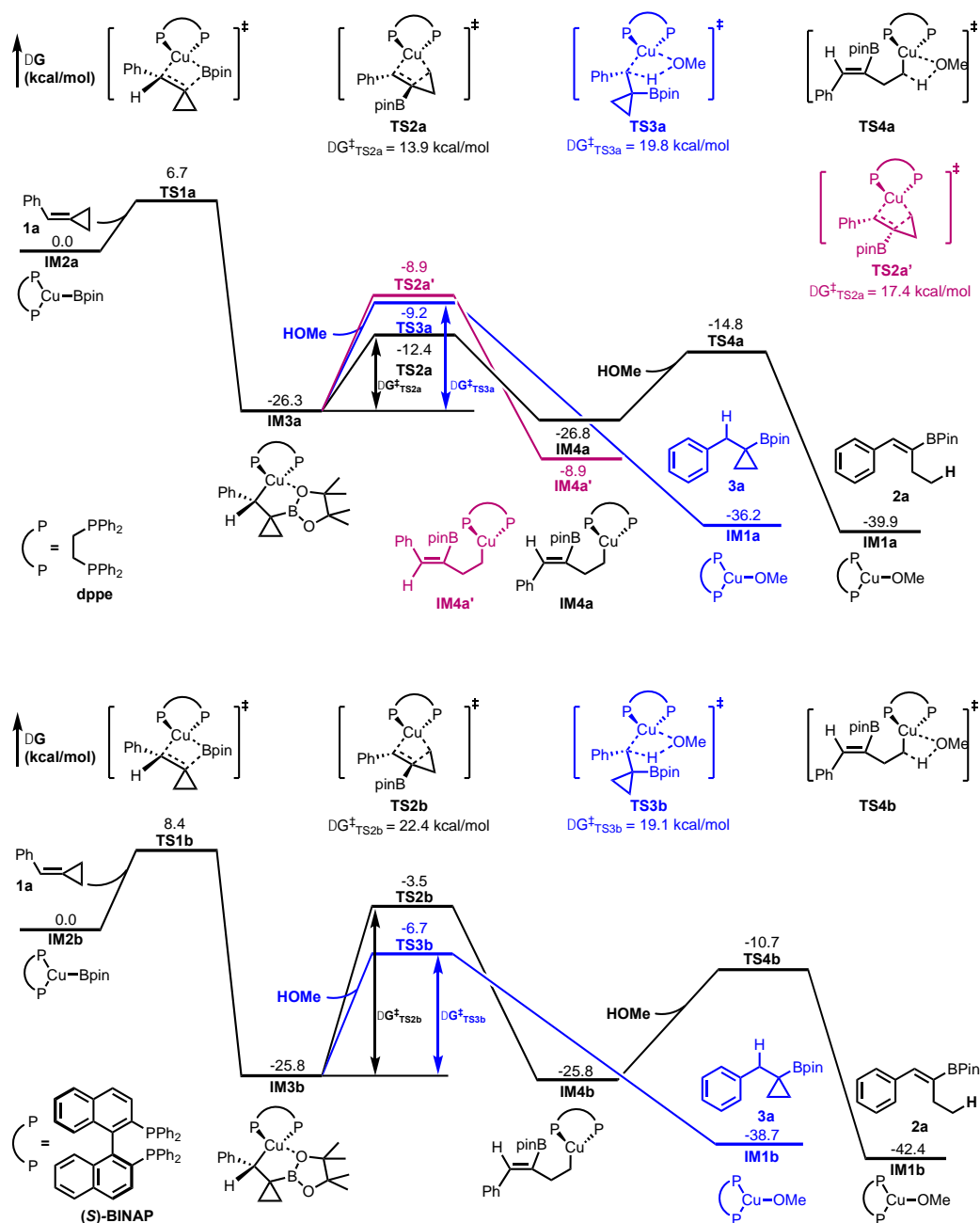
undergoes borylation with $B_2(\text{pin})_2$ to form the $\text{LCu(I)}\text{--B(pin)}$ intermediate **IM2**. Subsequent migratory insertion of the BCP substrate **1a** into $\text{LCu(I)}\text{--B(pin)}$ via **TS1** forms benzylic copper(I) complex **IM3** irreversibly, a key common intermediate to form both alkenylboronates (**2a**) and boronic esters (**3a**). The two different products are generated through distinct transition states. Protodecupration (**TS3**) of **IM3** releases the boronic ester product **3a** and regenerates **IM1**. Conversely, β -carbon elimination (**TS2**) may take place to cleave the cyclopropane ring. A subsequent protodecupration (**TS4**) would then form the alkenylboronate product **2a**. In both pathways, the $\text{LCu(I)}\text{--OR}$ complex is regenerated after the protodecupration step.



Scheme 3.1. Proposed reaction mechanism for hydroboration of benzylidencyclopropanes.

The computed energy profiles for the two competing pathways with the dppe- and (*S*)-BINAP-supported Cu(I)–B(pin) complexes are shown in **Scheme 3.2**. In reactions using both dppe and (*S*)-BINAP ligands, the key intermediates **IM3a** and **IM3b** are generated via an irreversible BCP migratory insertion (**TS1a** and **TS1b**). In reaction with the (*S*)-BINAP ligand, the Cu–B(pin) complex preferentially adds to the *Re*-face of the BCP double bond, leading to the (*R*)-benzylic Cu(I) complex **IM3b**. Addition to the opposite face of BCP (*vide infra*) requires higher barrier. Nonetheless, this newly formed benzylic chiral center is ablated in subsequent steps, eventually leading to achiral products in both pathways depicted in **Scheme 3.2**.

The benzylic Cu(I) intermediates **IM3a** and **IM3b** adopt a distorted tetrahedral conformation with one of the oxygen atoms on B(pin) datively bonded onto the Cu center, where the distortion from the tetrahedral geometry is more substantial in the (*S*)-BINAP-bound species **IM3b**. From the dppe-supported complex **IM3a**, the β -carbon elimination transition state (**TS2a**) is more favorable over protodecupration (**TS3a**) by 3.2 kcal/mol, leading to the formation of the alkenylboronate product **2a**. The most favorable β -carbon elimination transition state (**TS2a**) places the Ph and B(pin) groups on the opposite sides of the double bond, leading to the experimentally observed *Z*-stereoisomer of the alkenylboronate. Another β -carbon elimination transition state (**TS2a'**), which would eventually lead to the *E*-stereoisomer of the alkenylboronate, is 3.5 kcal/mol less stable than **TS2a**.

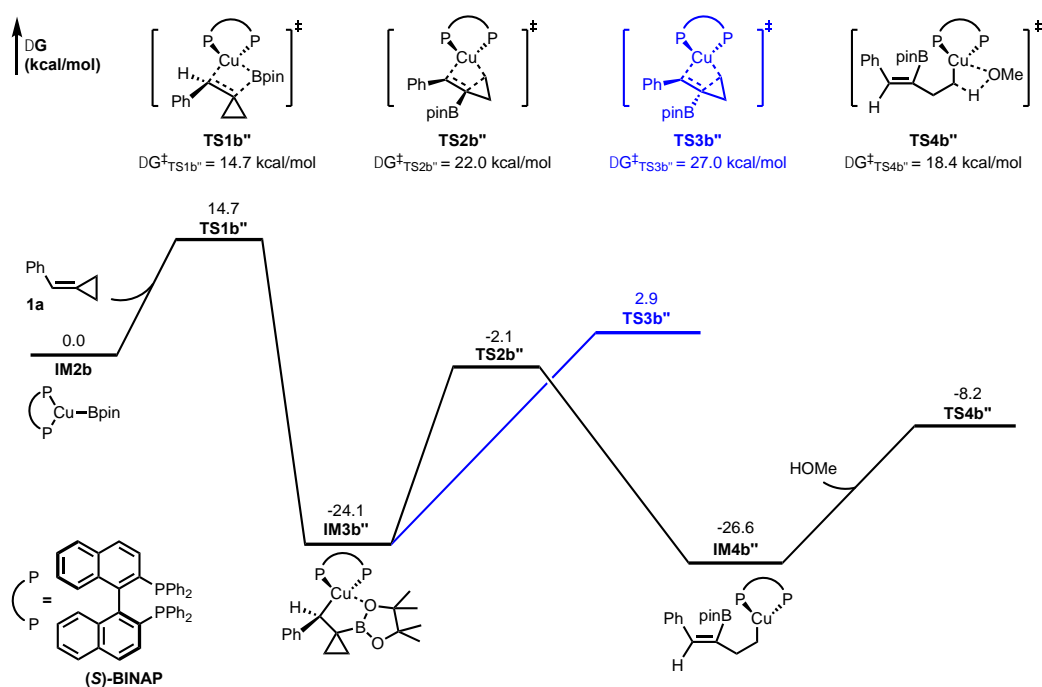


Scheme 3.2. Computed reaction energy profiles of the hydroboration of benzylidenecyclopropane **1** with dppe (top)- and (*S*)-BINAP (bottom)-supported Cu catalysts.

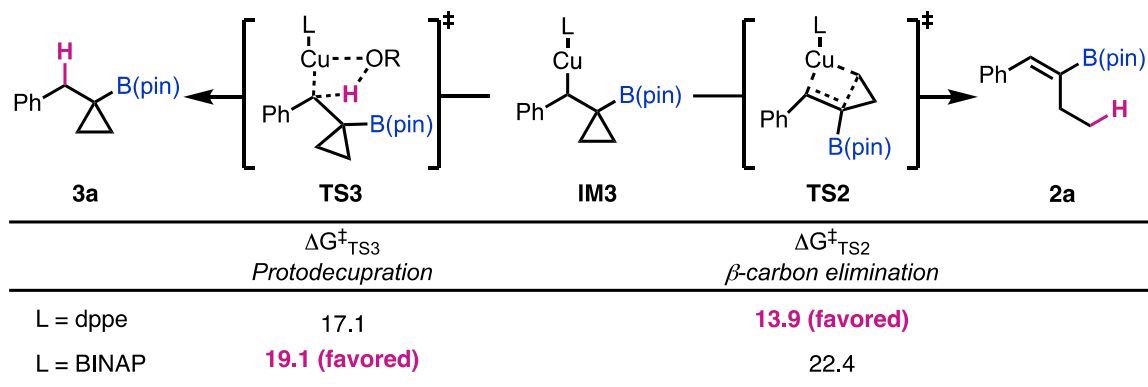
In contrast, the (*S*)-BINAP-supported complex **IM3b** favors the protodecupration (**TS3b**) over β -carbon elimination (**TS2b**) by 3.2 kcal/mol, leading to the formation of the boronic ester.

This less favorable β -carbon elimination transition state, **TS2b**, would eventually lead to the *Z*-alkenylboronate. The β -carbon elimination to form the *E*-double bond is expected to be even less favorable, because of the steric repulsions between Ph and B(pin) groups. However, after multiple attempts, this β -carbon elimination transition state still cannot be located, because of the unfavorable steric interactions in this transition state. Overall, the computational studies indicated the hydroboration reaction with the dppe-supported Cu catalyst favors the *Z*-alkenylboronate **2a**, while the use of (*S*)-BINAP-supported Cu catalyst leads to the cyclopropylboronic ester **3a**. This reversal of product selectivity is in good agreement with experiment.

We also considered the alternative pathway with the (*S*)-BINAP ligand that initiates via the LCu(I)–B(pin) complex adding to the opposite face of the BCP π -bond. The computed energy profile in this pathway is shown in **Scheme 3.3**. The calculations suggest this pathway is much less favorable because the initial migratory insertion (**TS1b''**) is much less favorable than the competing pathway via **TS1b**. The calculations suggest that the pathway selectivity is determined by the activation energy difference between β -carbon elimination (**TS2**) and protodecupration (**TS3**) from the benzylic copper intermediate **IM3** formed via the irreversible migratory insertion of the BCP **1a** (**Scheme 3.4**).



Scheme 3.3. Alternative diastereomeric TS with the (S)-BINAP-supported Cu catalyst.



Scheme 3.4. Summary of pathway selectivity.

Consistent with the experimental observations, with the dppe ligand, the β -carbon elimination is favored over protodecupration by 3.2 kcal/mol, leading to the formation of the alkenylboronate product **2a**. The use of BINAP ligand completely reverses the pathway selectivity. β -carbon elimination from the benzylic copper complex with BINAP as ligand requires a much

higher barrier ($\Delta G^\ddagger = 22.4$ kcal/mol) than that with dppe as ligand ($\Delta G^\ddagger = 13.9$ kcal/mol). On the other hand, ligand effects have a much smaller impact on the barrier of protodecupration (**TS2**). Therefore, the reaction using BINAP as ligand forms the cyclopropylboronic ester **3a** via favorable protodecupration. The origin of ligand effects on the β -carbon elimination barrier can be visualized in the quadrant diagrams in **Figure 3.3**.

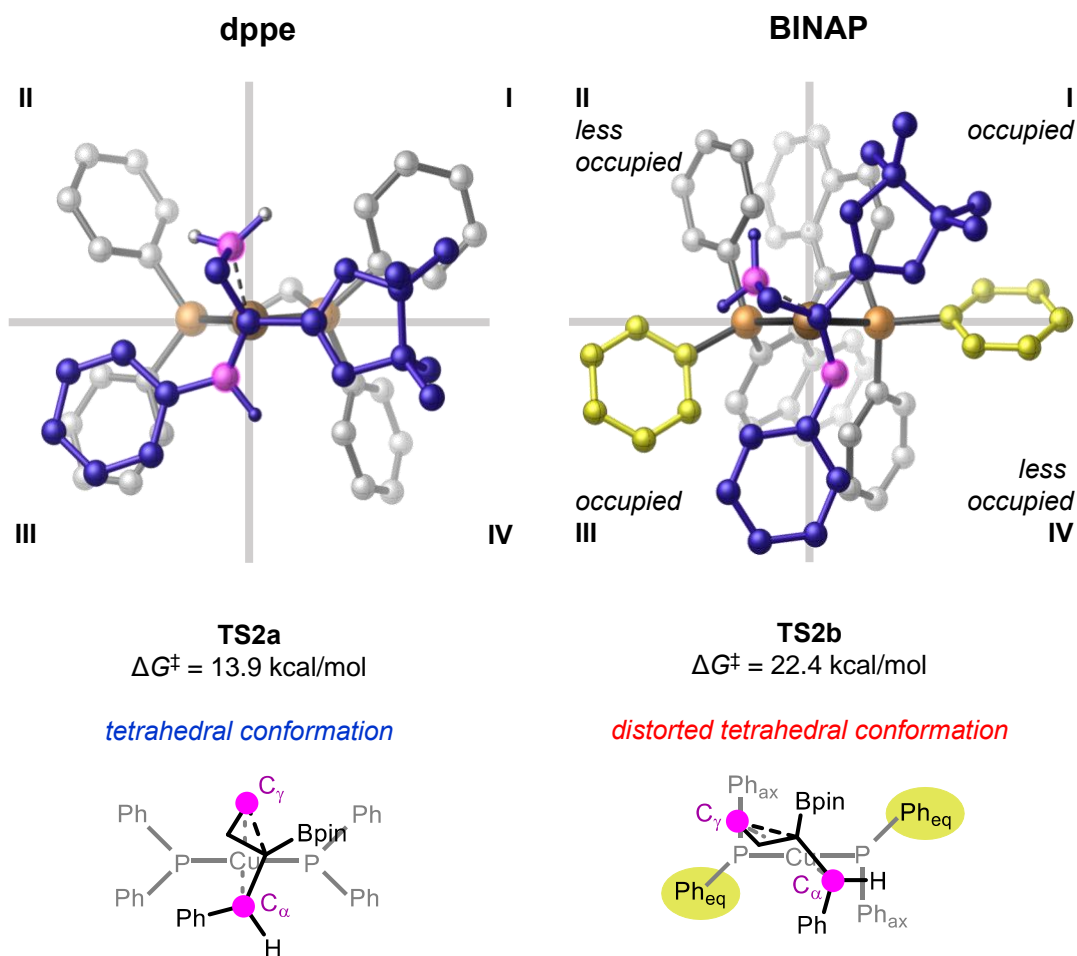


Figure 3.3. Ligand effects on the β -carbon elimination transition states.

The β -carbon elimination TS with the Cu(I) center prefers a tetrahedral geometry that places the benzylic (C_α) and γ -carbons (C_γ) within the vertical region perpendicular to the P–Cu–

P plane. With the dppe ligand, this vertical region is not occupied by the $-\text{PPh}_2$ arms. Thus, no unfavorable steric repulsions are observed in **TS2a**. On the other hand, the more rigid BINAP ligand is confined to a C_2 -symmetric conformation, in which the vertical region is blocked by the pseudoaxial phenyl groups (Ph_{ax}) of the $-\text{PPh}_2$ arms. The benzylic and γ -carbons in **TS2b** are significantly distorted to be placed in the less occupied diagonal regions in quadrants **II** and **IV** to avoid repulsions with the BINAP ligand. Consequently, the distorted tetrahedral **TS2b** is energetically disfavored (**Figure 3.3**).

An isomer of **TS2b** that places C_α and C_γ in the more occupied **I** and **III** quadrants was also located, **TS2b'**, which requires an even higher activation energy (26.7 kcal/mol). In **TS2b'**, the γ - and benzylic carbons are placed in the more occupied quadrants **I** and **III**. Therefore, greater steric repulsions with the ligand are observed in **TS1b'** (**Figure 3.4**).

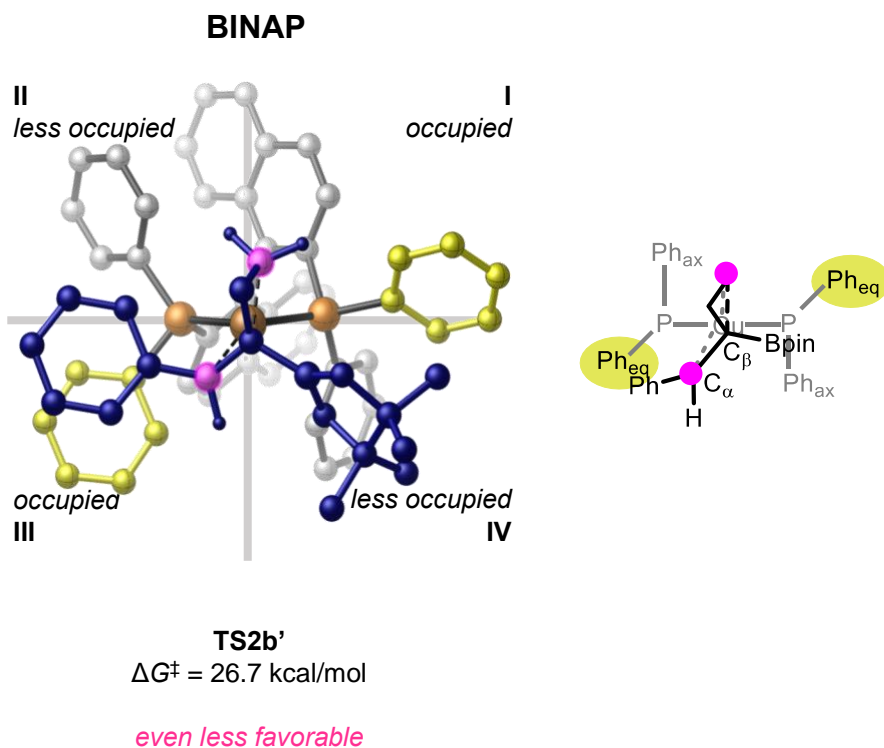


Figure 3.4. Alternative β -carbon elimination transition state with BINAP-supported catalyst.

In contrast, the ligand steric effects have a smaller impact on the geometry and energy of the protodecupration transition states, which are less sterically congested (**TS3a** and **TS3b**, **Figure 3.5**). These transition states have comparable activation energies, and are less crowded than the β -carbon elimination transition states due to a smaller substrate bite angle. Therefore, both **TS3a** and **TS3b** experience smaller ligand–substrate steric repulsions and are less distorted from the tetrahedral geometry.

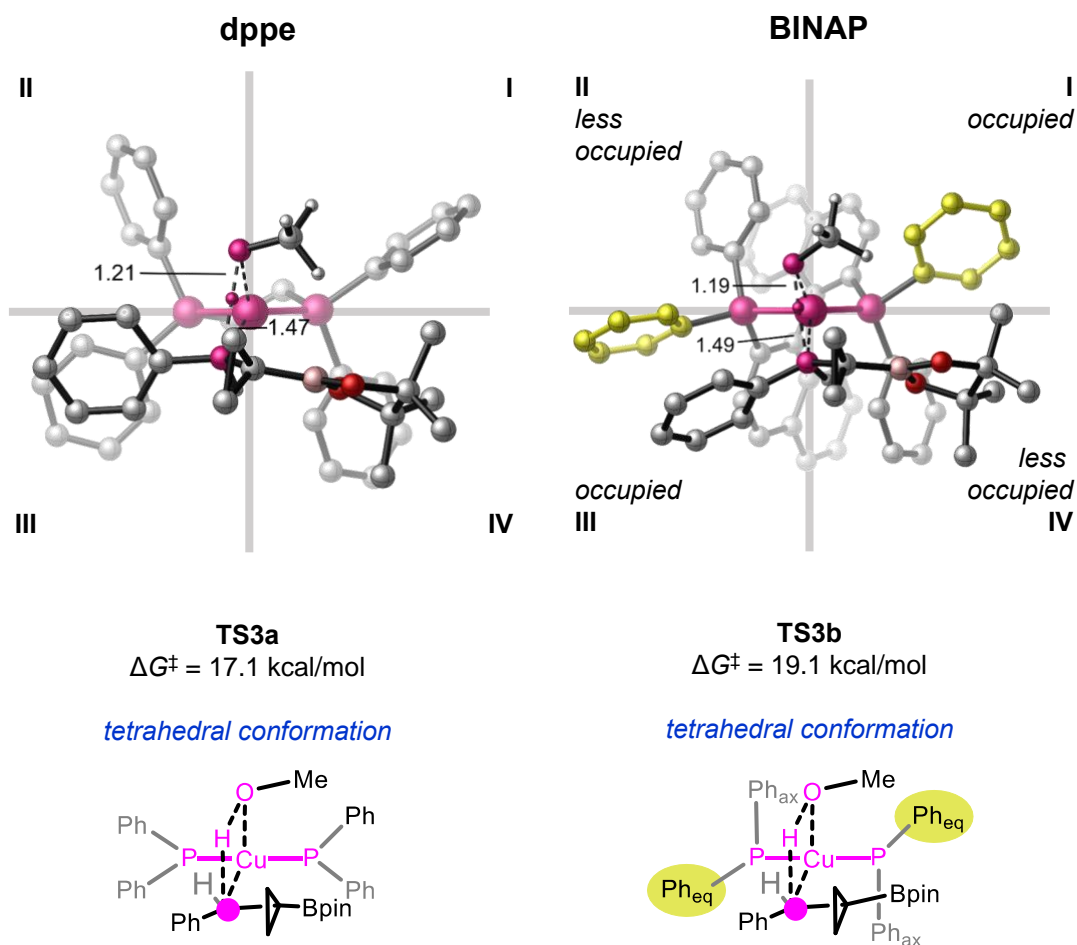
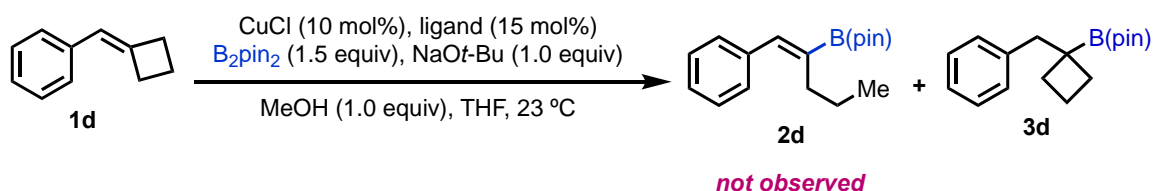


Figure 3.5. Ligand effects on the protodecupration transition states.

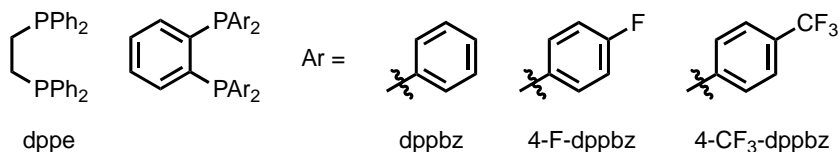
3.4 The Influence of the Ligand–Substrate Interactions on the Product Selectivity and Rates of Cu-Catalyzed Hydroboration of Benzyldenecyclobutanes

Unlike the previously reported hydroboration of benzyldenecyclopropanes,⁵⁹ experiments reveal that benzyldenecyclobutanes do not readily undergo β -carbon elimination that forms the alkenylboronate product **2d** (Table 3.2), despite the similar ring strain energies of cyclopropane and cyclobutane rings (27.5 and 26.3 kcal/mol, respectively). Furthermore, the dppbz ligand gave improved yields, favoring the formation of the boronic ester **3d**, and the installment of electron withdrawing groups installed on the dppbz ligands improved the reaction yields.⁶⁰

Table 3.2. Summary of ligand optimization with representative BCB substrate 1d.

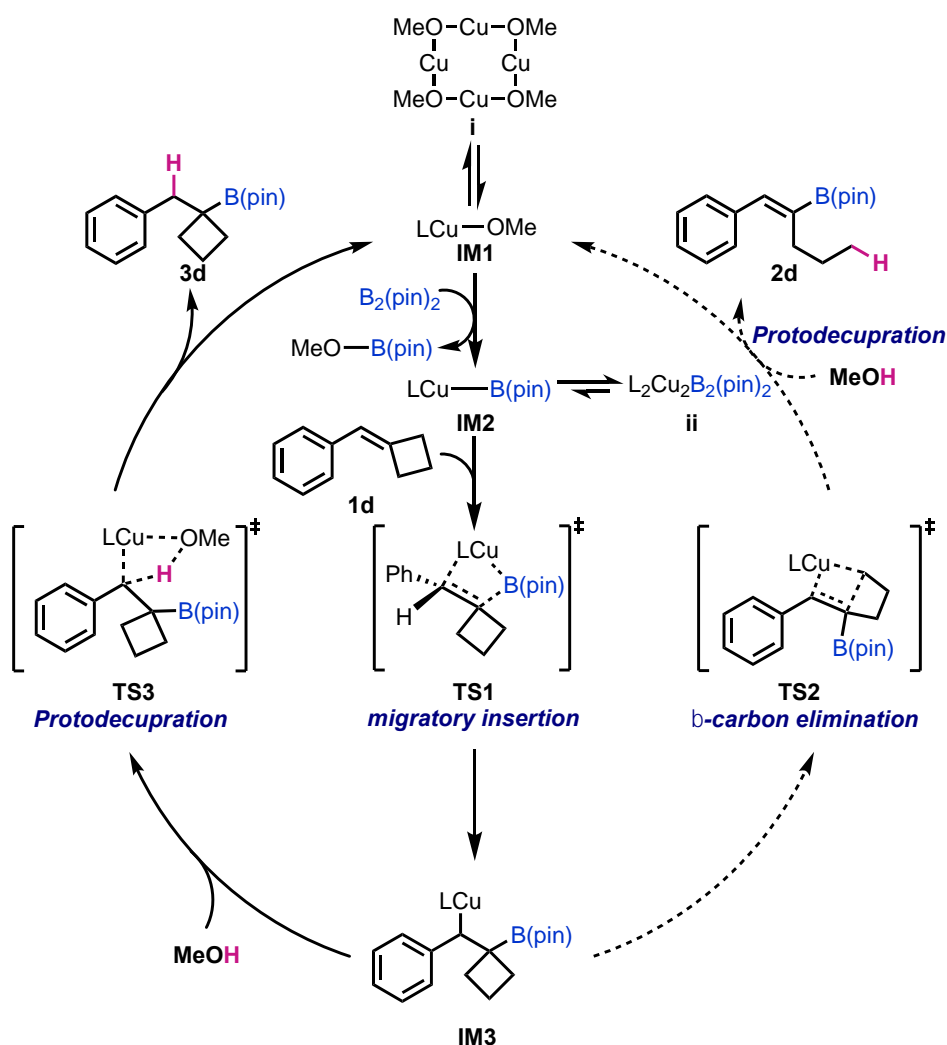


entry	ligand	3d (% yield)
1	dppe	36
2	dppbz	49
3	4-F-dppbz	62
4	4-CF ₃ -dppbz	74



We first investigated the origins of product selectivity in the hydroboration of benzyldenecyclobutanes and computed the reaction energy profiles based on the proposed

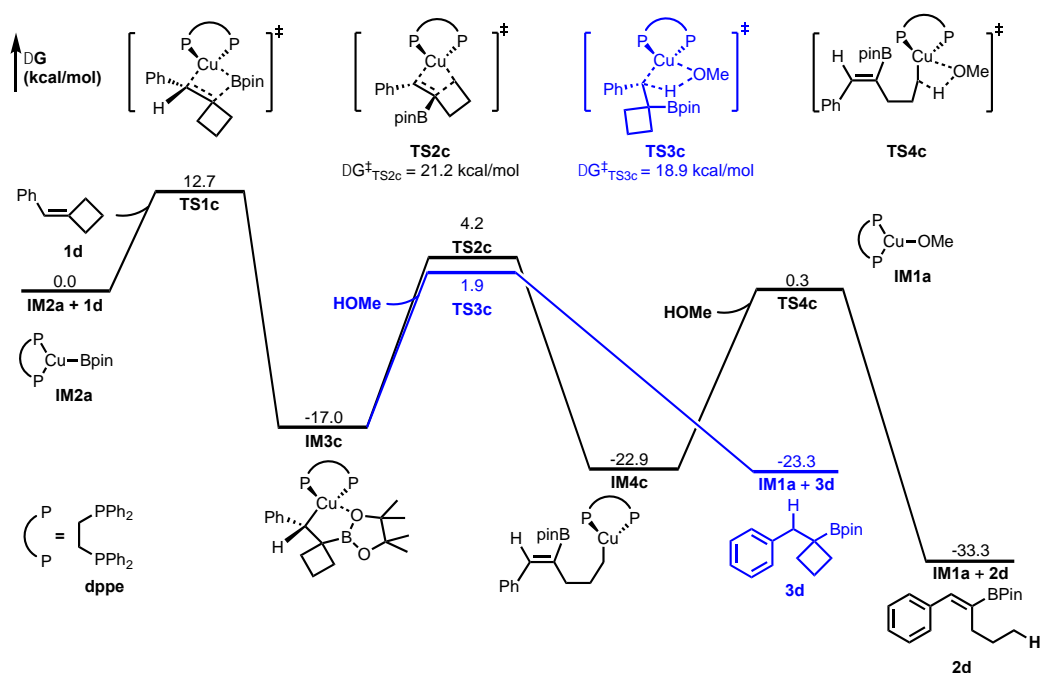
reaction mechanisms shown in **Scheme 3.5**. The productive catalytic cycle involves the σ -bond metathesis of LCu(I)–OMe (**IM1**) with B₂(pin)₂ to form copper(I)–boryl species **IM2**, which undergoes migratory insertion of **1d** via **TS1** to form benzylic Cu(I) intermediate **IM3**. Protodecupration of **IM3** yields the boronic ester **3d** and regenerates the copper(I)–alkoxy complex **IM1**. The benzylic Cu(I) intermediate **IM3** does not form the putative ring-opened alkenylboronate products (**2d**) via **TS2**.



Scheme 3.5. Proposed reaction mechanism of hydroboration of benzylidencyclobutanes.

3.4.1 Comparison of BCB to BCP

To understand why BCBs do not undergo ring-opening despite the similar ring strain energies, we studied the full reaction energy profile with the dppe-supported copper catalyst to compare the benzylidenecyclobutane system to the benzylidenecyclopropane system (**Scheme 3.6**).



Scheme 3.6. Reaction energy profile of the dppe-supported Cu-catalyzed hydroboration of 1d.

Calculations were performed at the M06/6-311+G(d,p)–SDD(Cu) (SMD, THF)/M06L/6-31G(d)–LANL2DZ(Cu) level of theory. Gibbs free energies are calculated at 298 K, 1 mol/L, using Truhlar's quasiharmonic correction.

Energies are reported in kcal/mol.

Our calculations demonstrated that β -carbon elimination in the reaction with BCB is disfavored due to steric effects (**Figure 3.6**). In the β -carbon elimination transition state (TS2c), steric repulsions are observed between the hydrogen of the C_β and the ligand. Additionally, the

B(pin) moiety is slightly rotated towards the ligand Ph, which created steric repulsions between the methyl hydrogen on the B(pin) and the ligand. The ligand–substrate steric repulsions are less in the β -carbon elimination transition state in the reaction with BCP (**TS2a**). The Ph group on the ligand (highlighted) is rotated more towards the C_β in **TS2a**, into the available empty region because the opening of the cyclopropane ring occupies less space than the opening of the cyclobutane ring. This allows the B(pin) to fit into the empty region under the ligand Ph, while avoiding steric clashes between the hydrogens on the C_β and the ligand. In contrast, due to the steric influence of the substrate in **TS2c**, the ligand Ph conformation is rotated towards B(pin) to minimize the repulsions between the hydrogen on the C_β and the Ph group of the ligand, which creates repulsions between B(pin) and the Ph, and induces a slight rotation of the B(pin) group to alleviate some of the steric repulsion. However, this is still not enough and therefore the barrier of the **TS2c** is significantly increased compared to the **TS2a** ($\Delta\Delta G^\ddagger = 7.3$ kcal/mol). On the other hand, the protodecupration barriers are less sensitive to the ring size than the β -carbon elimination barriers. The benzylic carbons in **TS2c** and **TS2a** (highlighted in green) have a tetrahedral-like geometry that places the ring away from the ligand, therefore the protodecupration transition states **TS3c** and **TS3a** are not affected by any steric influence that could have occurred between the substrate and the ligand ($\Delta\Delta G^\ddagger = 1.8$ kcal/mol).

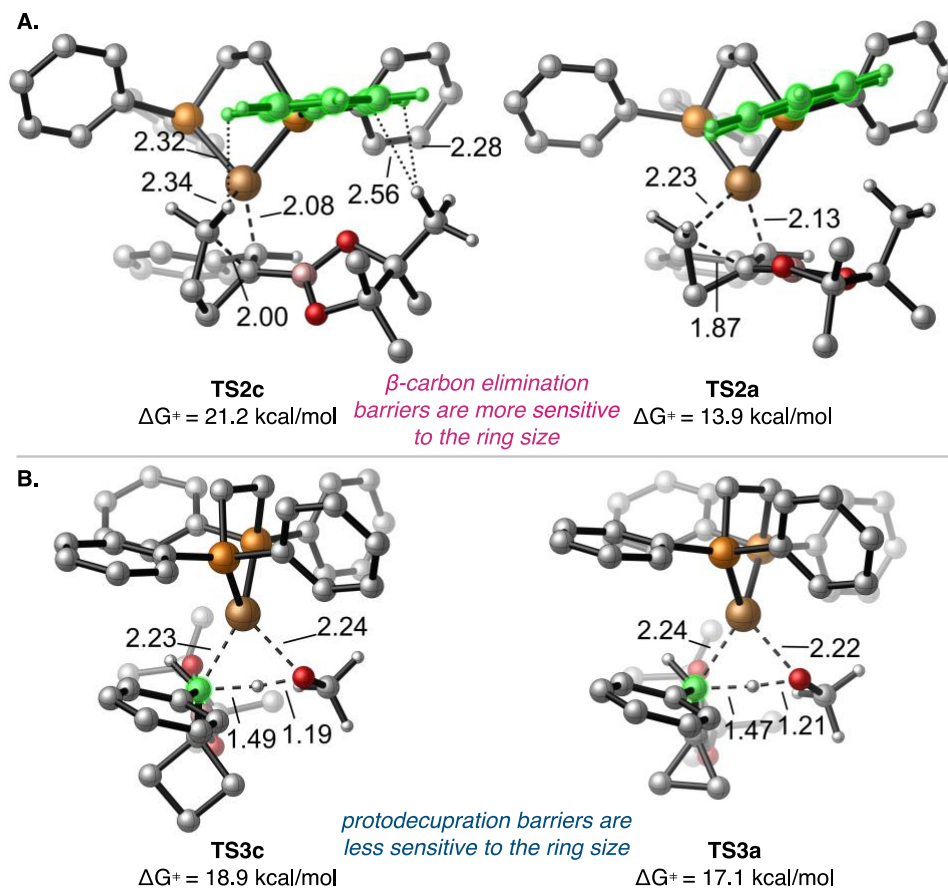
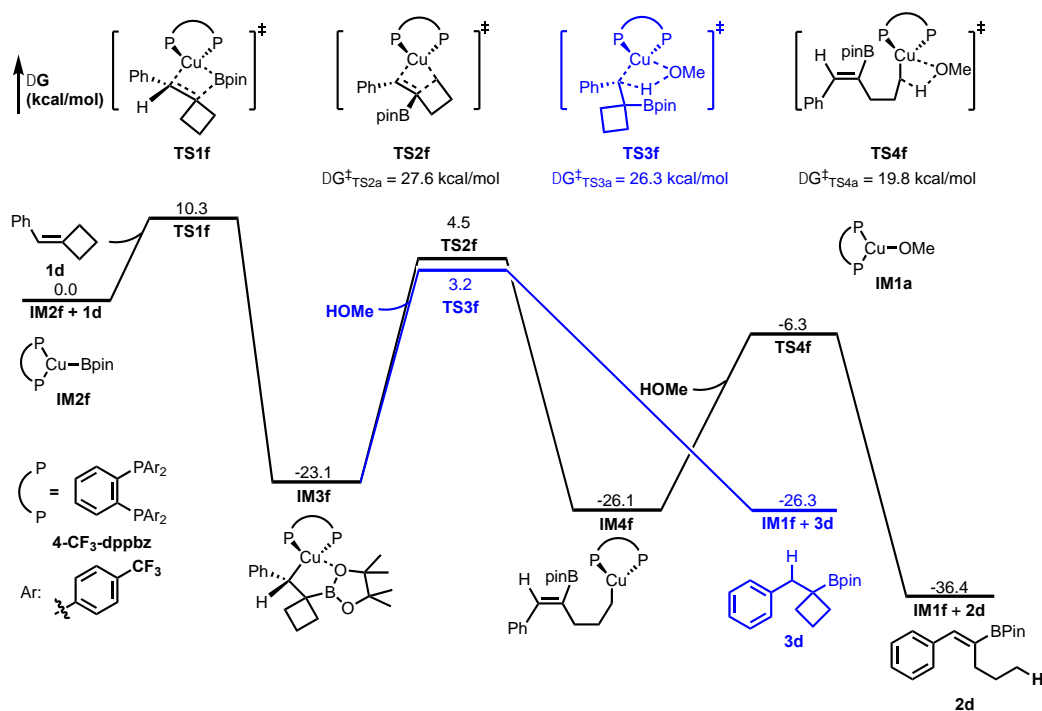


Figure 3.6. Comparison of a) β -carbon elimination and b) protodecupration transition states of BCB and BCPs.

Energies are with respect to the benzylic copper intermediate (**IM3c** and **IM3a**, respectively).

Next, the reaction energy profile of the hydroboration of benzylidenecyclobutane **1d** with the best-performing 4-CF₃-dppbz-supported Cu catalyst suggest was studied (**Scheme 3.7**). The β -carbon elimination (**TS2f**) is disfavored by 1.3 and 11.3 kcal/mol in terms of activation free energy and activation enthalpies, respectively, compared to the competing protodecupration pathway (**TS3f**).



Scheme 3.7. Reaction energy profile of the 4-CF₃-dppbz-supported-Cu-catalyzed hydroboration of 1d.

Calculations were performed at the M06/6-311+G(d,p)–SDD(Cu)(SMD, THF)//M06L/6-31G(d)–LANL2DZ(Cu) level of theory. Gibbs free energies are calculated at 298 K, 1 mol/L, using Truhlar’s quasiharmonic correction.

Energies are reported in kcal/mol.

Although both **TS3f** and **TS2f** adopt a tetrahedral geometry around the copper center, the β -carbon elimination transition state (**TS2f**) is more sensitive to steric effects from the ligand due to a greater substrate binding angle ($\angle\text{CCuO} = 74.4^\circ$ in **TS3f** compared to $\angle\text{CCuC} = 88.2^\circ$ in **TS2f**). Therefore, steric repulsions between the substrate and the ligand destabilize the protodecupration transition state (**Figure 3.7**).

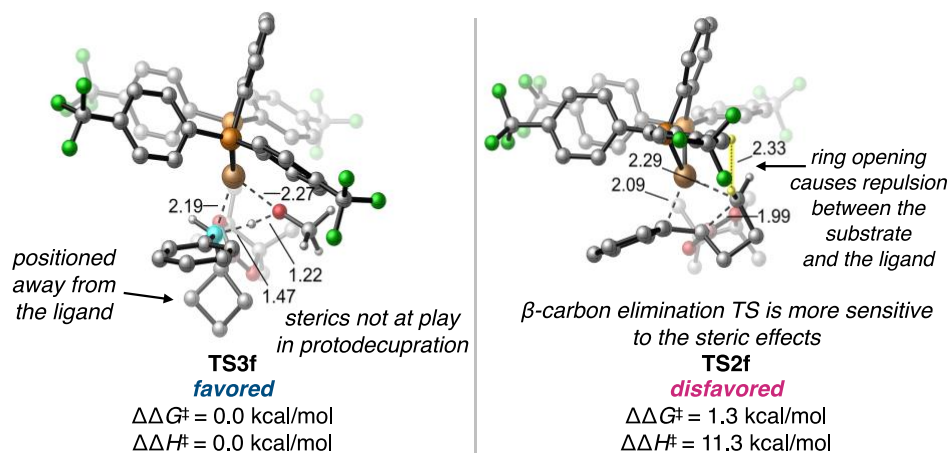
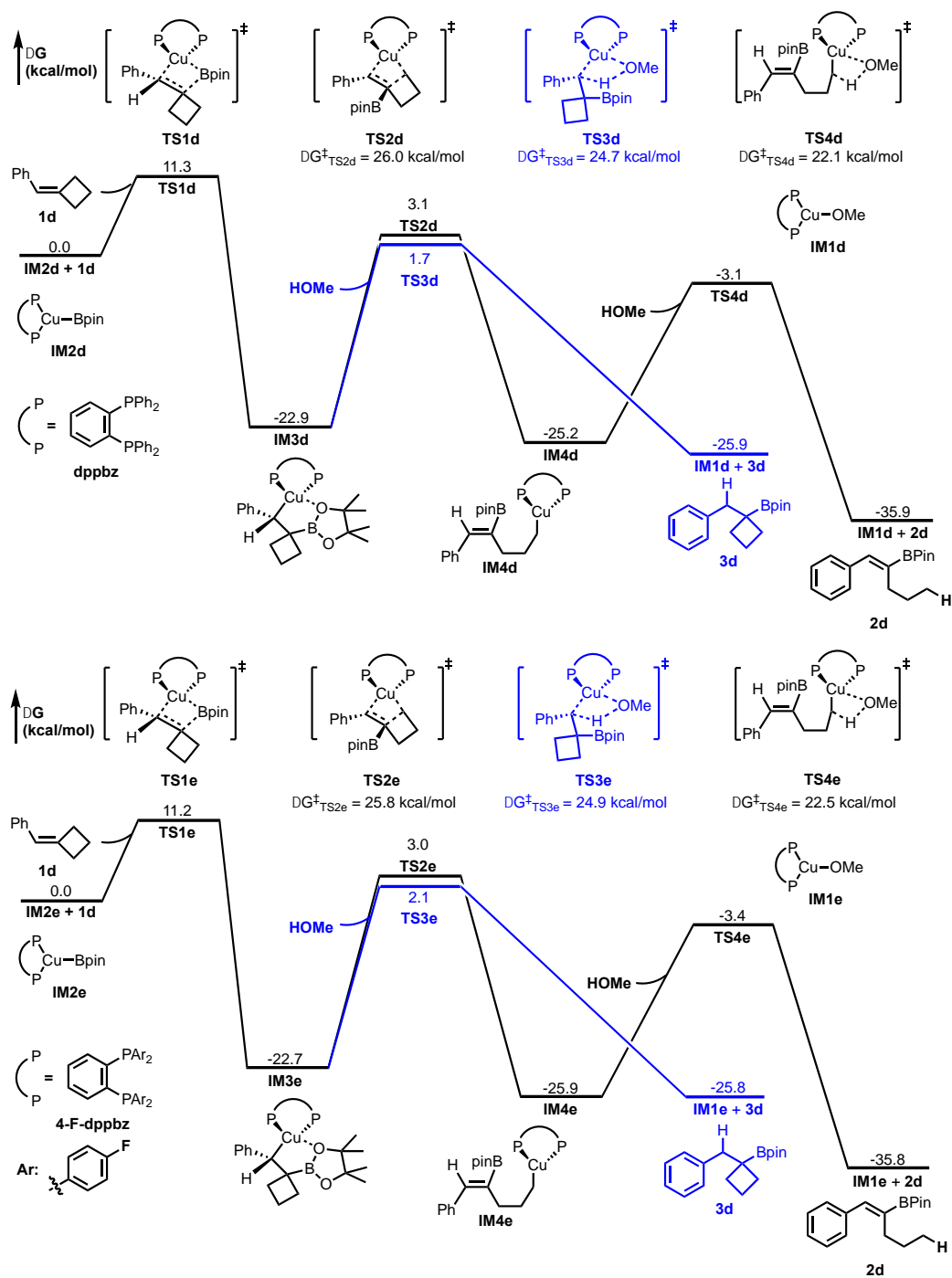


Figure 3.7. Protodecupration (left) and β -carbon elimination (right) transition states with 4-CF₃-dppbz ligand.

Energies are with respect to the benzylic copper intermediate **IM3f**.



Scheme 3.8. Reaction energy profile of the dppbz (top) and 4-F-dppbz (bottom)-supported-Cu-catalyzed hydroboration of 1d.

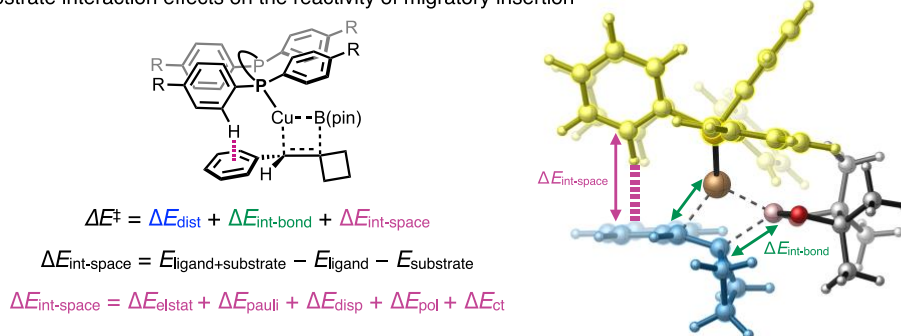
Calculations were performed at the M06/6-311+G(d,p)-SDD(Cu)(SMD, THF)/M06L/6-31G(d)-LANL2DZ(Cu) level of theory. Gibbs free energies are calculated at 298 K, 1 mol/L, using Truhlar's quasiharmonic correction.

Energies are reported in kcal/mol.

3.4.2 Origins of Ligand and Substrate Effects on Reactivity

Next, we turned our attention to the origins of ligand and substrate effects on the barriers to alkene migratory insertion, since the experimental mechanistic studies (*vide infra*) suggested this is the turnover-limiting step of the catalytic cycle. Previous reports and our DFT calculations indicated several stable dimeric and oligomeric copper(I)–alkoxide⁷² or copper(I)–boryl species (*e.g.* i and ii, see **Scheme 3.5**) may be the off-cycle resting state(s) before the migratory insertion step. The computed energies required to convert these off-cycle complexes to the monomeric copper(I)–boryl species (**IM2**) do not correlate with the experimental reactivity, indicating the observed reactivity trend is not a result of dimer or oligomer dissociation. On the other hand, the calculated activation free energies of the migratory insertion transition states with respect to the monomeric copper(I)–boryl species agree well with the experimentally-determined relative reactivities,⁶⁰ indicating the reactivity is mainly affected by the stability of the migratory insertion transition state. To gain more insights into factors that promote the catalyst–substrate interactions in this step, we sought to understand the differences in reactivity via the ligand–substrate interaction model analysis (**Figure 3.8a**).

a) Ligand–substrate interaction effects on the reactivity of migratory insertion



b) Ligand effects on the reactivity of migratory insertion

TS1d
 $\Delta G^\ddagger = 11.3$ kcal/mol

TS1e
 $\Delta G^\ddagger = 11.2$ kcal/mol

TS1f
 $\Delta G^\ddagger = 10.3$ kcal/mol

entry	ligand	ΔE^\ddagger	ΔE_{dist}	$\Delta E_{\text{int-space}}$	$\Delta E_{\text{int-bond}}$	ΔE_{elstat}	ΔE_{pauli}	ΔE_{disp}	ΔE_{pol}	ΔE_{CT}
1	dppbz (TS1d)	-4.7	35.9	-5.2	-35.4	-3.5	17.2	-15.6	-1.0	-2.8
2	4-F-dppbz (TS1e)	-5.2	35.7	-5.5	-35.3	-4.0	17.8	-15.6	-1.0	-3.0
3	4-CF ₃ -dppbz (TS1f)	-5.8	35.5	-6.0	-35.3	-4.3	17.6	-15.7	-1.1	-3.1

c) Substrate effects on the reactivity of migratory insertion

TS1h
 $\Delta G^\ddagger = 13.6$ kcal/mol

TS1e
 $\Delta G^\ddagger = 11.2$ kcal/mol

TS1g
 $\Delta G^\ddagger = 8.1$ kcal/mol

entry	substrate	ΔE^\ddagger	ΔE_{dist}	$\Delta E_{\text{int-space}}$	$\Delta E_{\text{int-bond}}$	ΔE_{elstat}	ΔE_{pauli}	ΔE_{disp}	ΔE_{pol}	ΔE_{CT}
1	R' = OCH ₃ (TS1h)	-4.7	36.1	-6.1	-34.0	-4.2	18.7	-16.4	-1.2	-3.4
2	R' = H (TS1e)	-5.2	35.7	-5.5	-35.3	-4.0	17.8	-15.6	-1.0	-3.0
3	R' = CF ₃ (TS1g)	-5.8	32.9	-6.8	-35.4	-3.4	16.3	-15.9	-1.1	-3.2

Figure 3.8. Summary of the a) ligand–substrate interaction effects on the reactivity of migratory insertion b) ligand effects, and c) substrate effects (L = 4-F-dppbz).

ΔG^\ddagger values are reported with respect to the isolated substrate and the LCu–B(pin) intermediate. The forming B–C bond distances indicate a late transition state with **1e** (**TS1h**), and an early transition state with **1f** (**TS1g**).

The EDA calculations revealed the dominant factors that control the reactivity trends in reactions with different ligands (**Figure 3.8b**) and with different *para*-substituted benzylidenecyclobutanes (**Figure 3.8c**). The higher reactivity with the 4-CF₃-dppbz ligand (entry 4, Table 2.2) compared to those with dppbz and 4-F-dppbz is primarily due to the more favorable electrostatic interactions between the ligand and the substrate (ΔE_{elstat} , **Figure 3.8b**). Examination of the migratory insertion transition state geometries indicated an edge-to-face (T-shaped) interaction between one of the *P*-Ar groups on the ligand and the phenyl group on the substrate (**Figure 3.9**). Therefore, an electron-withdrawing substituent on the “edge” arene (i.e., on the ligand) would enhance the T-shaped π/π interaction through more favorable electrostatic interactions.⁷³

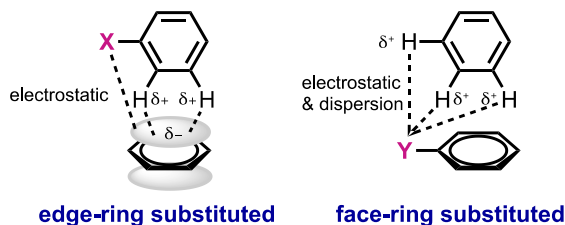


Figure 3.9. Edge-ring and face-ring interactions.

Figure adapted from ref. 73.

On the other hand, when the electron-withdrawing substituent is installed on the “face” arene (i.e., on the benzylidenecyclobutane), the T-shaped π/π interaction becomes weaker, as evidenced by the slightly less favorable ΔE_{elstat} term in the reaction with **1f** ($R' = \text{CF}_3$) than that with **1d** ($R' = \text{H}$) and **1e** ($R' = \text{OCH}_3$) (**Figure 3.8c**). Therefore, although the ligand effects on reactivity are controlled by the T-shaped π/π interaction between the ligand and the substrate, such interactions are not the dominant factor leading to the higher reactivity of electron-deficient benzylidenecyclobutanes (**Figure 3.8c**). The EDA calculations show that the transition state with

1f ($R = CF_3$) is stabilized by multiple factors, including smaller distortion energy (ΔE_{dist}) and Pauli repulsion energy (ΔE_{pauli}), as well as more favorable through-bond interaction energy ($\Delta E_{\text{int-bond}}$) (**Figure 3.8c**). These results indicate that the reaction with **1f** ($R = CF_3$) has an earlier transition state with diminished catalyst/substrate distortion and steric repulsions. Although the transition state is early, the bonding interaction ($\Delta E_{\text{int-bond}}$) between LCu–B(pin) and the electron-deficient benzyldenecyclobutane (**1f**) is still the strongest among the three substrates because of the more electron-deficient π -cloud that promotes migratory insertion.⁶¹

3.5 Conclusions

In summary, computational analysis reveals the mechanisms and the origins of ligand effects on pathway selectivity and reactivity in the Cu-catalyzed hydroboration of BCPs and BCBs. The catalytic cycle begins with the borylation of the copper-alkoxy complex, forming the LCu(I)–B(pin) intermediate. Migratory insertion of the alkene into LCu(I)–B(pin) forms a key benzylic copper intermediate irreversibly. For BCPs, two different products, alkenylboronates (via β -carbon elimination) and boronic esters (via protodecupration), can be formed through two distinct transition states; whereas for BCBs, only the protodecupration product is formed. The turnover-limiting step in the hydroboration of the BCBs is the migratory insertion.

The β -carbon elimination step leading to the alkenylboronate products is sensitive to ligand steric effects. With the dppe-supported Cu-catalyst, β -carbon elimination pathway is favored, forming alkenylboronates. When BINAP-supported Cu-catalyst is used, protodecupration pathway is favored, leading to the formation of cyclopropylboronic esters. The pathway selectivity is determined by the rigidity of the ligand backbone, and the available empty space perpendicular to

the P–Cu–P axis. BCBs do not undergo β -carbon elimination due to the limited spatial availability for the 4-membered ring-opening.

DFT and EDA calculations revealed the role of modified 4-F-dppbz and 4-CF₃-dppbz ligands in enhancing catalytic reactivity on the hydroboration of benzyldenecyclobutanes. The T-shaped π/π interactions between the ligand and the substrate in the migratory insertion transition state influence the reactivity with different modified dppbz ligands. On the other hand, the reactivity differences of substituted benzyldenecyclobutane substrates are mainly affected by the through-bond interactions between the catalyst and the substrates with varying electronic properties. Understanding these types of non-covalent interactions in catalysis offers exciting opportunities in rationally designing ligands that incorporate requisite substrate recognition motifs to amplify reactivity.

4.0 Transient Directing Group Strategies in Pd-Catalyzed Functionalization of Alkenes

Oxtoby, L. J., Li, Z.-Q., Tran, V. T., **Erbay, T. G.**, Deng, R., Liu, P., Engle, K. M. “A Transient-Directing-Group Strategy Enables Enantioselective Reductive Heck Hydroarylation of Alkenes” *Angew. Chem. Int. Ed.* **2020**, 59, 8885–8890.

In this work, I designed and carried out the DFT calculations and analyzed the computational results. Synthesis of compounds and kinetic studies were carried out by Oxtoby, L. J., Li, Z.-Q., Tran, V. T., Deng, R., Engle, K. M. at the Scripps Research Institute.

C(alkenyl)–H Activation Enabled by Transient Directing Group: From Concept to Atropoisomeric Synthesis. *Manuscript in preparation.*

In this work, I designed and carried out the DFT calculations and analyzed the computational results. Synthesis of compounds and kinetic studies were carried out by the Engle Group at the Scripps Research Institute.

4.1 Introduction

Among the foremost challenges in modern synthetic chemistry is forming C–C bonds to establish stereocenters remote from existing functional groups. Catalytic enantioselective alkene functionalization has emerged as an attractive strategy owing to the widespread accessibility and unique reactivity profile of alkenes. The use of directing groups (DGs), functional motifs containing one or more Lewis basic binding sites that are capable of facilitating efficient coordination of a reagent or catalyst, is a classical strategy in organic synthesis for controlling

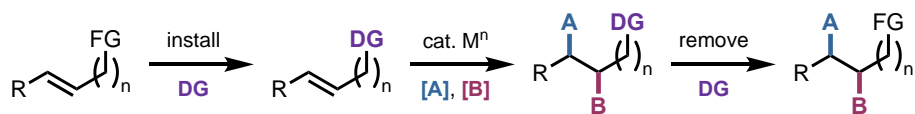
reactivity and selectivity.⁷⁴⁻⁷⁵ In recent years, removable-DG strategies have been successfully applied to various alkene functionalization reactions.⁷⁶⁻⁷⁸ In the realm of difunctionalization and hydrofunctionalization of unactivated aliphatic alkenes, removable bidentate DGs, such as 8-aminoquinoline-derived amides, have proven especially valuable due to their ability to suppress β -hydride elimination and allow subsequent transmetalation/ligand exchange.⁷⁹⁻⁸¹

The reactions involving removable-DGs are valuable, but they are limited by the fact that the DG needs to be installed and cleaved, requiring a minimum of two concession steps (**Figure 4.1a**). Additionally, reactions using DGs are difficult to render enantioselective owing to a lack of available coordination sites on the metal for a chiral ligand.⁸¹⁻⁸⁴ Developing a strategy whereby a chiral directing moiety could condense with the substrate reversibly, promote the desired reaction, and then dissociate effectively, thereby serving as a synergistic organocatalyst,⁸⁵⁻⁸⁶ would directly address the aforementioned issues; however, successfully implementing so-called transient directing groups (TDGs)⁸⁷⁻⁹⁰ in transition metal-catalyzed alkene activation is challenging.

An appropriate TDG must interact in a highly selective yet reversible manner with a native functional group on the substrate, such as an alcohol, aldehyde, or amine. Additionally, this TDG needs to be chemo-orthogonal to the catalytic reaction of interest, such that neither catalytic cycle is inhibited or perturbed to instead form undesired side products. The viability of catalytic TDGs has previously been established in several mechanistically distinct transition metal-catalyzed reactions, including in the field of C–H activation;⁹¹⁻⁹⁸ however there are comparatively few examples⁹⁹ of efficient chiral TDGs in transition metal catalysis, and the scope of these transformations remains limited. Early examples by the groups of Bergman/Ellman¹⁰⁰ and Douglas¹⁰¹ focused on intramolecular alkene cyclizations, but achieved only modest enantioinduction (**Figure 4.1b**, left). Tan and coworkers used the TDG approach for the

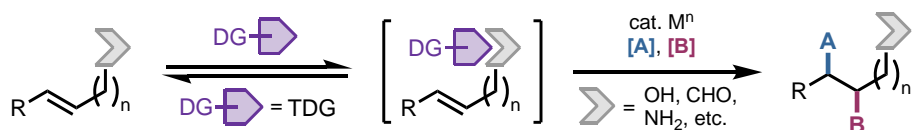
enantioselective hydroformylation of allylic amines using phosphinite ligands (**Figure 4.1b**, middle).¹⁰² More recently, Yu and coworkers have successfully developed amino acid TDGs to promote enantioselective benzylic C–H activation with Pd(II) (**Figure 4.1b**, right).¹⁰³⁻¹⁰⁴

a. Transient DG and removable DG strategy for alkene functionalization



removable DG limitations

- requires additional synthetic transformations
- often requires purification of intermediates
- process generates unnecessary waste
- cleavage conditions can be harsh



transient DG challenges

- must be compatible with catalytic system
- must not promote undesired pathways
- must effectively coordinate metal center
- DG installation/removal must be reversible

b. Key precedents in use of chiral TDGs in catalysis

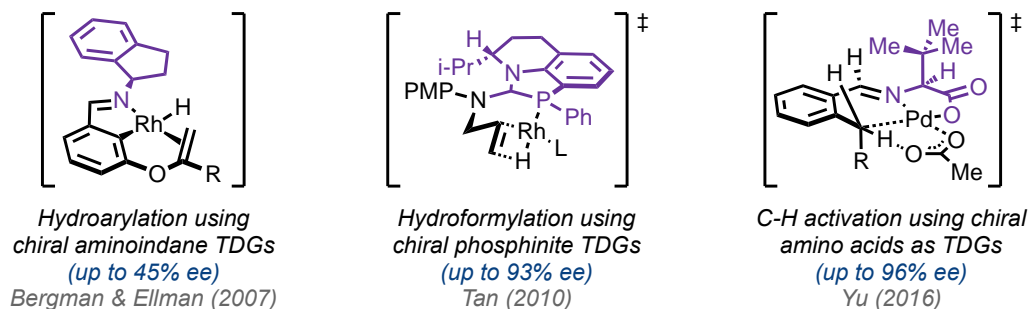


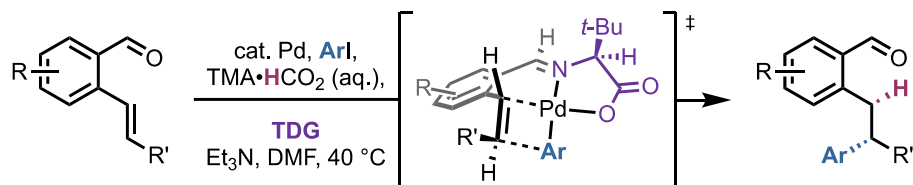
Figure 4.1. General comparison of auxiliary-based and TDG approaches for alkene functionalization. b)

Pioneering examples of using chiral TDGs in transition metal catalysis.

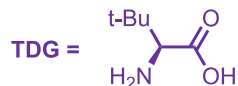
Recent collaborations between our group and Engle Group explored the Pd-catalyzed C(alkenyl)–H activations for carboamination of unactivated alkenes⁹⁹ and the site selectivity in the synthesis of 1,3-dienes, with the aminoquinoline directing group.¹⁰⁵ Although Yu and Houk groups have explored the use of TDG in the aryl and alkyl C–H bond functionalization,¹⁰⁶ the TDG-

assisted functionalization of alkenyl C–H bonds are scarce. Likewise, despite the enantioselective Heck-type hydroarylations are known and well-studied, the TDG effects on the reaction mechanisms and the mode of enantioinduction are unknown and have not been explored computationally. There are several general mechanistic questions in TDG-mediated transition metal catalysis. For example, using TDGs may alter the reaction pathway and change the rate- and stereoselectivity-determining steps. Another question is the understanding of the origin of enantioinduction, in particular, the roles of potential highly strained metallacycle intermediates during the catalytic process that involve multi-dentate chelation of the TDG and the substrate to the metal center—these strain and distortion effects may destabilize reaction intermediates and impede rates of key elementary steps, but alternatively, they may be leveraged to control stereoselectivity induced by the chiral TDG. However, the influence of the remote chiral center in the stereoinduction is often unclear. In this chapter, using DFT methods, we are exploring two TDG-promoted alkene functionalization reactions; (i) an enantioselective Heck hydroarylation (**Figure 4.2a**), and (ii) a Pd-catalyzed alkenyl C–H activation for the atroposelective synthesis of 1,3-dienes (**Figure 4.2b**), both facilitated by *L-tert*-leucine as the chiral TDG. We aim to understand the reaction mechanisms, rate- and selectivity-determining steps, and modes of enantioinduction and atroposelectivity that are difficult to investigate experimentally.

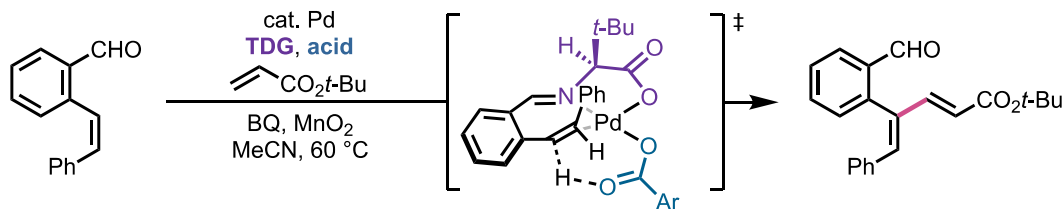
a. Asymmetric reductive Heck hydroarylation using a TDG



- What is the mechanism of the hydroarylation?
- What is the origin of the high enantioselectivity?



b. C(alkenyl)–H Activation Enabled by TDG



- What is the mechanism of the C–H activation?
- What is the origin of the high atroposelectivity?

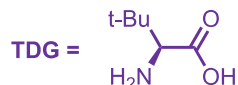


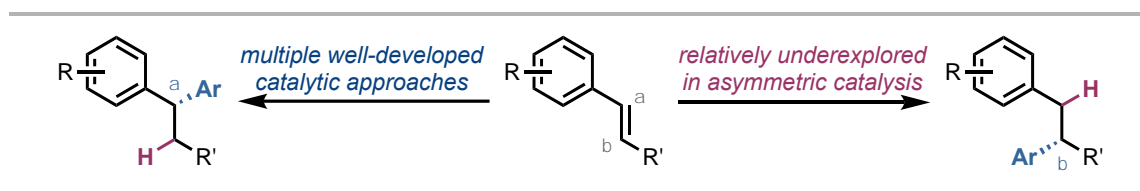
Figure 4.2. a) General depiction of a reductive Heck reaction facilitated by an in situ formed imine using a chiral TDG strategy. b) Catalytic C(alkenyl)–H activation enabled by TDG.

4.2 A Transient-Directing-Group Strategy that Enables Enantioselective Reductive Heck Hydroarylation of Alkenes

Palladium-catalyzed Heck-type arylations¹⁰⁷⁻¹⁰⁸ provide a powerful mode of reactivity as a result of their broad substrate scope and functional-group compatibility. However, significant limitations in Heck-type chemistry remain, including controlling regioselectivity with multi-substituted, electronically neutral alkenes; suppressing β -hydride elimination to enable interception with additional reaction partners; and achieving stereinduction during intermolecular

migratory insertion.¹⁰⁹⁻¹¹¹ The application of chiral TDG strategies in versatile Pd(0)-catalyzed Heck-type coupling remains unknown.

Our collaborators, the Engle Group, demonstrated that the use of a chiral amine TDG could facilitate a stereo-controlled Heck-type migratory insertion with an alkenyl aldehyde substrate, where the reductive Heck system¹¹²⁻¹¹³ would tolerate the presence of the free amine and water, operate synergistically with the TDG cycle, while the mild conditions typical of these reactions could curb undesired side reactions. After the migratory insertion, the TDG would suppress β -hydride elimination to enable interception with a hydride source. Successful implementation of this strategy would complement the various methods that have been developed for achieving enantio- and α -selective hydroarylation of styrenes.¹¹⁴⁻¹¹⁷ Comparatively few methods have been reported for hydroarylation of internal alkenylarenes to install a C(sp³)-Ar chiral center at the β -position (**Scheme 4.1**);¹¹⁸⁻¹²¹ and common alternative methods such as cross-coupling of homobenzylic alkyl halides or trifluoroborates often deliver low yields or enantioselectivity.¹²²⁻¹²³



Scheme 4.1. State of the art in the asymmetric hydroarylation of styrenes.

(*Z*)-2-(prop-1-en-1-yl)benzaldehyde was initially screened as a model substrate based on the fact that alkyl-substituted internal styrenes are typically challenging substrates with low reactivity in intermolecular Pd-catalyzed reductive Heck coupling.¹¹³ The screening of a variety of conditions and amino acids revealed that *L*-*tert*-leucine gave both high yields and

enantioselectivity, illustrating the privileged nature of amino acids in organocatalytic processes (**Figure 4.3**).

The X-ray crystallography studies confirmed the stereochemistry of the product of the reaction of **3** with *N*-aminophthalimide is in (*S*)-configuration (**Figure 4.3**). Deuterium labeling studies demonstrated that the formate serves as a hydride source following decarboxylation. A control experiment without the amino acid additive resulted in no reaction, thus demonstrating the critical role of this co-catalyst for reactivity as well as selectivity. To rule out an alternate pathway involving classical Mizoroki–Heck arylation followed by reduction of the intermediate diarylalkene, a representative stilbene substrate (**1c**) was subjected to standard conditions with the exclusion of aryl iodide, and in this case the starting material was recovered.

In the light of these results, we sought to understand the reaction mechanisms, and the origins of the excellent regio- and enantioselectivity in this system using DFT calculations.¹²⁴

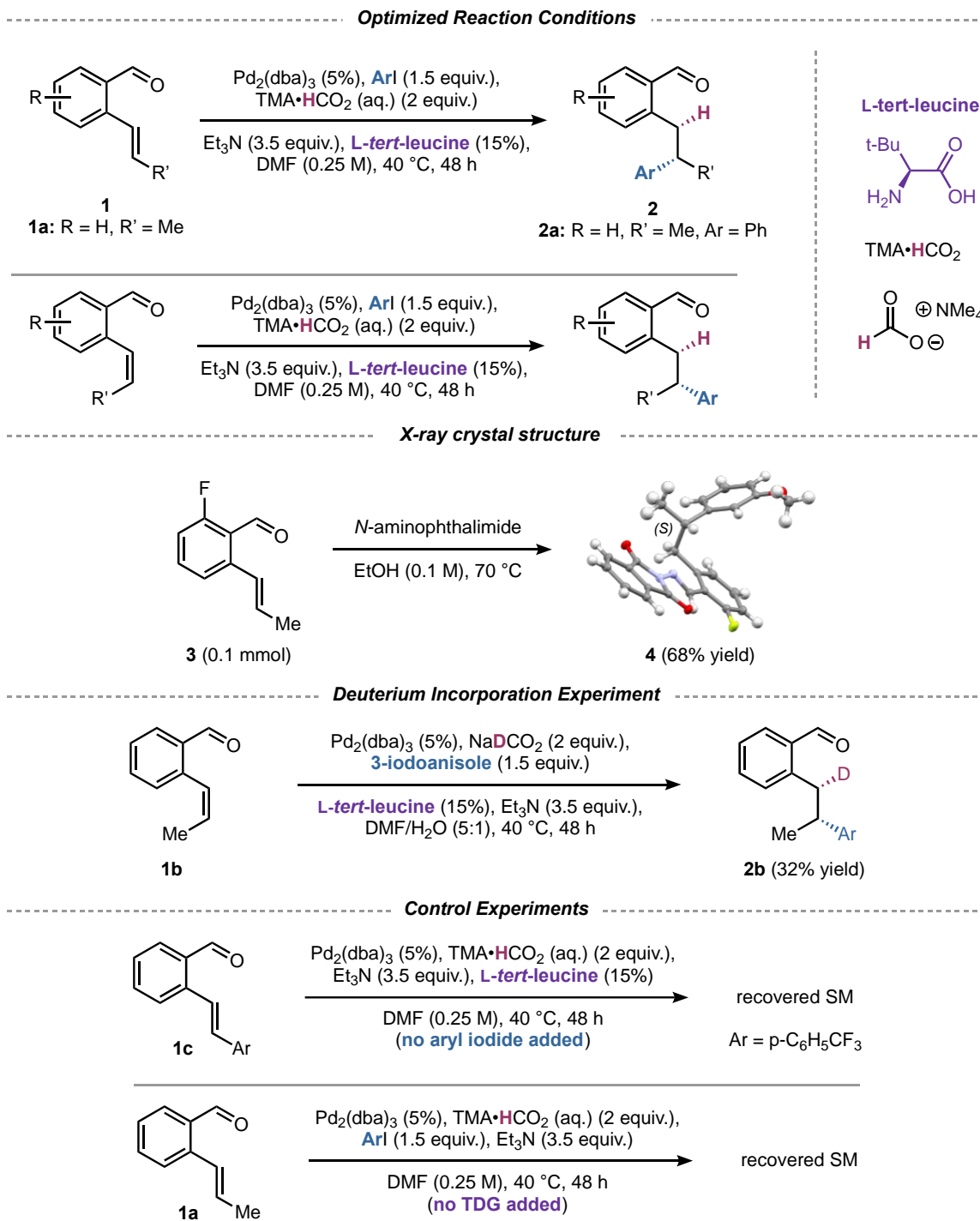


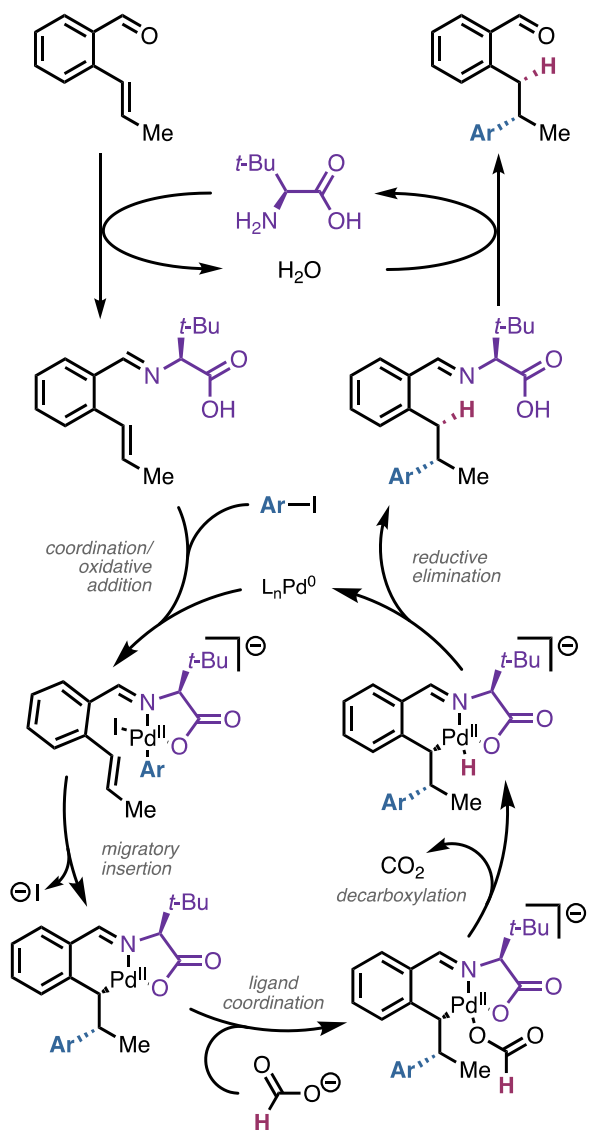
Figure 4.3. Optimized reaction conditions, X-ray crystal structure, deuterium incorporation and control experiments.

4.2.1 Computational Methods

Geometry optimizations and single point energy calculations were carried out using Gaussian 16.³⁰ Geometries of intermediates and transition states were optimized using the M06 functional³¹ with a mixed basis set of SDD for Pd and 6-31G(d) for other atoms in the gas phase. Vibrational frequency calculations were performed for all the stationary points to confirm if each optimized structure is a local minimum or a transition state structure. Solvation energy corrections were calculated in DMF solvent with the SMD solvation model³⁶ based on the gas-phase optimized geometries. The M06 functional with a mixed basis set of SDD for Pd and 6-311+G(d,p) for other atoms was used for single point energy calculations. Gibbs free energies were calculated at the standard conditions (298K, 1 atm) using Cramer and Truhlar's quasiharmonic approximation³⁴ using Goodvibes v2.0.1.³⁵ Images of structures were generated using CYLview.³⁹

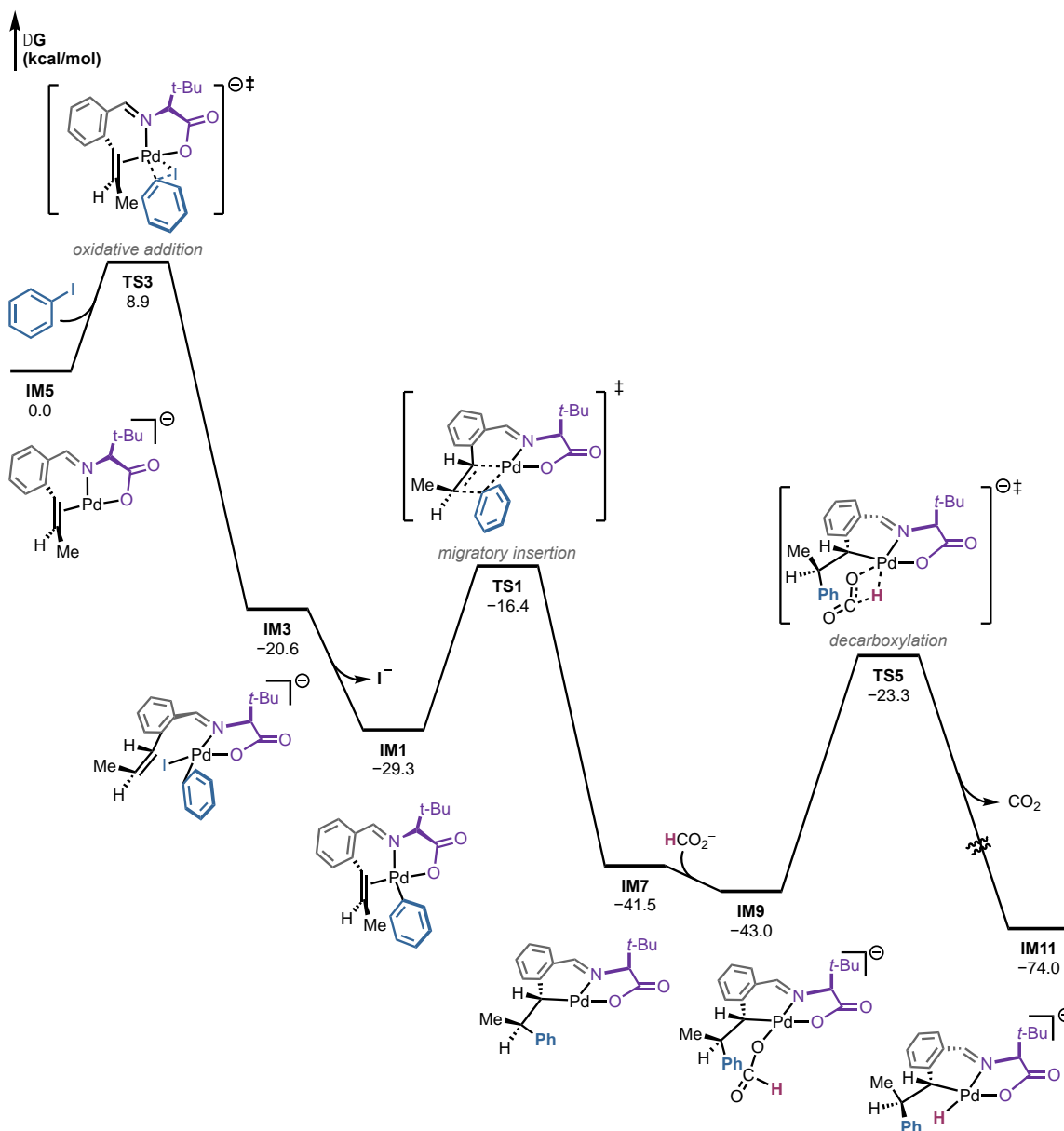
4.2.2 Mechanism of C–H Activation

The proposed catalytic cycle is outlined in **Scheme 4.2**. Following coordination with the condensed imine and the oxidative addition of the aryl iodide, the arylpalladium(II) intermediate undergoes an irreversible migratory insertion. Next, the alkylpalladium(II) intermediate is intercepted with formate, which decarboxylates to generate a Pd–H species. Following C–H reductive elimination, Pd(0) is regenerated to close the catalytic cycle, and dissociation of the TDG affords the desired product.



Scheme 4.2. Proposed catalytic cycle.

We calculated the reaction energy profiles of the hydroarylation of the (*E*)-alkene **1a** with iodobenzene to identify the enantioselectivity-determining step, to elucidate the factors affecting the π -facial selectivity in the migratory insertion, and to investigate the mechanism of the decarboxylation. Pathway leading to the experimentally observed (*S*)-product is shown in **Scheme 4.3**. The corresponding oxidative addition pathway in which the Pd binds to the other face of the alkene and leading to the (*R*)-product was also calculated (**Scheme 4.4**).



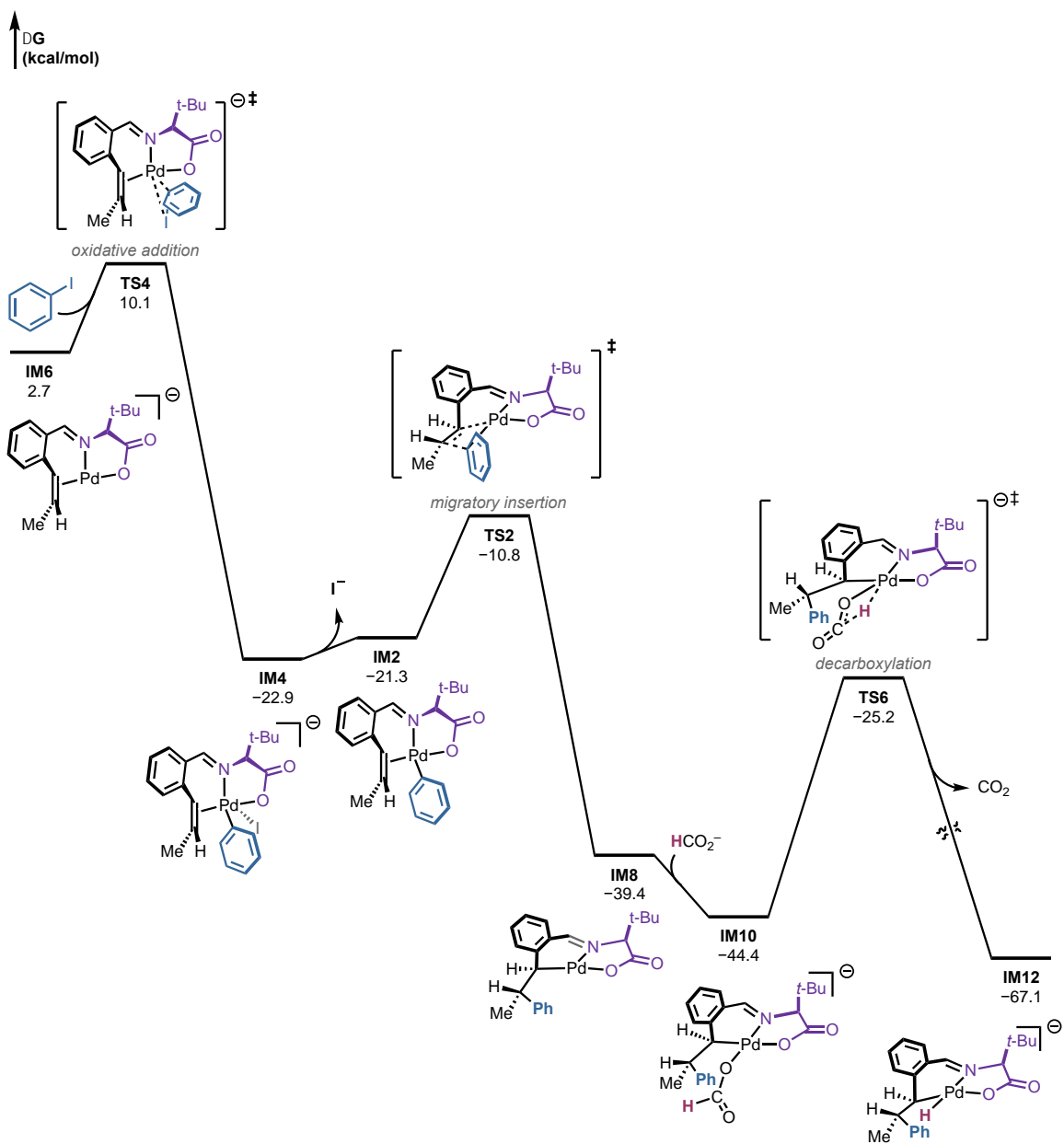
Scheme 4.3. Calculated reaction energy profile of hydroarylation of alkene 1a to form the (S)-enantiomer of the product.

Energies are reported with respect to **IM5**.

Upon coordination with the condensed imine, π -alkene Pd(0) complex **IM5** undergoes facile oxidative addition with iodobenzene via **TS3** to form Pd(II) intermediate **IM3**, which then dissociates an iodide anion to form four-coordinated π -alkene arylpalladium(II) complex **IM1**

(**Scheme 4.3**). The π -alkene Pd(0) complex **IM6**, which is 2.7 kcal/mol less stable than **IM5**, also undergoes facile oxidative addition with iodobenzene (**TS4**) and iodide dissociation to form four-coordinated π -alkene Pd(II) complex **IM2** (**Scheme 4.4**). Both oxidative addition transition states (**TS3** and **TS4**) require low activation energies and are highly exergonic.

The four-coordinate π -alkene Pd(II) complex **IM1** that forms the favored (*S*)-product is 8.0 kcal/mol more stable than the corresponding **IM2** that forms the other enantiomer. Although the initial oxidative addition is irreversible and preferentially forms **IM1**, the two π -alkene complexes **IM1** and **IM2** may equilibrate via partial dissociation of the π -alkene. Therefore, under these Curtin-Hammett conditions, the enantioselectivity of the hydroarylation product is determined in subsequent steps after the oxidative addition. The migratory insertion from **IM1** and **IM2** forms the 3-coordinated alkylpalladium(II) intermediates **IM7** and **IM8**, respectively, which upon coordination of formate anion form more stable four-coordinated Pd(II) intermediates **IM9** and **IM10**. The subsequent decarboxylation occurs via **TS5** and **TS6**. Because **TS5** and **TS6** are lower in energy than migratory insertion transition states **TS1** and **TS2**, the migratory insertion is irreversible and thus enantioselectivity-determining. **TS5** and **TS6** are four-membered cyclic transition states, leading to palladium hydride complexes **IM11** and **IM12**. C–H reductive elimination from **IM11** and **IM12** would form the favored (*S*)-product and disfavored (*R*)-product, respectively. The C–H reductive elimination from Pd(II) is expected to be facile and thus was not calculated.



Scheme 4.4. Calculated reaction energy profile of hydroarylation of alkene 1a to form the (*R*)-enantiomer of the product.

Energies are reported with respect to **IM5**.

The oxidative addition (**TS3** and **TS4**) and decarboxylation (**TS5** and **TS6**) transition states are shown in **Figure 4.4** and **Figure 4.5**, respectively. In these transition states, the benzene ring on the alkene substrate is puckered below the plane and the *t*-Bu group on the *L*-*tert*-leucine

directing group is above the plane. This conformation minimizes the distortion around the planar imine nitrogen and the five-membered ring with the *N,O*-bidentate directing group.

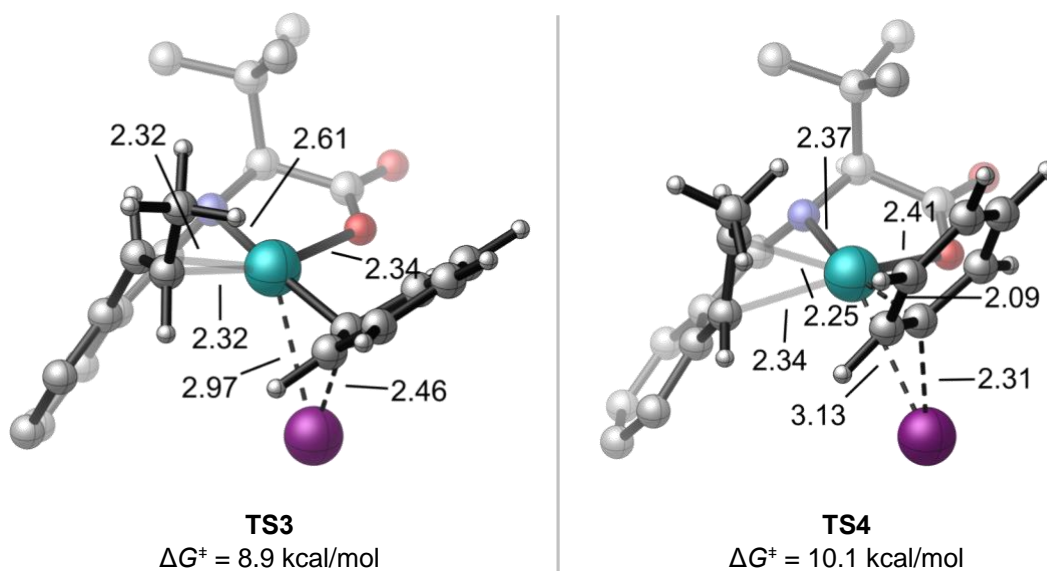


Figure 4.4. Oxidative addition transition states.

Energies are with respect to the Pd(0) π -alkene complex **IM5**.

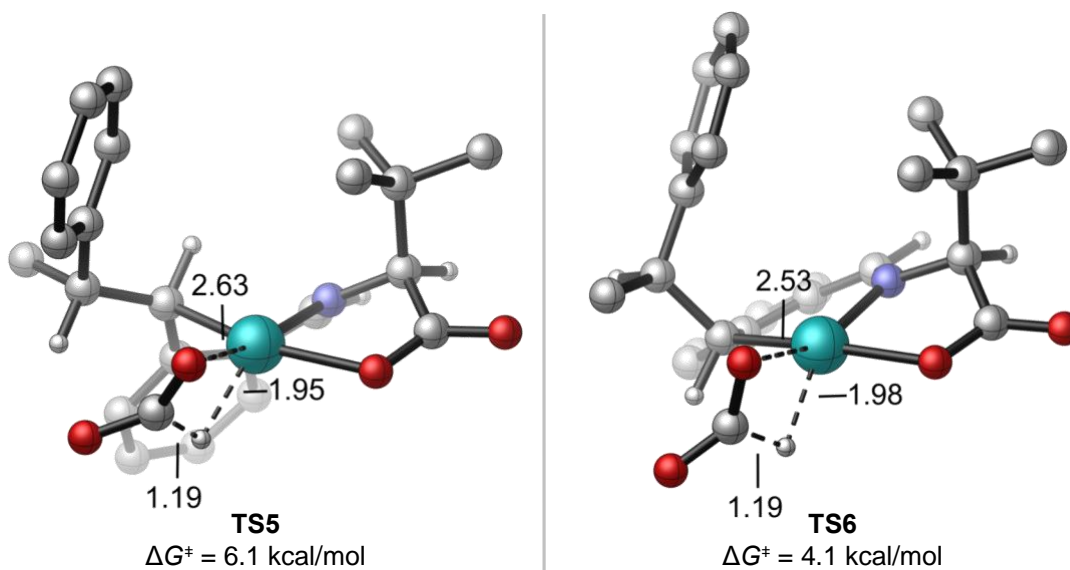


Figure 4.5. Decarboxylation transition states.

Energies are with respect to the Pd(0) π -alkene complex **IM1**.

4.2.3 Origin of Enantioselectivity

The computed energy profiles showed that the alkene migratory insertion is irreversible and enantioselectivity-determining because the subsequent decarboxylation transition states are lower in energy than the migratory insertion transition states. The π -alkene complex (**IM1**) and the migratory-insertion transition state (**TS1**) leading to the (*S*)-enantiomer of the product are both significantly more stable than corresponding structures in the pathway that forms the (*R*)-enantiomer (**IM2** and **TS2**, respectively, **Figure 4.6**).

The origin of this energy difference is not direct steric repulsion between the *t*-Bu moiety of the directing group and either of the two newly formed stereocenters.¹²⁵ Instead, it is attributed to the conformation of the fused benzene ring. In both **IM1** and **TS1**, the benzene ring fused to the 6-membered palladacycle is puckered below the plane of the square planar Pd, while the *t*-Bu moiety of the directing group is puckered above the plane. This geometry allows the imine nitrogen to remain in the preferred planar geometry and the Pd center to be perfectly square planar.

By contrast, in **IM2** and **TS2**, the benzene ring and the *t*-Bu moiety are both puckered above the plane. This induces significant distortion around the sp²-hybridized imine nitrogen and distorts the Pd from the preferred square planar geometry. Although the chiral center on the TDG is remote from the alkene, the distortion effect leads to a 5.6 kcal/mol energy difference between **TS1** and **TS2**. Thus, the formation of the (*S*)-configured product is predicted to be strongly favored, which is consistent with the absolute configuration determined by the X-ray crystallography as demonstrated in **Figure 4.3**.

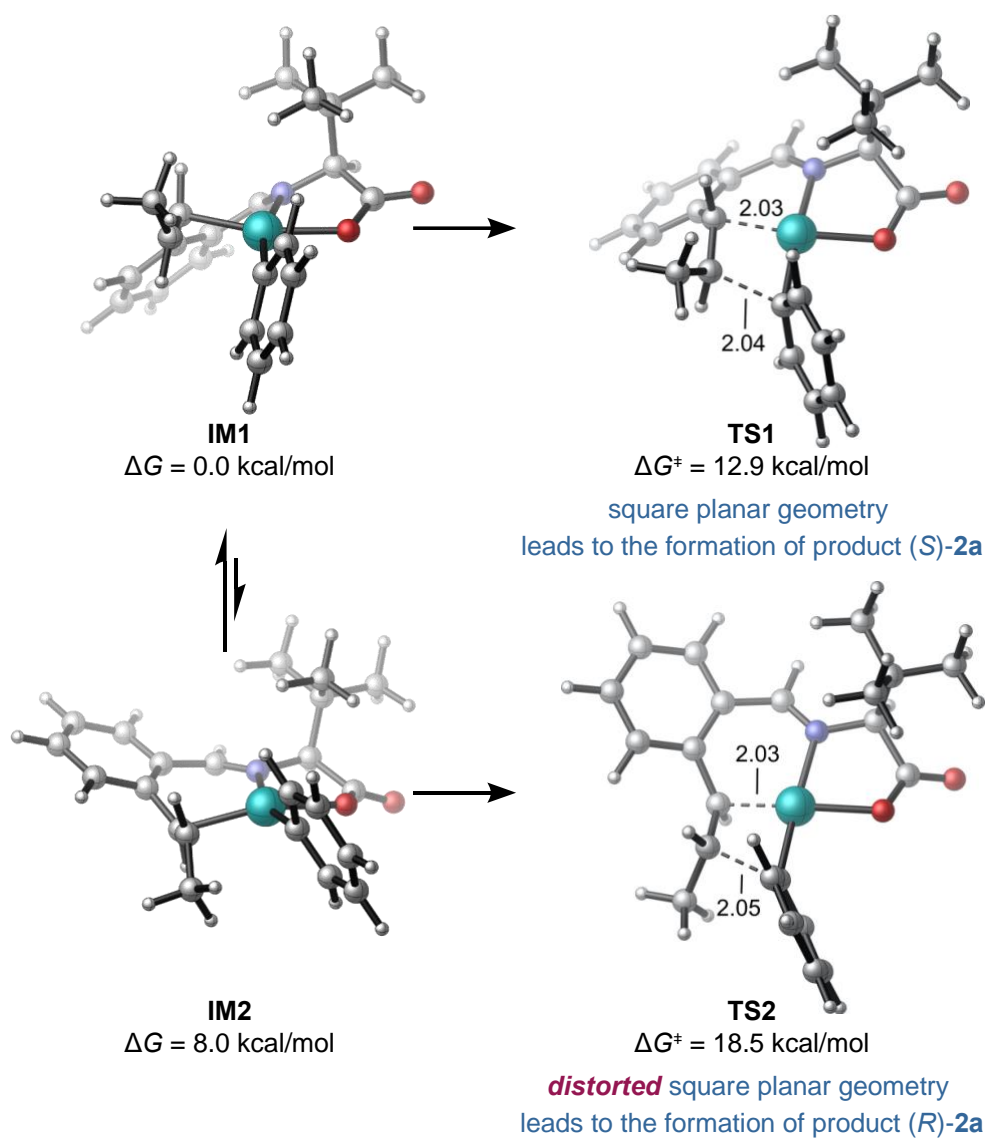


Figure 4.6. Origin of enantioselectivity in migratory insertion.

Energies are with respect to the Pd(II) π -alkene complex **IM1**.

4.2.4 Conclusions

In summary, a Pd-catalyzed asymmetric reductive Heck hydroarylation of alkenes remote to aldehyde functional groups, enabled by the transient *L-tert*-leucine directing group, is developed. The reaction proceeds under mild conditions, is tolerant to various functional groups, and provides the desired products in high *ee*.

DFT calculations were carried out to elucidate the reaction mechanisms and the origins of enantioinduction by the chiral TDG. The reaction proceeds by in situ formation of the imine, which is followed by the coordination of the alkene to the metal. This is followed by the oxidative addition of the aryl iodide. The forming intermediate undergoes an irreversible migratory insertion. Next, the formate intercepts the stabilized alkylpalladium(II) intermediate, and decarboxylates to generate a Pd–H species. Following the C–H reductive elimination, Pd(0) is regenerated, and dissociation of the directing group furnishes the desired product.

Our DFT calculations demonstrated that the oxidative addition requires low activation barriers. The irreversible alkene migratory insertion is the enantioselectivity-determining step in the reaction, and an unusual mode of enantioinduction by the remote chiral center in the transient directing group is observed, where the π -facial selectivity is induced by the conformation of the fused benzene ring.

4.3 C(alkenyl)–H Activation via Transient-Directing-Group Strategy for Atropoisomeric Synthesis

Oxidative coupling of C(alkenyl)–H bonds with alkenes is an efficient strategy to access 1,3-dienes. Compared to C(alkyl)–H and C(aryl)–H activation, C(alkenyl)–H activation with transient directing groups is rare. Previous studies of our group in collaboration with the Engle Group explored the mechanism and the origin of site selectivity of a Pd-catalyzed alkenyl C–H functionalization for the 1,3-diene synthesis with the 8-aminoquinoline directing group, where the C–H activation takes place through the formation of a six-membered palladacycle.¹⁰⁵ Inspired by this preparation of 1,3-dienes together with the hydroarylation¹²⁴ and arylfluorination¹²⁶ of the *ortho*-alkenylbenzaldehydes that have been achieved with the TDG strategies, a TDG-promoted Pd-catalyzed C(alkenyl)–H functionalization is achieved (**Figure 4.7a**). Optimization of the reaction conditions revealed that the fluorine-containing benzoic acids are effective in promoting the C–H activation, and the TDGs with an α -substituent group are more effective, and *L*-*tert*-leucine performed the best. The atroposelective synthesis of axially chiral styrene derivatives was achieved in the reaction of *ortho*-disubstituted styrene **4** with the *L*-*tert*-leucine as the TDG. The reaction was carried out at room temperature for four days, affording 1,3-diene product **5** with excellent atroposelectivity (**Figure 4.7b**). The TDG-promoted C–H activation step was verified by the preparation of the palladacycle complex via stoichiometric reaction of the amino acid and Pd(OAc)₂ pre-catalyst with substrate **1** in the presence of pyridine as an L-type ligand to stabilize the complex.

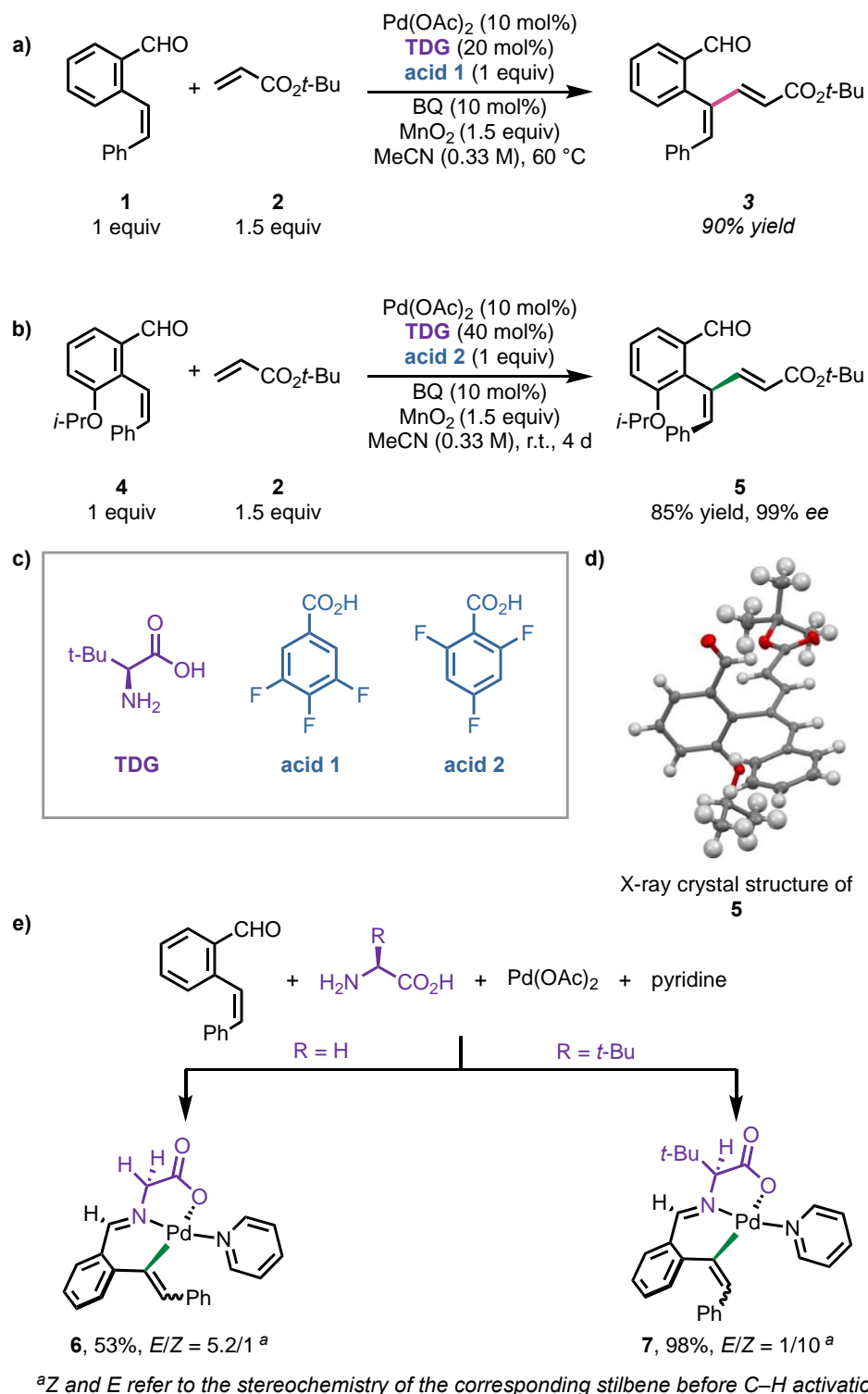


Figure 4.7. a) Optimized reaction conditions, b) Synthesis of atropisomeric 1,3-diene 5, c) TDG and the acids used in reactions, and d) X-ray crystal structure of 5, e) Stoichiometric reaction to form the palladacycle complex.

We performed DFT calculations to probe the reaction energy profiles using the (Z)-alkene **1** as the model substrate, to understand the mechanism of C–H activation and the origins of the observed atroposelectivity.

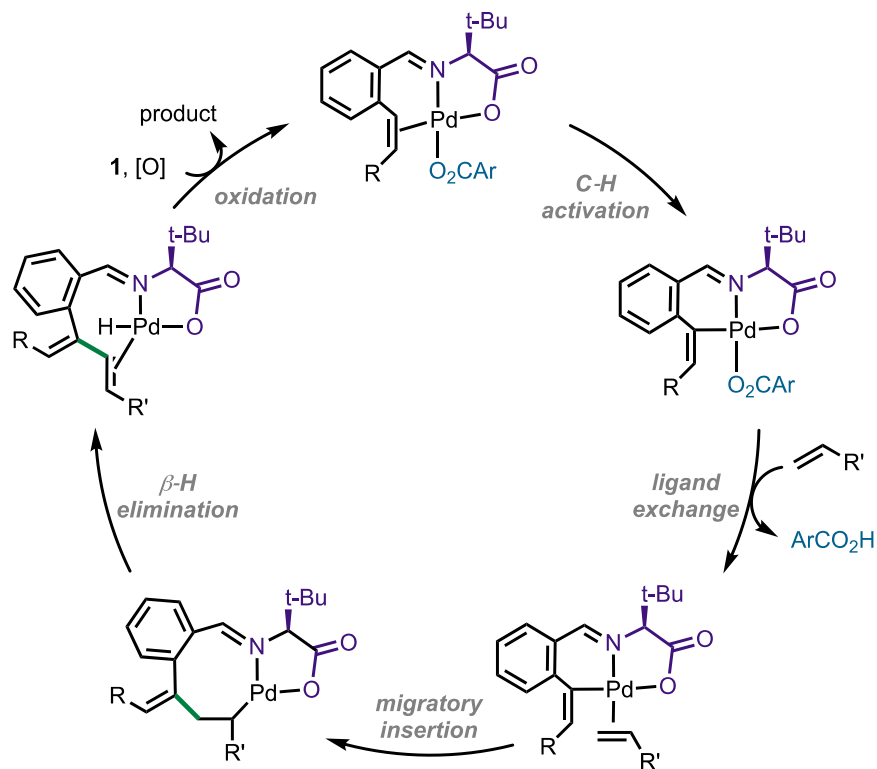
4.3.1 Computational Methods

Geometry optimizations and single point energy calculations were carried out using Gaussian 16.³⁰ Geometries of intermediates and transition states were optimized using the M06 functional³¹ with a mixed basis set of SDD for Pd and 6-31G(d) for other atoms in the gas phase. Vibrational frequency calculations were performed for all the stationary points to confirm if each optimized structure is a local minimum or a transition state structure. Solvation energy corrections were calculated in acetonitrile solvent with the SMD solvation model³⁶ based on the gas-phase optimized geometries. The M06 functional with a mixed basis set of SDD for Pd and 6-311+G(d,p) for other atoms was used for single point energy calculations. Gibbs free energies were calculated at the standard conditions (298K, 1 atm) using Cramer and Truhlar's quasiharmonic approximation³⁴ using Goodvibes v2.0.1.³⁵ Images of structures were generated using CYLview.³⁹

4.3.2 Mechanism of C–H Activation and the Origins of the Atroposelectivity

A plausible catalytic cycle is outlined in **Scheme 4.5**. Following coordination with the condensed imine, a π -alkene complex is formed, and the carboxylate-assisted C–H metalation occurs via a concerted metalation-deprotonation (CMD) to generate a six-membered palladacycle. The exchange of the carboxylate ligand with the electron-deficient alkene is followed by the migratory insertion, β -hydride elimination, and reductive elimination to form the diene product.

The oxidation of the Pd(0) species and coordination of another condensed imine substrate regenerate the catalyst/reactant complex.



Scheme 4.5. Proposed catalytic cycle.

We calculated the reaction energy profiles of the C–H activation of the (*Z*)-alkene **1** with the best-performing 3,4,5-trifluorobenzoic acid (**acid 1**) and *tert*-butyl acrylate as the coupling partner to elucidate the origins of the observed selectivity, and to understand the mechanism of the TDG-promoted Pd-catalyzed C–H activation.

We explored the alkenyl C–H activation pathways with two different π -faces of the alkene binding to the Pd center. The preferred π -face of the substrate coordination to the Pd (**IM1**) indeed leads to the more favorable C–H activation transition state that eventually proceeds to form the experimentally observed atropisomeric product in the reaction with the *ortho*-substituted

substrate **4**. The square planar geometry around the Pd is significantly distorted in the less stable π -alkene complex **IM2**, making it 9.2 kcal/mol higher in energy than **IM1** (Figure 4.8).

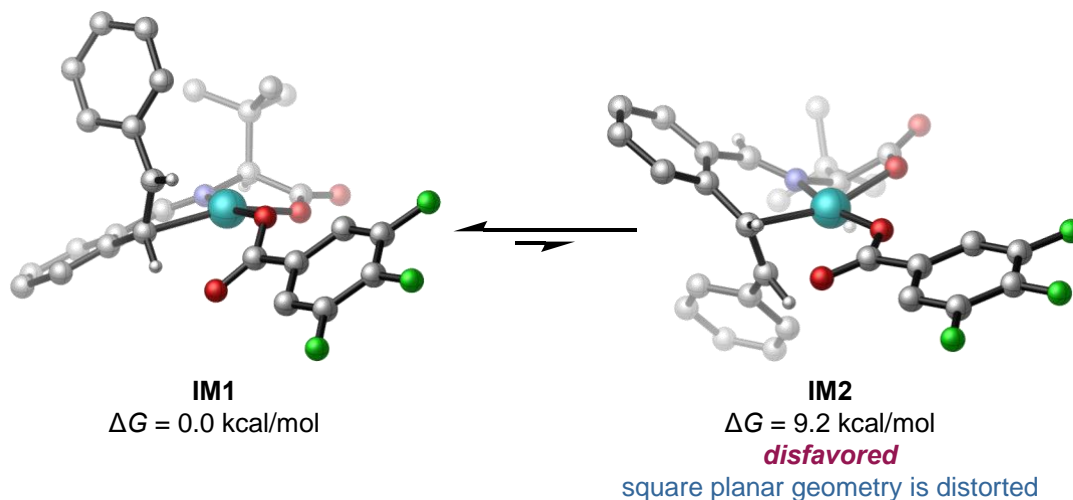


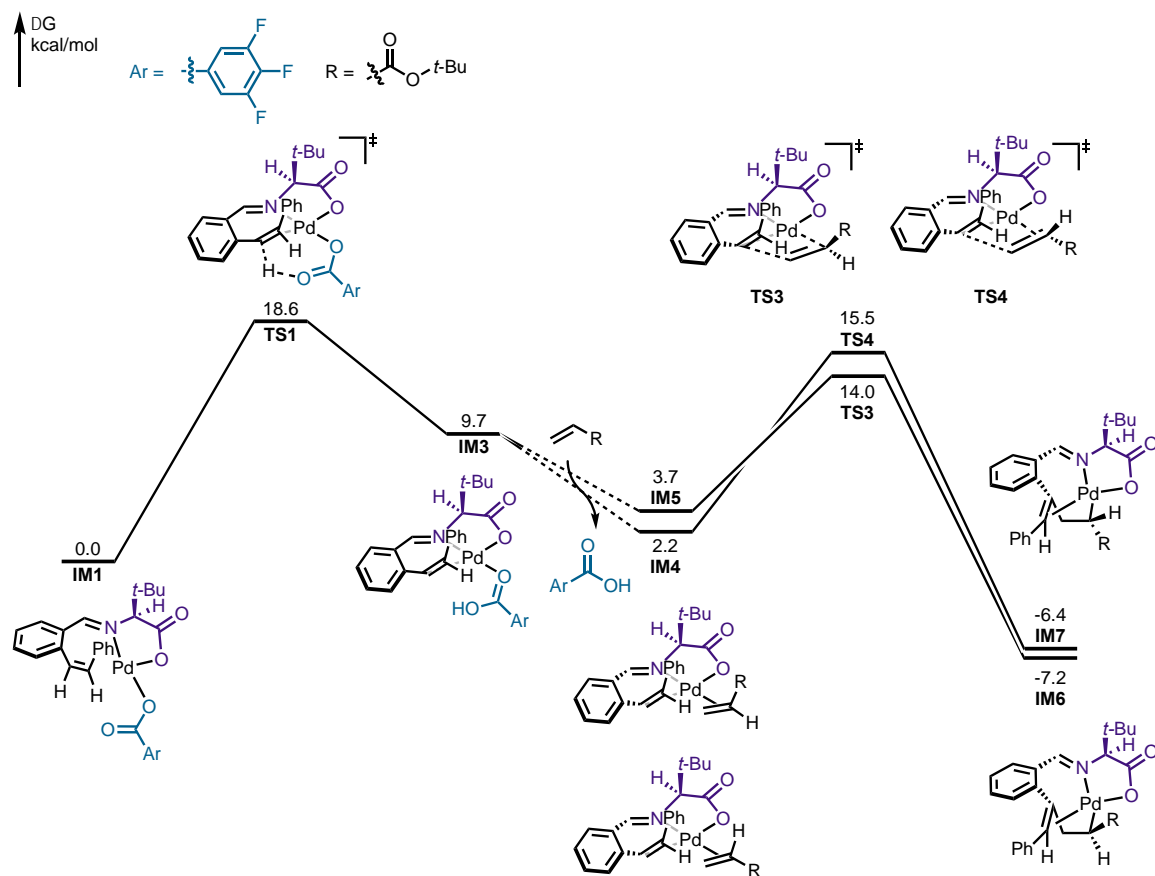
Figure 4.8. Isomers of the π -alkene reactant complex with different π -facial selectivity.

The calculated reaction energy profile of the C–H activation and alkene migratory insertion steps is shown in **Scheme 4.6**. The carboxylate-assisted CMD of the C(alkenyl)–H bond from π -alkene complex **IM1** occurs via **TS1** and has an activation free energy of 18.6 kcal/mol. Following the C–H activation, a six-membered palladacycle (**IM3**) is formed. The coordinated benzoic acid is then replaced by the *tert*-butyl acrylate to form more stable intermediates **IM4** and **IM5** followed by the alkene migratory insertion via transition states **TS4** and **TS3** with activation free energies of 13.3 and 10.3 kcal/mol with respect to **IM4** and **IM5**, respectively.

Experimental studies identified the C–H activation step as the rate-determining step. Our analyses of the DFT-optimized structures revealed that from **IM1** to **TS1**, a slight reorganization of the π -alkene complex occurs to decrease the distortion of the C–H bond in the CMD step, and the metal center acquires a square planar geometry. This change in the geometry of the metal center

causes a distortion of the geometry around the imine. Distortion-interaction analysis of the C–H activation transition states with the Pd center coordinated to the two opposite π -faces of the alkene (**TS1** and **TS2**) revealed that the distortion of the π -alkene palladium complex in **TS1** is lower than that in **TS2**, and the interaction energy between the palladium and the carboxylate anion is stronger in **TS1** (**Figure 4.9**). These results suggest that the less distortion of the forming palladacycle leads to the lower energy of **TS1** compared to **TS2**. In the more favorable transition state **TS1**, the alkenyl group is placed above the plane, on the same side of the *t*-Bu substituent on the chiral TDG. In reactions with substrates containing an *ortho*-substituent that blocks the free rotation about the C(aryl)–C(alkenyl) bond after the C–H palladation (*e.g.* when reacting with substrate **4**), the atroposelectivity in the product is determined in the C–H palladation step. The atropoisomer formed after **TS1** is consistent with the experimentally observed major atropoisomer in the reaction with **4**.

The optimized geometries of the migratory insertion transition states with *tert*-butyl acrylate are depicted in **Figure 4.10**. The migratory insertion transition states with two opposite π -faces of the alkene were considered. **TS3** is 1.5 kcal/mol more stable than **TS4**, potentially attributed to the longer distance between a carboxylate oxygen on the TDG and an oxygen of the *tert*-butyl acrylate (3.57 and 3.13 Å, respectively). These migratory insertion transition states lead to eight-membered palladacycles (**IM6** and **IM7**) that are stabilized by the coordination of the π bond on the γ -carbon and the palladium center.



Scheme 4.6. Calculated reaction energy profile of C–H activation of the (Z)-alkene **1** with 3,4,5-trifluorobenzoic acid (**acid 1**) with *tert*-butyl acrylate as the coupling partner.

Energies are reported with respect to the **IM1**. All energies are in kcal/mol.

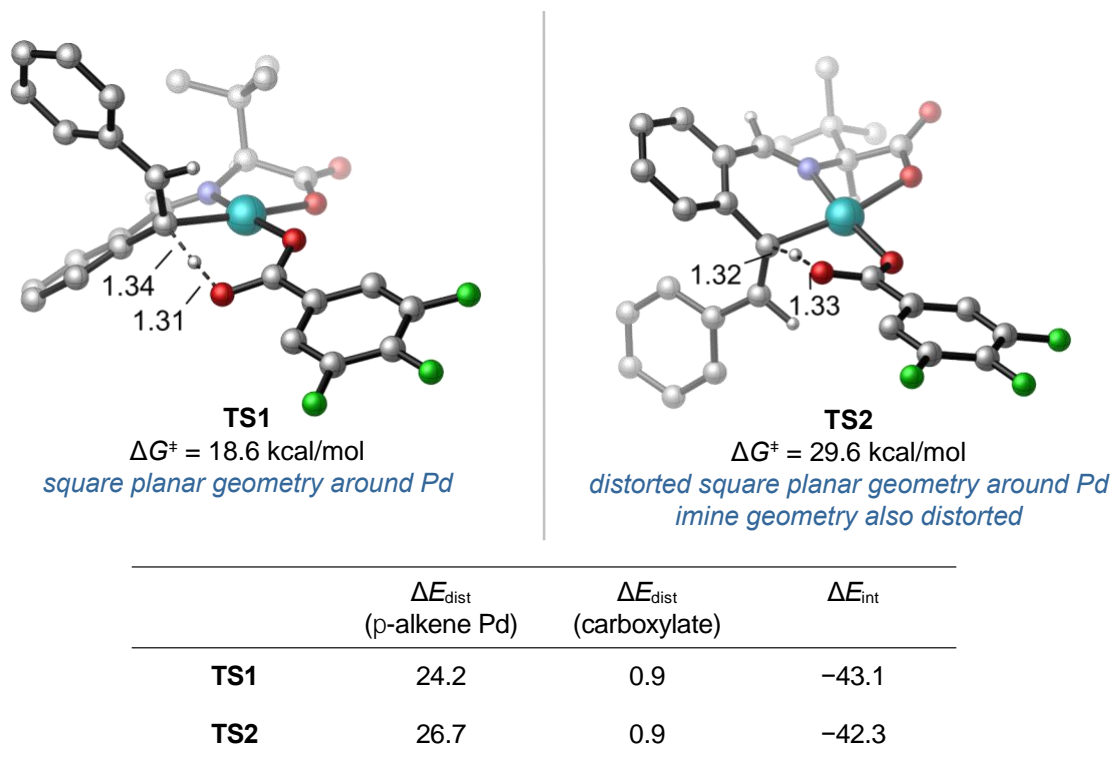


Figure 4.9. Comparison of the C–H activation transition states with the Pd bound to the opposite faces of the alkene, and summary of distortion-interaction analyses of the two transition states.

The activation free energies of the TS are reported with respect to the **IM1**. All energies are in kcal/mol. Distortion energies of the palladacycles are calculated with respect to the three-coordinate π -alkene Pd complexes without the carboxylate anion ligand.

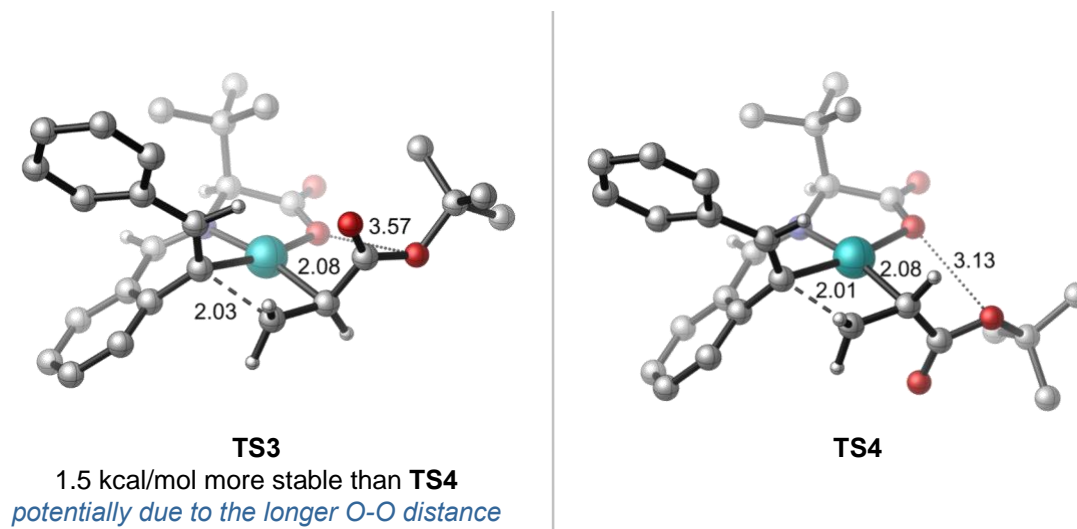


Figure 4.10. Migratory insertion transition states with *tert*-butyl acrylate.

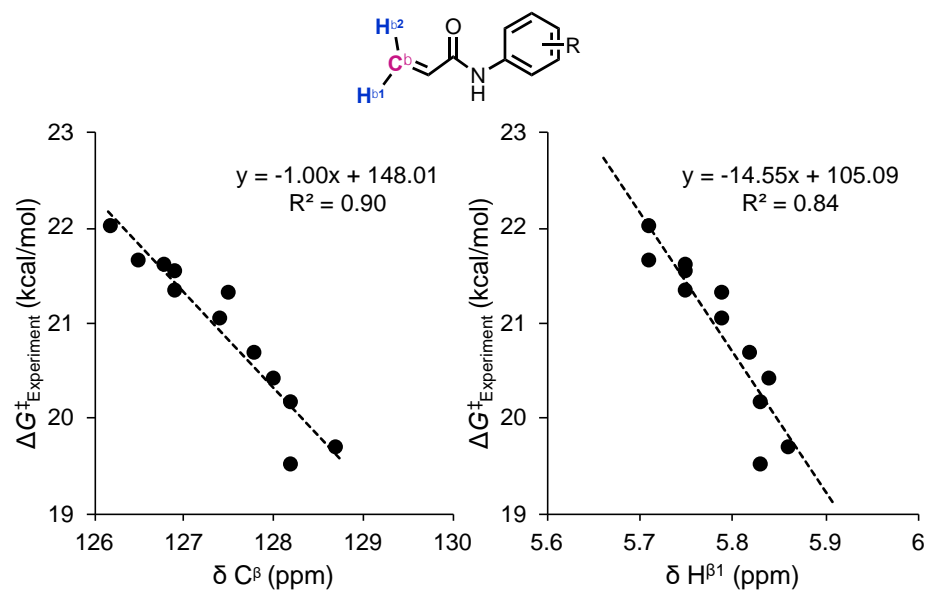
We are continuing our DFT calculations to identify the possible β -hydride elimination transition states from **IM6** that lead to the observed 1,3-diene product. The direct β -hydride elimination from **IM6** appears unlikely due to the strain of the endocyclic β -hydride elimination transition state. The concerted hydride transfer to the imine nitrogen was also computed and found to be unfavorable. We expect that the β -hydride elimination occurs after the dissociation of the directing group, which will alleviate the ring strain and create an empty site for the β -hydride elimination. Although these calculations are still ongoing, we expect the directing group dissociation and β -hydride elimination steps are kinetically facile and are not rate- or selectivity-determining.

4.3.3 Conclusions

In summary, a TDG-promoted Pd-catalyzed C(alkenyl)–H functionalization of the *ortho*-alkenylbenzaldehydes is achieved, which would set the foundation of the studies on alkene–Pd reactivity and inspire the development of C(alkenyl)–H activation in the future. Our DFT studies explored the mechanism of the TDG-promoted C–H activation, and elucidated the origins of the observed atroposelectivity in the synthesis of aryl-substituted 1,3-dienes with hindered rotation about the C(aryl)–C(alkenyl) bond. The catalytic process of C–H activation is initiated by the in situ formation of the imine. A π -alkene complex is formed upon coordination to the Pd center, followed by the carboxylate-assisted concerted C–H metalation-deprotonation to generate a six-membered palladacycle. Upon the exchange of the benzoic acid ligand with the electron-deficient alkene, the migratory insertion occurs, which is then followed by the β -hydride elimination that furnishes the product, and the catalyst is oxidized in the final step and closes the cycle.

Our DFT calculations show that the facial selectivity of the π -alkene coordination is dependent on the TDG. The origin of the observed atroposelectivity lies on the distortion of the palladacycle in the C–H palladation step.

Appendix A ^{13}C and ^1H NMR Shifts (ppm) of *N*-Aryl Acrylamides



Appendix B DFT-Calculated and Experimentally-Determined Barriers of Thiolate

Additions to the α -Methylene- γ -lactams

M06-2X/6-311+G(d,p)(SMD)//M06-2X/6-31+G(d)(SMD)
Nucleophile: Methyl thiolate
All energies are reported in kcal/mol.

entry	compound	$\Delta G^\ddagger_{\text{Experiment}}$	$\Delta G^\ddagger_{\text{DFT, HOA}}$	$\Delta G^\ddagger_{\text{DFT, QHA}}$	$\Delta H^\ddagger_{\text{DFT}}$
1	H (5a)	22.9	13.5	14.7	2.1
2	<i>p</i> -CF ₃ (5b)	22.3	12.6	13.7	1.1
3	<i>p</i> -CN (5c)	21.7	11.9	13.2	0.7
4	<i>p</i> -OMe (5d)	23.3	14.1	15.3	2.6
5	<i>p</i> -F (5e)	23.0	13.1	14.6	2.0
6	<i>p</i> -NO ₂ (5f)	21.0	11.4	12.5	-0.1
7	<i>p</i> -NMe ₂ (5g)	—	14.0	15.7	3.0
8	<i>m</i> -OMe (5h)	23.1	13.1	14.5	1.9
9	<i>m</i> -F (5i)	22.5	12.8	14.1	1.5
10	<i>m</i> -NO ₂ (5j)	22.2	11.8	13.5	0.9
11	<i>o</i> -OMe (5k)	23.5	14.1	15.4	2.7
12	<i>o</i> -F (5l)	23.0	13.6	14.6	2.0
13	<i>o</i> -NO ₂ (5m)	22.0	12.9	13.7	1.1

M06-2X/6-311+G(d,p)(PCM)//M06-2X/6-31+G(d)(PCM)
Nucleophile: Methyl thiolate
All energies are reported in kcal/mol.

entry	compound	$\Delta G^\ddagger_{\text{Experiment}}$	$\Delta G^\ddagger_{\text{DFT, HOA}}$	$\Delta G^\ddagger_{\text{DFT, QHA}}$	$\Delta H^\ddagger_{\text{DFT}}$
1	H (5a)	22.9	17.5	18.6	6.0
2	<i>p</i> -CF ₃ (5b)	22.3	16.2	17.1	4.4
3	<i>p</i> -CN (5c)	21.7	15.3	16.5	3.8
4	<i>p</i> -OMe (5d)	23.3	19.7	21.2	8.7
5	<i>p</i> -F (5e)	23.0	17.5	18.5	5.9
6	<i>p</i> -NO ₂ (5f)	21.0	14.7	15.6	3.0
7	<i>p</i> -NMe ₂ (5g)	—	19.5	20.5	7.5
8	<i>m</i> -OMe (5h)	23.1	17.7	18.6	5.9
9	<i>m</i> -F (5i)	22.5	16.9	17.8	5.1
10	<i>m</i> -NO ₂ (5j)	22.2	15.7	16.9	4.2
11	<i>o</i> -OMe (5k)	23.5	19.7	20.4	7.5
12	<i>o</i> -F (5l)	23.0	18.1	18.9	6.1
13	<i>o</i> -NO ₂ (5m)	22.0	17.1	17.7	4.9

B3LYP/6-311+G(d,p)(SMD)/B3LYP/6-31+G(d)(SMD)

Nucleophile: Methyl thiolate

All energies are reported in kcal/mol.

entry	compound	$\Delta G^\ddagger_{\text{Experiment}}$	$\Delta G^\ddagger_{\text{DFT, HOA}}$	$\Delta G^\ddagger_{\text{DFT, QHA}}$	$\Delta H^\ddagger_{\text{DFT}}$
1	H (5a)	22.9	18.1	19.1	6.7
2	<i>p</i> -CF ₃ (5b)	22.3	16.4	17.5	5.0
3	<i>p</i> -CN (5c)	21.7	15.3	16.6	4.3
4	<i>p</i> -OMe (5d)	23.3	18.8	20.0	7.4
5	<i>p</i> -F (5e)	23.0	17.9	19.0	6.5
6	<i>p</i> -NO ₂ (5f)	21.0	12.6	14.6	2.4
7	<i>p</i> -NMe ₂ (5g)	–	19.6	20.8	8.2
8	<i>m</i> -OMe (5h)	23.1	17.6	19.0	6.5
9	<i>m</i> -F (5i)	22.5	17.0	18.1	5.7
10	<i>m</i> -NO ₂ (5j)	22.2	16.2	17.4	4.9
11	<i>o</i> -OMe (5k)	23.5	19.7	20.5	7.9
12	<i>o</i> -F (5l)	23.0	18.0	19.1	6.6
13	<i>o</i> -NO ₂ (5m)	22.0	17.4	17.7	5.0

B3LYP/6-311+G(d,p)(PCM)/B3LYP/6-31+G(d)(PCM)

Nucleophile: Methyl thiolate

All energies are reported in kcal/mol.

entry	compound	$\Delta G^\ddagger_{\text{Experiment}}$	$\Delta G^\ddagger_{\text{DFT, HOA}}$	$\Delta G^\ddagger_{\text{DFT, QHA}}$	$\Delta H^\ddagger_{\text{DFT}}$
1	H (5a)	22.9	22.6	23.4	11.0
2	<i>p</i> -CF ₃ (5b)	22.3	20.0	21.1	8.6
3	<i>p</i> -CN (5c)	21.7	19.0	20.2	7.7
4	<i>p</i> -OMe (5d)	23.3	24.0	24.7	12.1
5	<i>p</i> -F (5e)	23.0	22.3	23.2	10.7
6	<i>p</i> -NO ₂ (5f)	21.0	17.4	18.2	5.8
7	<i>p</i> -NMe ₂ (5g)	–	25.6	26.2	13.3
8	<i>m</i> -OMe (5h)	23.1	22.7	23.4	10.9
9	<i>m</i> -F (5i)	22.5	21.4	22.2	9.7
10	<i>m</i> -NO ₂ (5j)	22.2	20.2	21.1	8.5
11	<i>o</i> -OMe (5k)	23.5	25.9	26.2	13.4
12	<i>o</i> -F (5l)	23.0	23.5	24.1	11.3
13	<i>o</i> -NO ₂ (5m)	22.0	21.4	22.5	9.9

M06-2X/6-311+G(d,p)(SMD)//M06-2X/6-31+G(d)(SMD)

Nucleophile: Cysteamine thiolate

All energies are reported in kcal/mol.

entry	compound	$\Delta G^\ddagger_{\text{Experiment}}$	$\Delta G^\ddagger_{\text{DFT, HOA}}$	$\Delta G^\ddagger_{\text{DFT, QHA}}$	$\Delta H^\ddagger_{\text{DFT}}$
1	H (5a)	22.9	13.9	15.0	0.8
2	<i>p</i> -CF ₃ (5b)	22.3	12.2	13.9	-0.4
3	<i>p</i> -CN (5c)	21.7	11.6	13.2	-0.8
4	<i>p</i> -OMe (5d)	23.3	13.1	15.5	1.3
5	<i>p</i> -F (5e)	23.0	13.8	14.9	0.7
6	<i>p</i> -NO ₂ (5f)	21.0	11.3	12.5	-1.6
7	<i>p</i> -NMe ₂ (5g)	–	14.6	16.3	1.8
8	<i>m</i> -OMe (5h)	23.1	13.0	14.7	0.5
9	<i>m</i> -F (5i)	22.5	13.3	14.3	0.1
10	<i>m</i> -NO ₂ (5j)	22.2	12.4	13.8	-0.4
11	<i>o</i> -OMe (5k)	23.5	14.1	15.8	1.5
12	<i>o</i> -F (5l)	23.0	12.5	14.9	0.8
13	<i>o</i> -NO ₂ (5m)	22.0	12.2	13.6	-0.8

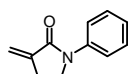
M06-2X/6-311+G(d,p)(SMD)//M06-2X/6-31+G(d)(SMD)

Compounds: *N*-aryl acrylamides Nucleophile: Methyl thiolate

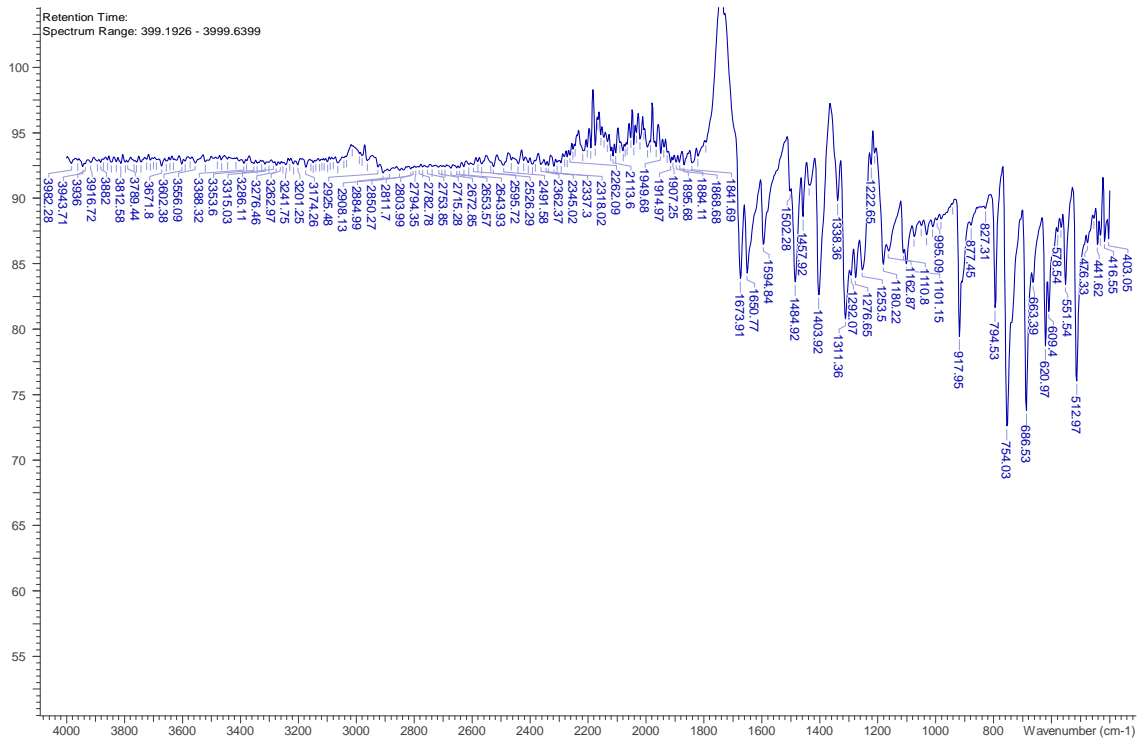
All energies are reported in kcal/mol.

entry	compound	$\Delta G^\ddagger_{\text{Experiment}}$	$\Delta G^\ddagger_{\text{DFT, HOA}}$	$\Delta G^\ddagger_{\text{DFT, QHA}}$	$\Delta H^\ddagger_{\text{DFT}}$
1	H	21.6	11.6	12.7	0.6
2	<i>p</i> -CF ₃	20.7	9.9	11.2	0.1
3	<i>p</i> -CN	20.2	10.1	11.3	-0.8
4	<i>p</i> -OMe	22.0	11.4	12.9	0.8
5	<i>p</i> -F	21.5	12.2	12.5	0.3
6	<i>p</i> -NO ₂	19.7	9.3	10.5	-1.5
7	<i>p</i> -NMe ₂	–	–	–	–
8	<i>m</i> -OMe	21.3	11.0	12.0	0.2
9	<i>m</i> -F	21.0	11.8	12.2	0.0
10	<i>m</i> -NO ₂	20.4	10.1	11.7	-0.4
11	<i>o</i> -OMe	21.6	12.0	13.2	0.7
12	<i>o</i> -F	21.3	11.5	12.0	-0.1
13	<i>o</i> -NO ₂	19.5	9.2	10.7	-1.4

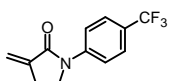
Appendix C IR Spectra of *N*-Aryl α -Methylene- γ -Lactams



5a

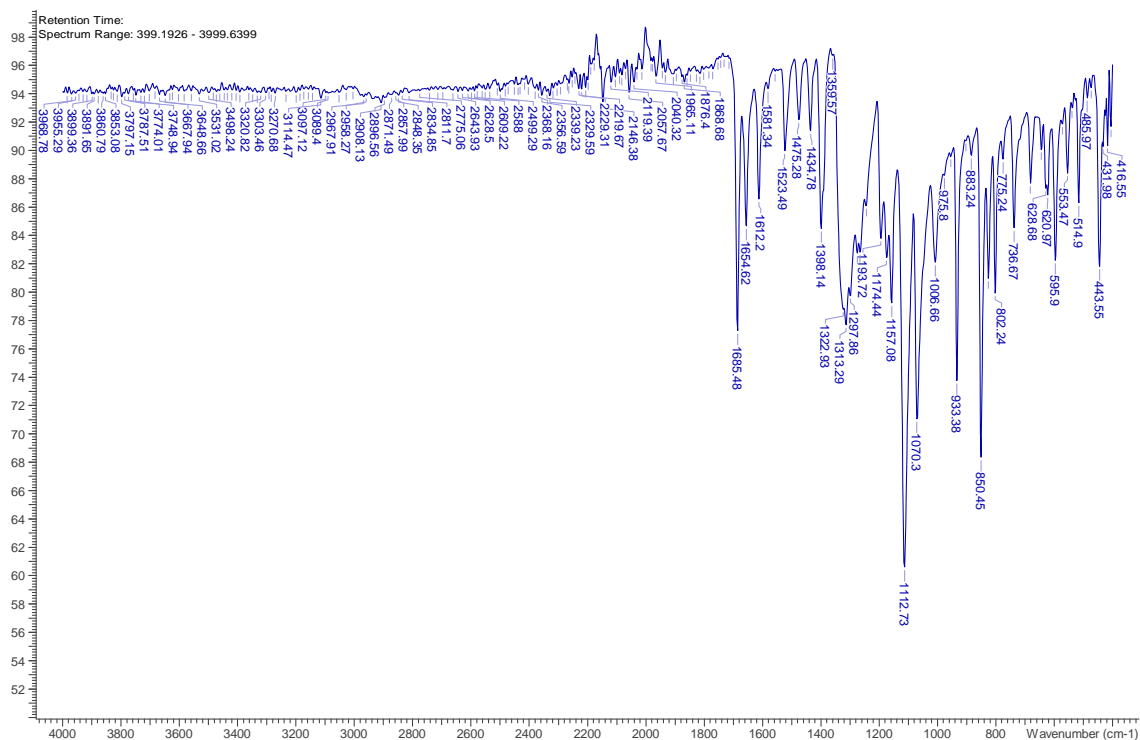


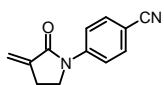
TGE-01-114



5b

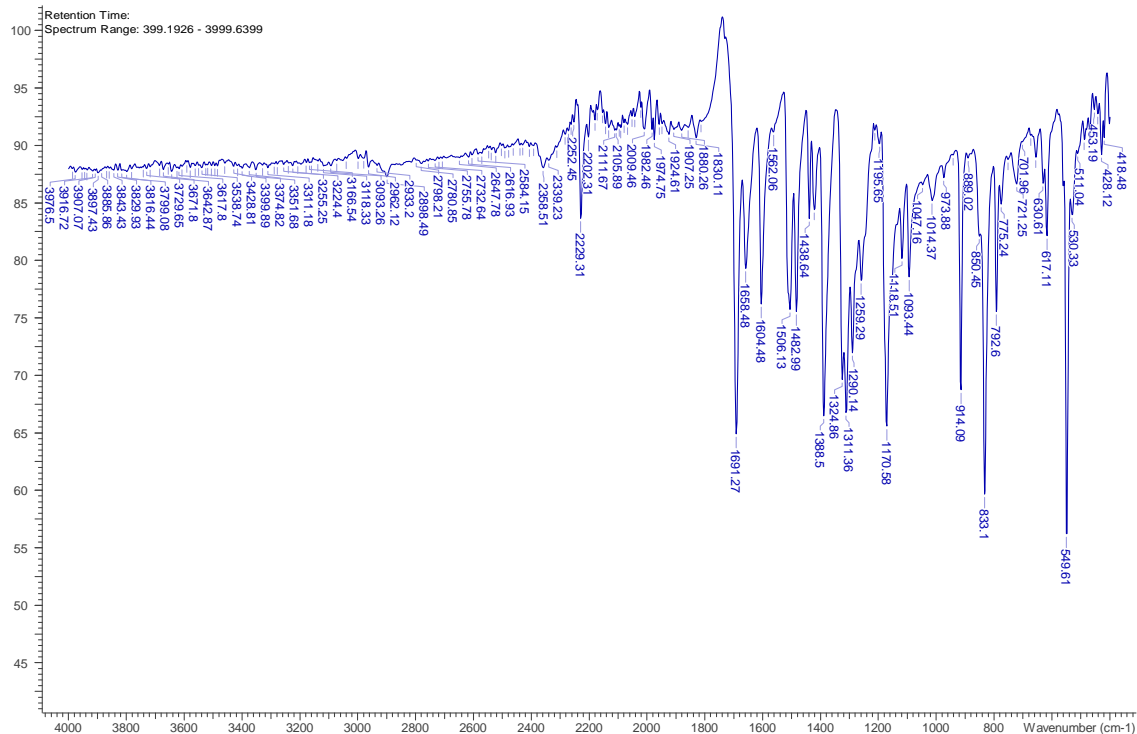
TGE-01-106

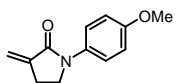




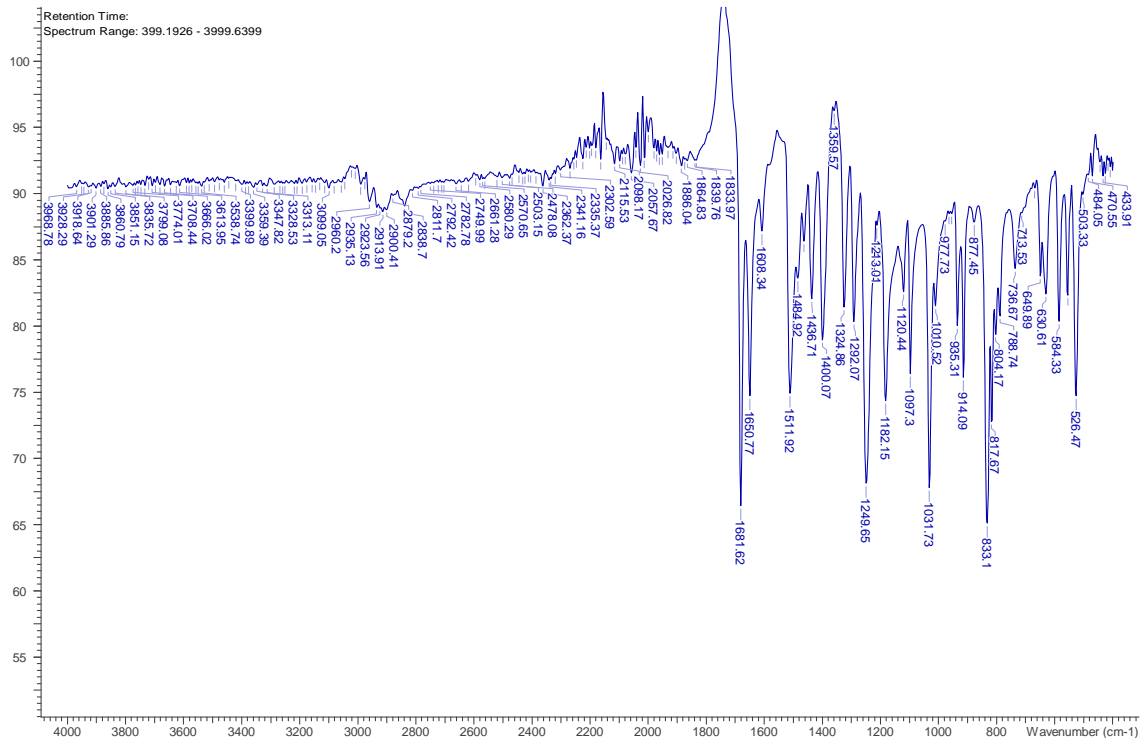
5c

TGE-01-166





5d

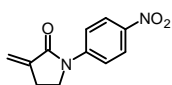


TGE-01-108



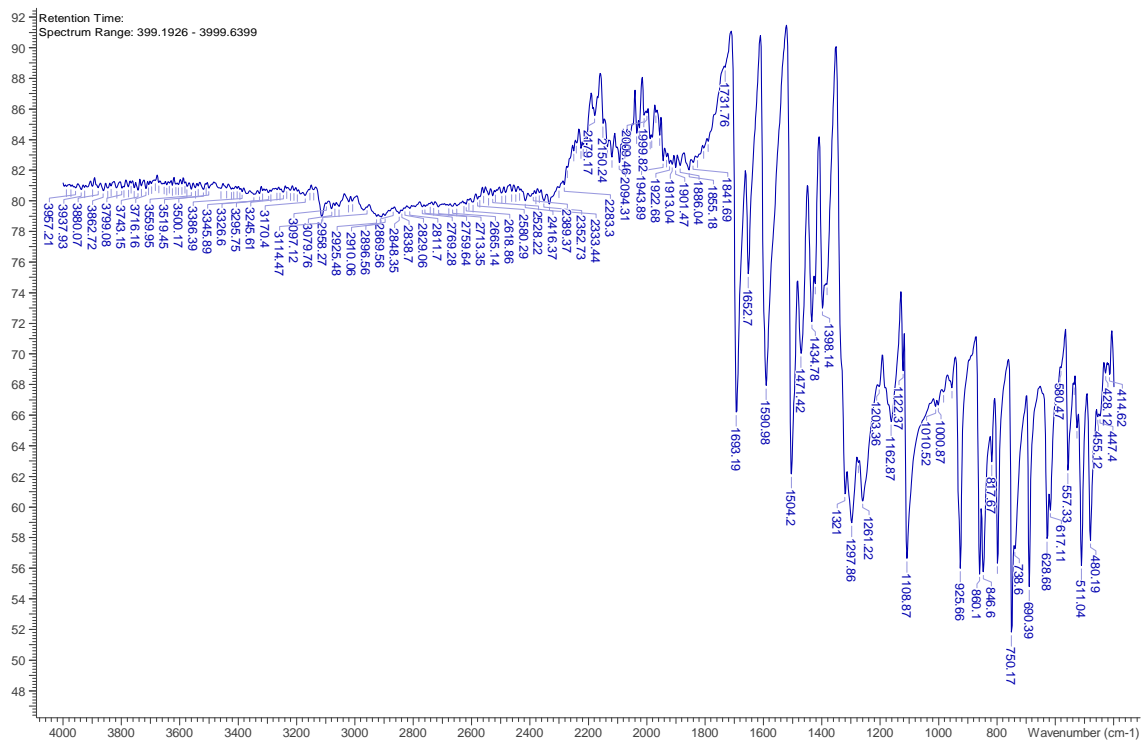
Retention Time:
Spectrum Range: 399.1926 - 3999.6399

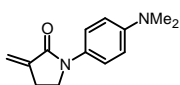




5f

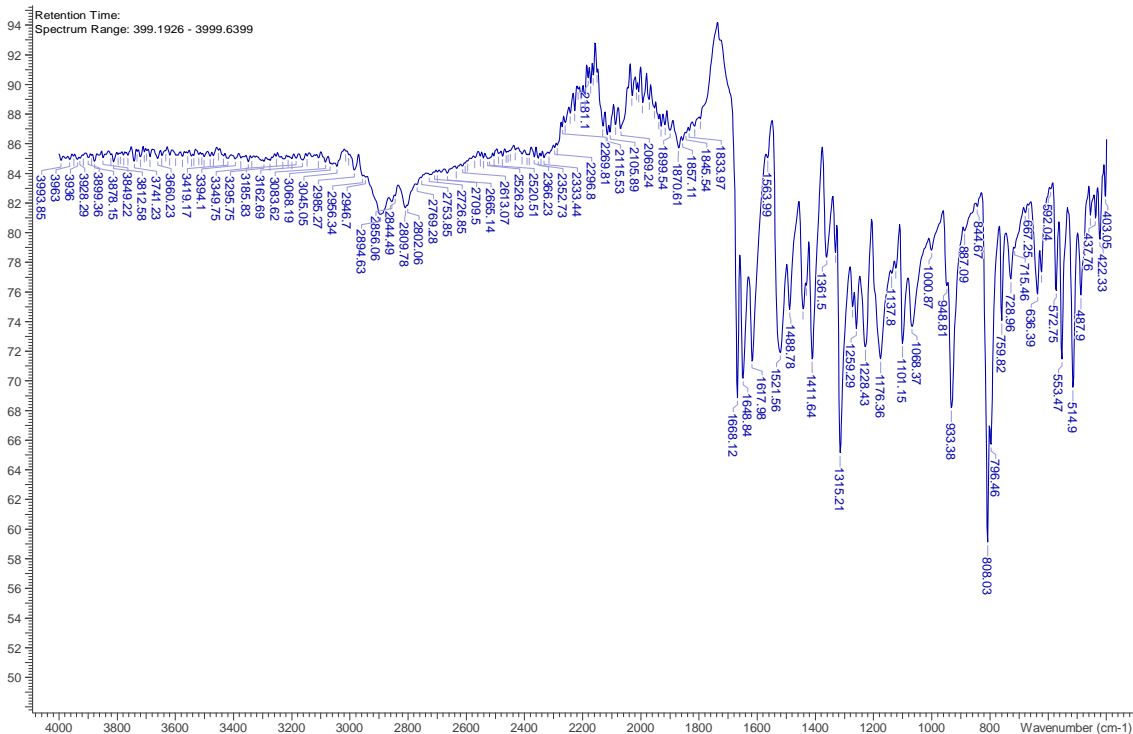
TGE-01-140





5g

TGE-01-142



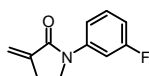
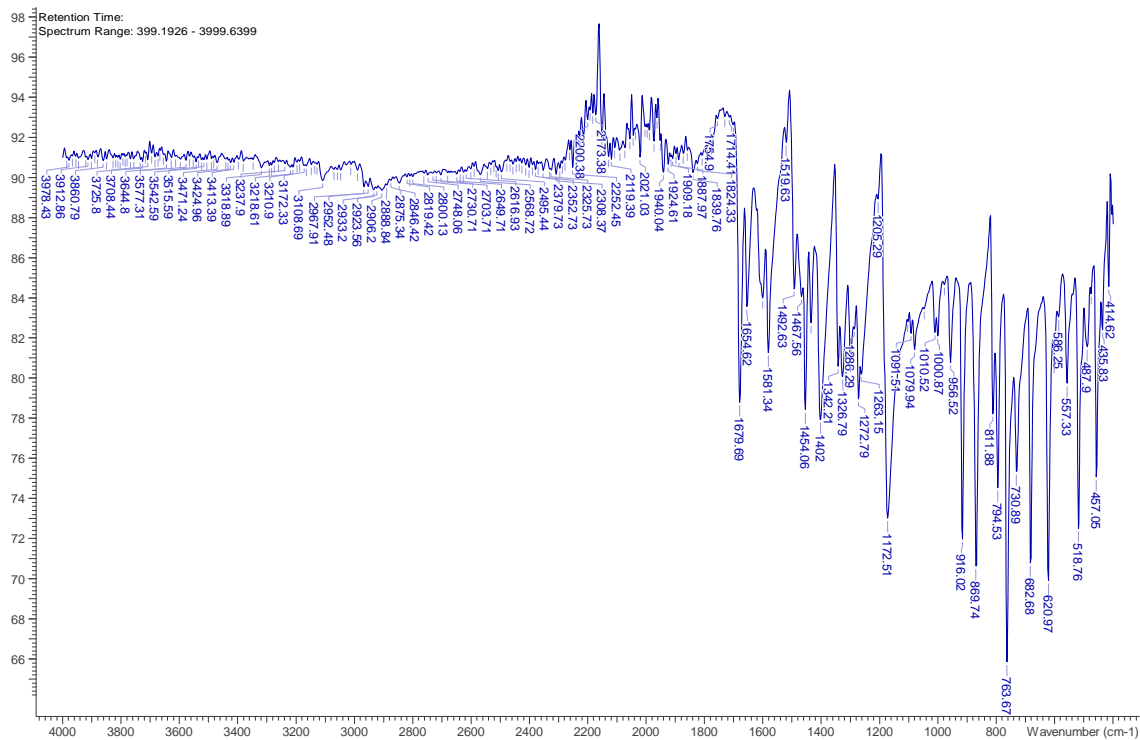


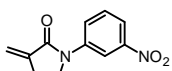
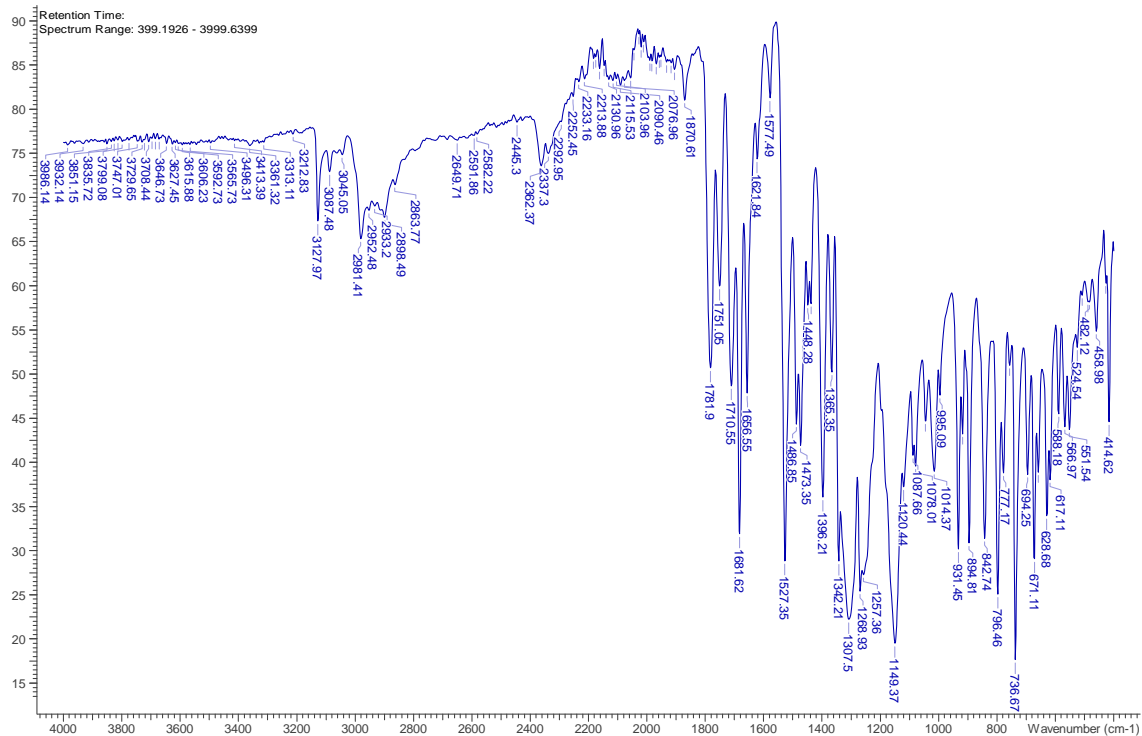
Retention Time: 399.1926 - 3999.6399

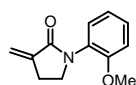
Wavenumber (cm⁻¹)

Key peaks (Wavenumber, cm⁻¹):

- 414.62
- 451.26
- 464.76
- 532.26
- 549.61
- 572.75
- 624.82
- 659.18
- 688.46
- 730.89
- 755.6
- 790.67
- 833.1
- 898.31
- 908.31
- 933.16
- 993.16
- 1004.73
- 1051.01
- 1097.3
- 1174.44
- 1211.08
- 1259.93
- 1278.57
- 1346.07
- 1402
- 1446.35
- 1455.99
- 1477.21
- 1579.41
- 1650.77
- 1675.84
- 1862.9
- 1918.82
- 1982.32
- 2005.61
- 2032.6
- 2051.89
- 2096.24
- 2105.39
- 2173.51
- 2183.51
- 2233.16
- 2244.74
- 2273.86
- 2331.52
- 2341.16
- 2360.44
- 2400.94
- 2541.72
- 2593.36
- 2728.78
- 2786.63
- 2819.42
- 2852.92
- 2882.7
- 2892.2
- 2913.91
- 2931.27
- 2960.2
- 2996.84
- 3099.05
- 3141.03
- 3351.88
- 3403.74
- 3473.17
- 3517.52
- 3561.02
- 3635.16
- 3723.87
- 3733.58
- 3743.8
- 3781.72
- 3793.29
- 3862.72
- 3888.72
- 3897.43
- 3892.14
- 3864.93
- 3869.52

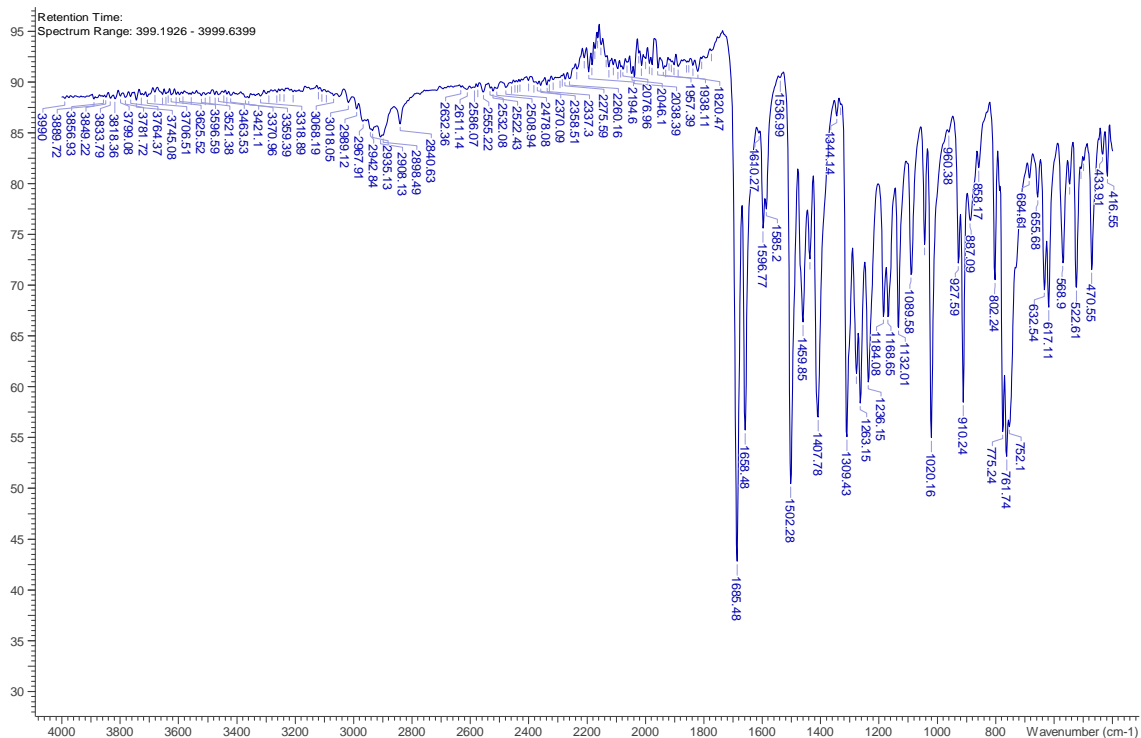
**5i**

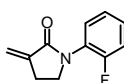
**5j**



5k

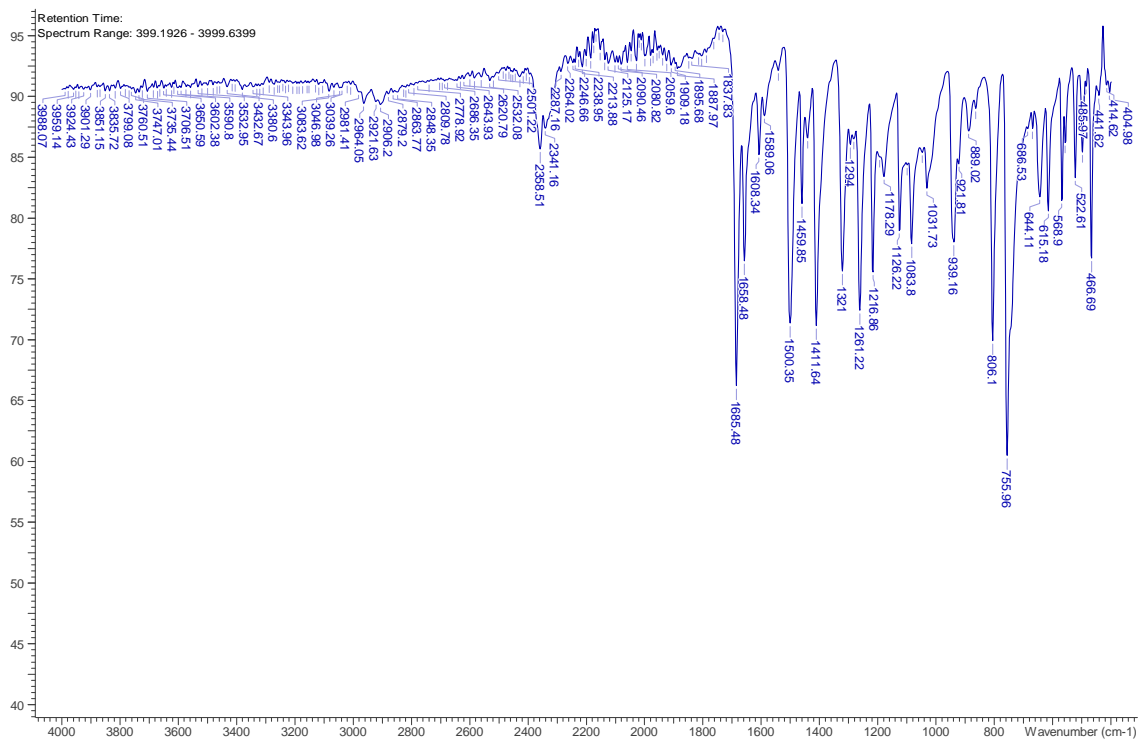
TGE-01-190



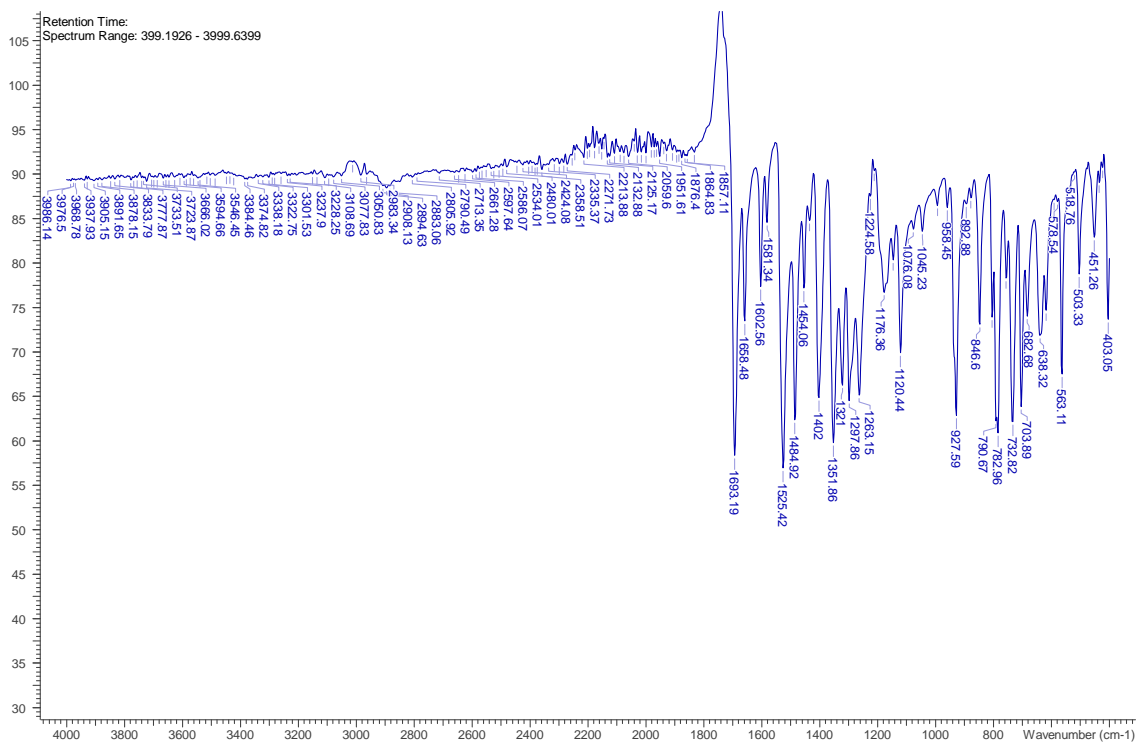


51

TGE-01-180



Retention Time:
Spectrum Range: 399.1926 - 3999.6399



Bibliography

1. Fabbro, D.; Cowan-Jacob, S. W.; Moebitz, H., Ten Things You Should Know About Protein Kinases: IUPHAR Review 14. *British Journal of Pharmacology* **2015**, *172*, 2675–2700.
2. Zhang, J.; Yang, P. L.; Gray, N. S., Targeting Cancer with Small Molecule Kinase Inhibitors. *Nature Reviews Cancer* **2009**, *9*, 28–39.
3. Cohen, P., Protein Kinases--The Major Drug Targets of the Twenty-First Century? *Nature Reviews Drug Discovery* **2002**, *1*, 309–315.
4. Ferguson, F. M.; Gray, N. S., Kinase Inhibitors: The Road Ahead. *Nature Reviews Drug Discovery* **2018**, *17*, 353–377.
5. Barf, T.; Kaptein, A., Irreversible Protein Kinase Inhibitors: Balancing the Benefits and Risks. *Journal of Medicinal Chemistry* **2012**, *55*, 6243–6262.
6. Abdeldayem, A.; Raouf, Y. S.; Constantinescu, S. N.; Moriggl, R.; Gunning, P. T., Advances in Covalent Kinase Inhibitors. *Chemical Society Reviews* **2020**, *49*, 2617–2687.
7. Greig, S. L., Osimertinib: First Global Approval. *Drugs* **2016**, *76*, 263–273.
8. Callegari, D.; Ranaghan, K. E.; Woods, C. J.; Minari, R.; Tiseo, M.; Mor, M.; Mulholland, A. J.; Lodola, A., L718Q Mutant EGFR Escapes Covalent Inhibition by Stabilizing a Non-reactive Conformation of the Lung Cancer Drug Osimertinib. *Chemical Science* **2018**, *9*, 2740–2749.
9. Walter, A. O.; Sjin, R. T. T.; Haringsma, H. J.; Ohashi, K.; Sun, J.; Lee, K.; Dubrovskiy, A.; Labenski, M.; Zhu, Z.; Wang, Z.; Sheets, M.; St Martin, T.; Karp, R.; van Kalken, D.; Chaturvedi, P.; Niu, D.; Nacht, M.; Petter, R. C.; Westlin, W.; Lin, K.; Jaw-Tsai, S.; Raponi, M.; Van Dyke, T.; Etter, J.; Weaver, Z.; Pao, W.; Singh, J.; Simmons, A. D.; Harding, T. C.; Allen,

A., Discovery of a Mutant-Selective Covalent Inhibitor of EGFR that Overcomes T790M-Mediated Resistance in NSCLC. *Cancer Discovery* **2013**, *3*, 1404–1415.

10. Thress, K. S.; Paweletz, C. P.; Felip, E.; Cho, B. C.; Stetson, D.; Dougherty, B.; Lai, Z.; Markovets, A.; Vivancos, A.; Kuang, Y.; Ercan, D.; Matthews, S. E.; Cantarini, M.; Barrett, J. C.; Jänne, P. A.; Oxnard, G. R., Acquired EGFR C797S Mutation Mediates Resistance to AZD9291 in Non-small Cell Lung Cancer Harboring EGFR T790M. *Nature Medicine* **2015**, *21*, 560–562.

11. Janecka, A.; Wyrebska, A.; Gach, K.; Fichna, J.; Janecki, T., Natural and Synthetic α -Methylenelactones and α -Methylenelactams with Anticancer Potential. *Drug Discovery Today* **2012**, *17*, 561–572.

12. Ghantous, A.; Gali-Muhtasib, H.; Vuorela, H.; Saliba, N. A.; Darwiche, N., What Made Sesquiterpene Lactones Reach Cancer Clinical Trials? *Drug Discovery Today* **2010**, *15*, 668–678.

13. Cee, V. J.; Volak, L. P.; Chen, Y.; Bartberger, M. D.; Tegley, C.; Arvedson, T.; McCarter, J.; Tasker, A. S.; Fotsch, C., Systematic Study of the Glutathione (GSH) Reactivity of *N*-Arylacrylamides: 1. Effects of Aryl Substitution. *Journal of Medicinal Chemistry* **2015**, *58*, 9171–9178.

14. Flanagan, M. E.; Abramite, J. A.; Anderson, D. P.; Aulabaugh, A.; Dahal, U. P.; Gilbert, A. M.; Li, C.; Montgomery, J.; Oppenheimer, S. R.; Ryder, T.; Schuff, B. P.; Uccello, D. P.; Walker, G. S.; Wu, Y.; Brown, M. F.; Chen, J. M.; Hayward, M. M.; Noe, M. C.; Obach, R. S.; Philippe, L.; Shanmugasundaram, V.; Shapiro, M. J.; Starr, J.; Stroh, J.; Che, Y., Chemical and Computational Methods for the Characterization of Covalent Reactive Groups for the Prospective Design of Irreversible Inhibitors. *Journal of Medicinal Chemistry* **2014**, *57*, 10072–10079.

15. Birkholz, A.; Kopecky, D. J.; Volak, L. P.; Bartberger, M. D.; Chen, Y.; Tegley, C. M.; Arvedson, T.; McCarter, J. D.; Fotsch, C.; Cee, V. J., Systematic Study of the Glutathione

Reactivity of *N*-Phenylacrylamides: 2. Effects of Acrylamide Substitution. *Journal of Medicinal Chemistry* **2020**, *63*, 11602–11614.

16. Krenske, E. H.; Petter, R. C.; Zhu, Z.; Houk, K. N., Transition States and Energetics of Nucleophilic Additions of Thiols to Substituted α,β -Unsaturated Ketones: Substituent Effects Involve Enone Stabilization, Product Branching, and Solvation. *The Journal of Organic Chemistry* **2011**, *76*, 5074–5081.

17. Krenske, E. H.; Petter, R. C.; Houk, K. N., Kinetics and Thermodynamics of Reversible Thiol Additions to Mono- and Diactivated Michael Acceptors: Implications for the Design of Drugs That Bind Covalently to Cysteines. *Journal of Organic Chemistry* **2016**, *81*, 11726–11733.

18. Krishnan, S.; Miller, R. M.; Tian, B.; Mullins, R. D.; Jacobson, M. P.; Taunton, J., Design of Reversible, Cysteine-Targeted Michael Acceptors Guided by Kinetic and Computational Analysis. *Journal of the American Chemical Society* **2014**, *136*, 12624–12630.

19. Allgäuer, D. S.; Jangra, H.; Asahara, H.; Li, Z.; Chen, Q.; Zipse, H.; Ofial, A. R.; Mayr, H., Quantification and Theoretical Analysis of the Electrophilicities of Michael Acceptors. *Journal of the American Chemical Society* **2017**, *139*, 13318–13329.

20. Mulliner, D.; Wondrousch, D.; Schuurmann, G., Predicting Michael-Acceptor Reactivity and Toxicity Through Quantum Chemical Transition State Calculations. *Organic & Biomolecular Chemistry* **2011**, *9*, 8400–8412.

21. Schwöbel, J. A. H.; Wondrousch, D.; Koleva, Y. K.; Madden, J. C.; Cronin, M. T. D.; Schuurmann, G., Prediction of Michael-Type Acceptor Reactivity Toward Glutathione. *Chemical Research in Toxicology* **2010**, *23*, 1576–1585.

22. Wondrousch, D.; Böhme, A.; Thaens, D.; Ost, N.; Schüürmann, G., Local Electrophilicity Predicts the Toxicity-relevant Reactivity of Michael Acceptors. *Journal of Physical Chemistry Letters* **2010**, *1*, 1605–1610.
23. Lonsdale, R.; Burgess, J.; Colclough, N.; Davies, N. L.; Lenz, E. M.; Orton, A. L.; Ward, R. A., Expanding the Armory: Predicting and Tuning Covalent Warhead Reactivity. *Journal of Chemical Information and Modeling* **2017**, *57*, 3124–3137.
24. Capoferri, L.; Lodola, A.; Rivara, S.; Mor, M., Quantum Mechanics/Molecular Mechanics Modeling of Covalent Addition Between EGFR–Cysteine 797 and *N*-(4-Anilinoquinazolin-6-yl) Acrylamide. *Journal of Chemical Information and Modeling* **2015**, *55*, 589–599.
25. Paasche, A.; Schiller, M.; Schirmeister, T.; Engels, B., Mechanistic Study of the Reaction of Thiol-containing Enzymes with α,β -Unsaturated Carbonyl Substrates by Computation and Chemoassays. *ChemMedChem* **2010**, *5*, 869–880.
26. Berteotti, A.; Vacondio, F.; Lodola, A.; Bassi, M.; Silva, C.; Mor, M.; Cavalli, A., Predicting the Reactivity of Nitrile-Carrying Compounds with Cysteine: A Combined Computational and Experimental Study. *ACS Medicinal Chemistry Letters* **2014**, *5*, 501–505.
27. Craven, P.; Aimon, A.; Dow, M.; Fleury-Bregeot, N.; Guilleux, R.; Morgentin, R.; Roche, D.; Kalliokoski, T.; Foster, R.; Marsden, S. P.; Nelson, A., Design, Synthesis and Decoration of Molecular Scaffolds for Exploitation in the Production of Alkaloid-like Libraries. *Bioorganic and Medicinal Chemistry* **2015**, *23*, 2629–2635.
28. Klapars, A.; Huang, X.; Buchwald, S. L., A General and Efficient Copper Catalyst for the Amidation of Aryl Halides. *Journal of the American Chemical Society* **2002**, *124*, 7421–7428.
29. Ward, R. A.; Anderton, M. J.; Ashton, S.; Bethel, P. A.; Box, M.; Butterworth, S.; Colclough, N.; Chorley, C. G.; Chuaqui, C.; Cross, D. A. E.; Dakin, L. A.; Debreczeni, J. É.;

Eberlein, C.; Finlay, M. R. V.; Hill, G. B.; Grist, M.; Klinowska, T. C. M.; Lane, C.; Martin, S.; Orme, J. P.; Smith, P.; Wang, F.; Waring, M. J., Structure- and Reactivity-Based Development of Covalent Inhibitors of the Activating and Gatekeeper Mutant Forms of the Epidermal Growth Factor Receptor (EGFR). *Journal of Medicinal Chemistry* **2013**, *56*, 7025–7048.

30. Frisch, M. J.; Trucks, G. W.; Schlegel, H. B.; Scuseria, G. E.; Robb, M. A.; Cheeseman, J. R.; Scalmani, G.; Barone, V.; Petersson, G. A.; Nakatsuji, H.; Li, X.; Caricato, M.; Marenich, A. V.; Bloino, J.; Janesko, B. G.; Gomperts, R.; Mennucci, B.; Hratchian, H. P.; Ortiz, J. V.; Izmaylov, A. F.; Sonnenberg, J. L.; Williams; Ding, F.; Lipparini, F.; Egidi, F.; Goings, J.; Peng, B.; Petrone, A.; Henderson, T.; Ranasinghe, D.; Zakrzewski, V. G.; Gao, J.; Rega, N.; Zheng, G.; Liang, W.; Hada, M.; Ehara, M.; Toyota, K.; Fukuda, R.; Hasegawa, J.; Ishida, M.; Nakajima, T.; Honda, Y.; Kitao, O.; Nakai, H.; Vreven, T.; Throssell, K.; Montgomery Jr., J. A.; Peralta, J. E.; Ogliaro, F.; Bearpark, M. J.; Heyd, J. J.; Brothers, E. N.; Kudin, K. N.; Staroverov, V. N.; Keith, T. A.; Kobayashi, R.; Normand, J.; Raghavachari, K.; Rendell, A. P.; Burant, J. C.; Iyengar, S. S.; Tomasi, J.; Cossi, M.; Millam, J. M.; Klene, M.; Adamo, C.; Cammi, R.; Ochterski, J. W.; Martin, R. L.; Morokuma, K.; Farkas, O.; Foresman, J. B.; Fox, D. J. *Gaussian 16 Rev. C.01*, Wallingford, CT, **2016**.

31. Zhao, Y.; Truhlar, D. G., The M06 Suite of Density Functionals for Main Group Thermochemistry, Thermochemical Kinetics, Noncovalent Interactions, Excited States, and Transition Elements: Two New Functionals and Systematic Testing of Four M06-Class Functionals and 12 Other Functionals. *Theoretical Chemistry Accounts* **2008**, *120*, 215–241.

32. Becke, A., Density-Functional Thermochemistry-III: The Role of Exact Exchange. *J. Chem. Phys* **1993**, *98*, 5648–5652.

33. Lee, C.; Yang, W.; Parr, R. G., Development of the Colle-Salvetti Correlation-Energy Formula into a Functional of the Electron Density. *Physical Review B* **1988**, *37*, 785–789.
34. Ribeiro, R. F.; Marenich, A. V.; Cramer, C. J.; Truhlar, D. G., Use of Solution-Phase Vibrational Frequencies in Continuum Models for the Free Energy of Solvation. *Journal of Physical Chemistry B* **2011**, *115*, 14556–14562.
35. Luchini, G.; Alegre-Requena, J.; Funes-Ardoiz, I.; Paton, R., GoodVibes: Automated Thermochemistry for Heterogeneous Computational Chemistry Data [Version 1; peer review: 2 approved with reservations]. *FI000Research* **2020**, *9*, 291–299.
36. Marenich, A. V.; Cramer, C. J.; Truhlar, D. G., Universal Solvation Model Based on Solute Electron Density and on a Continuum Model of the Solvent Defined by the Bulk Dielectric Constant and Atomic Surface Tensions. *Journal of Physical Chemistry B* **2009**, *113*, 6378–6396.
37. Mennucci, B.; Tomasi, J.; Cammi, R.; Cheeseman, J. R.; Frisch, M. J.; Devlin, F. J.; Gabriel, S.; Stephens, P. J., Polarizable Continuum Model (PCM) Calculations of Solvent Effects on Optical Rotations of Chiral Molecules. *The Journal of Physical Chemistry A* **2002**, *106*, 6102–6113.
38. Tomasi, J.; Mennucci, B.; Cammi, R., Quantum Mechanical Continuum Solvation Models. *Chemical Reviews* **2005**, *105*, 2999–3094.
39. Legault, C. Y. *CYLview20*, Université de Sherbrooke, **2020**.
40. Werner, H.-J.; Knowles, P. J.; Manby, F. R.; Black, J. A.; Doll, K.; Heßelmann, A.; Kats, D.; Köhn, A.; Korona, T.; Kreplin, D. A.; Ma, Q.; Miller III, T. F.; Mitrushchenkov, A.; Peterson, K. A.; Polyak, I.; Rauhut, G.; Sibae, M., The Molpro Quantum Chemistry Package. *The Journal of Chemical Physics* **2020**, *152*, 144107–144131.

41. Werner, H.-J.; Knowles, P. J.; Knizia, G.; Manby, F. R.; Schütz, M., Molpro: A General-Purpose Quantum Chemistry Program Package. *WIREs Computational Molecular Science* **2012**, 2, 242–253.
42. Hampel, C.; Werner, H. J., Local Treatment of Electron Correlation in Coupled Cluster Theory. *The Journal of Chemical Physics* **1996**, 104, 6286–6297.
43. Schütz, M.; Werner, H.-J., Local Perturbative Triples Correction (T) with Linear Cost Scaling. *Chemical Physics Letters* **2000**, 318, 370–378.
44. Schütz, M., A New, Fast, Semi-direct Implementation of Linear Scaling Local Coupled Cluster Theory. *Physical Chemistry Chemical Physics* **2002**, 4, 3941–3947.
45. Adler, T. B.; Werner, H. J., An Explicitly Correlated Local Coupled Cluster Method for Calculations of Large Molecules Close to the Basis Set Limit. *Journal of Chemical Physics* **2011**, 135, 144117–144133.
46. Knizia, G.; Adler, T. B.; Werner, H. J., Simplified CCSD(T)-F12 Methods: Theory and Benchmarks. *Journal of Chemical Physics* **2009**, 130, 54104–54124.
47. Liebman, J. F.; Greenberg, A., A Survey of Strained Organic Molecules. *Chemical Reviews* **1976**, 76, 311–365.
48. Marson, C. M., New and Unusual Scaffolds in Medicinal Chemistry. *Chemical Society Reviews* **2011**, 40, 5514–5533.
49. Talele, T. T., The “Cyclopropyl Fragment” is a Versatile Player that Frequently Appears in Preclinical/Clinical Drug Molecules. *Journal of Medicinal Chemistry* **2016**, 59, 8712–8756.
50. Meanwell, N. A., Synopsis of Some Recent Tactical Application of Bioisosteres in Drug Design. *Journal of Medicinal Chemistry* **2011**, 54, 2529–2591.

51. Butcher, K. J.; Denton, S. M.; Field, S. E.; Gillmore, A. T.; Harbottle, G. W.; Howard, R. M.; Laity, D. A.; Ngono, C. J.; Pibworth, B. A., Convergent Asymmetric Synthesis of Two Complex TRPV1 Antagonists. *Organic Process Research & Development* **2011**, *15*, 1192–1200.
52. Micheli, F.; Cavanni, P.; Andreotti, D.; Arban, R.; Benedetti, R.; Bertani, B.; Bettati, M.; Bettelini, L.; Bonanomi, G.; Braggio, S.; Carletti, R.; Checchia, A.; Corsi, M.; Fazzolari, E.; Fontana, S.; Marchioro, C.; Merlo-Pich, E.; Negri, M.; Oliosi, B.; Ratti, E.; Read, K. D.; Roscic, M.; Sartori, I.; Spada, S.; Tedesco, G.; Tarsi, L.; Terreni, S.; Visentini, F.; Zocchi, A.; Zonzini, L.; Di Fabio, R., 6-(3,4-Dichlorophenyl)-1-[(Methoxy)methyl]-3-azabicyclo[4.1.0]heptane: A New Potent and Selective Triple Reuptake Inhibitor. *Journal of Medicinal Chemistry* **2010**, *53*, 4989–5001.
53. Zillhardt, M.; Park, S.-M.; Romero, I. L.; Sawada, K.; Montag, A.; Krausz, T.; Yamada, S. D.; Peter, M. E.; Lengyel, E., Foretinib (GSK1363089), an Orally Available Multikinase Inhibitor of c-Met and VEGFR-2, Blocks Proliferation, Induces Anoikis, and Impairs Ovarian Cancer Metastasis. *Clinical Cancer Research* **2011**, *17*, 4042–4051.
54. Mulvihill, M. J.; Cooke, A.; Rosenfeld-Franklin, M.; Buck, E.; Foreman, K.; Landfair, D.; O'Connor, M.; Pirritt, C.; Sun, Y.; Yao, Y.; Arnold, L. D.; Gibson, N. W.; Ji, Q. S., Discovery of OSI-906: A Selective and Orally Efficacious Dual Inhibitor of the IGF-1 Receptor and Insulin Receptor. *Future Med. Chem.* **2009**, *1*, 1153–1153.
55. Smolen, J. S.; Genovese, M. C.; Takeuchi, T.; Hyslop, D. L.; Macias, W. L.; Rooney, T.; Chen, L.; Dickson, C. L.; Camp, J. R.; Cardillo, T. E.; Ishii, T.; Winthrop, K. L., Safety Profile of Baricitinib in Patients with Active Rheumatoid Arthritis with Over 2 Years Median Time in Treatment. *The Journal of Rheumatology* **2019**, *46*, 7–18.

56. Salphati, L.; Heffron, T. P.; Alicke, B.; Nishimura, M.; Barck, K.; Carano, R. A.; Cheong, J.; Edgar, K. A.; Greve, J.; Kharbanda, S.; Koeppen, H.; Lau, S.; Lee, L. B.; Pang, J.; Plise, E. G.; Pokorny, J. L.; Reslan, H. B.; Sarkaria, J. N.; Wallin, J. J.; Zhang, X.; Gould, S. E.; Olivero, A. G.; Phillips, H. S., Targeting the PI3K Pathway in the Brain—Efficacy of a PI3K Inhibitor Optimized to Cross the Blood–Brain Barrier. *Clinical Cancer Research* **2012**, *18*, 6239–6239.
57. Hemming, D.; Fritzemeier, R.; Westcott, S. A.; Santos, W. L.; Steel, P. G., Copper-Boryl Mediated Organic Synthesis. *Chemical Society Reviews* **2018**, *47*, 7477–7494.
58. Leonori, D.; Aggarwal, V. K., Lithiation–Borylation Methodology and Its Application in Synthesis. *Accounts of Chemical Research* **2014**, *47*, 3174–3183.
59. Medina, J. M.; Kang, T.; Erbay, T. G.; Shao, H.; Gallego, G. M.; Yang, S.; Tran-Dubé, M.; Richardson, P. F.; Derosa, J.; Helsel, R. T.; Patman, R. L.; Wang, F.; Ashcroft, C. P.; Braganza, J. F.; McAlpine, I.; Liu, P.; Engle, K. M., Cu-Catalyzed Hydroboration of Benzyldenecyclopropanes: Reaction Optimization, (Hetero)Aryl Scope, and Origins of Pathway Selectivity. *ACS Catalysis* **2019**, *9*, 11130–11136.
60. Kang, T.; Erbay, T. G.; Xu, K. L.; Gallego, G. M.; Burtea, A.; Nair, S. K.; Patman, R. L.; Zhou, R.; Sutton, S. C.; McAlpine, I. J.; Liu, P.; Engle, K. M., Multifaceted Substrate–Ligand Interactions Promote the Copper-Catalyzed Hydroboration of Benzyldenecyclobutanes and Related Compounds. *ACS Catalysis* **2020**, *10*, 13075–13083.
61. Dang, L.; Zhao, H.; Lin, Z.; Marder, T. B., DFT Studies of Alkene Insertions into Cu–B Bonds in Copper(I) Boryl Complexes. *Organometallics* **2007**, *26*, 2824–2832.
62. Neel, A. J.; Hilton, M. J.; Sigman, M. S.; Toste, F. D., Exploiting Non-covalent π Interactions for Catalyst Design. *Nature* **2017**, *543*, 637–646.

63. Hopffgarten, M. v.; Frenking, G., Energy Decomposition Analysis. *WIREs Computational Molecular Science* **2012**, *2*, 43–62.
64. Zhao, L.; Hermann, M.; Schwarz, W. H. E.; Frenking, G., The Lewis Electron-Pair Bonding Model: Modern Energy Decomposition Analysis. *Nature Reviews Chemistry* **2019**, *3*, 48–63.
65. Ess, D. H.; Goddard, W. A.; Periana, R. A., Electrophilic, Ambiphilic, and Nucleophilic C–H Bond Activation: Understanding the Electronic Continuum of C–H Bond Activation Through Transition-State and Reaction Pathway Interaction Energy Decompositions. *Organometallics* **2010**, *29*, 6459–6472.
66. Raupach, M.; Tonner, R., A Periodic Energy Decomposition Analysis Method for the Investigation of Chemical Bonding in Extended Systems. *The Journal of Chemical Physics* **2015**, *142*, 194105–194119.
67. Phipps, M. J. S.; Fox, T.; Tautermann, C. S.; Skylaris, C.-K., Energy Decomposition Analysis Approaches and Their Evaluation on Prototypical Protein–Drug Interaction Patterns. *Chemical Society Reviews* **2015**, *44*, 3177–3211.
68. Lu, G.; Liu, R. Y.; Yang, Y.; Fang, C.; Lambrecht, D. S.; Buchwald, S. L.; Liu, P., Ligand–Substrate Dispersion Facilitates the Copper-Catalyzed Hydroamination of Unactivated Olefins. *Journal of the American Chemical Society* **2017**, *139*, 16548–16555.
69. Thomas, A. A.; Speck, K.; Kevlishvili, I.; Lu, Z.; Liu, P.; Buchwald, S. L., Mechanistically Guided Design of Ligands That Significantly Improve the Efficiency of CuH-Catalyzed Hydroamination Reactions. *Journal of the American Chemical Society* **2018**, *140*, 13976–13984.
70. Roy, L. E.; Hay, P. J.; Martin, R. L., Revised Basis Sets for the LANL Effective Core Potentials. *Journal of Chemical Theory and Computation* **2008**, *4*, 1029–1031.

71. Shao, Y.; Gan, Z.; Epifanovsky, E.; Gilbert, A. T. B.; Wormit, M.; Kussmann, J.; Lange, A. W.; Behn, A.; Deng, J.; Feng, X.; Ghosh, D.; Goldey, M.; Horn, P. R.; Jacobson, L. D.; Kaliman, I.; Khaliullin, R. Z.; Kuś, T.; Landau, A.; Liu, J.; Proynov, E. I.; Rhee, Y. M.; Richard, R. M.; Rohrdanz, M. A.; Steele, R. P.; Sundstrom, E. J.; Iii, H. L. W.; Zimmerman, P. M.; Zuev, D.; Albrecht, B.; Alguire, E.; Austin, B.; Beran, G. J. O.; Bernard, Y. A.; Berquist, E.; Brandhorst, K.; Bravaya, K. B.; Brown, S. T.; Casanova, D.; Chang, C.-M.; Chen, Y.; Chien, S. H.; Closser, K. D.; Crittenden, D. L.; Diedenhofen, M.; Jr, R. A. D.; Do, H.; Dutoi, A. D.; Edgar, R. G.; Fatehi, S.; Fusti-Molnar, L.; Ghysels, A.; Golubeva-Zadorozhnaya, A.; Gomes, J.; Hanson-Heine, M. W. D.; Harbach, P. H. P.; Hauser, A. W.; Hohenstein, E. G.; Holden, Z. C.; Jagau, T.-C.; Ji, H.; Kaduk, B.; Khistyayev, K.; Kim, J.; Kim, J.; King, R. A.; Klunzinger, P.; Kosenkov, D.; Kowalczyk, T.; Krauter, C. M.; Lao, K. U.; Laurent, A. D.; Lawler, K. V.; Levchenko, S. V.; Lin, C. Y.; Liu, F.; Livshits, E.; Lochan, R. C.; Luenser, A.; Manohar, P.; Manzer, S. F.; Mao, S.-P.; Mardirossian, N.; Marenich, A. V.; Maurer, S. A.; Mayhall, N. J.; Neuscamman, E.; Oana, C. M.; Olivares-Amaya, R.; O'Neill, D. P.; Parkhill, J. A.; Perrine, T. M.; Peverati, R.; Prociuk, A.; Rehn, D. R.; Rosta, E.; Russ, N. J.; Sharada, S. M.; Sharma, S.; Small, D. W.; Sodt, A.; Stein, T.; Stück, D.; Su, Y.-C.; Thom, A. J. W.; Tsuchimochi, T.; Vanovschi, V.; Vogt, L.; Vydrov, O.; Wang, T.; Watson, M. A.; Wenzel, J.; White, A.; Williams, C. F.; Yang, J.; Yeganeh, S.; Yost, S. R.; You, Z.-Q.; Zhang, I. Y.; Zhang, X.; Zhao, Y.; Brooks, B. R.; Chan, G. K. L.; Chipman, D. M.; Cramer, C. J.; Iii, W. A. G.; Gordon, M. S.; Hehre, W. J.; Klamt, A.; Iii, H. F. S.; Schmidt, M. W.; Sherrill, C. D.; Truhlar, D. G.; Warshel, A.; Xu, X.; Aspuru-Guzik, A.; Baer, R.; Bell, A. T.; Besley, N. A.; Chai, J.-D.; Dreuw, A.; Dunietz, B. D.; Furlani, T. R.; Gwaltney, S. R.; Hsu, C.-P.; Jung, Y.; Kong, J.; Lambrecht, D. S.; Liang, W.; Ochsenfeld, C.; Rassolov, V. A.; Slipchenko, L. V.; Subotnik, J. E.; Voorhis, T. V.; Herbert, J. M.; Krylov, A. I.; Gill, P. M. W.; Head-Gordon, M., *Advances in*

Molecular Quantum Chemistry Contained in the Q-Chem 4 Program Package. *Molecular Physics* **2015**, *113*, 184–215.

72. Greiser, T.; Weiss, E., Kristallstruktur des Kupfer(I)-tert-butoxids, $[(CH_3)_3COCu]_4$. *Chemische Berichte* **1976**, *109*, 3142–3146.

73. Wheeler, S. E.; Houk, K. N., Origin of Substituent Effects in Edge-to-Face Aryl–Aryl Interactions. *Molecular Physics* **2009**, *107*, 749–760.

74. Brown, J. M., Directed Homogeneous Hydrogenation. *Angewandte Chemie International Edition in English* **1987**, *26*, 190–203.

75. Hoveyda, A. H.; Evans, D. A.; Fu, G. C., Substrate-Directable Chemical Reactions. *Chemical Reviews* **1993**, *93*, 1307–1370.

76. Oestreich, M., Directed Mizoroki–Heck Reactions. In *Directed Metallation*, Chatani, N., Ed. Springer Berlin Heidelberg: Berlin, Heidelberg, **2007**, 169–192.

77. Oestreich, M., Neighbouring-Group Effects in Heck Reactions. *European Journal of Organic Chemistry* **2005**, *2005*, 783–792.

78. Rousseau, G.; Breit, B., Removable Directing Groups in Organic Synthesis and Catalysis. *Angewandte Chemie International Edition* **2011**, *50*, 2450–2494.

79. Derosa, J.; Tran, V. T.; Boulous, M. N.; Chen, J. S.; Engle, K. M., Nickel-Catalyzed β,γ -Dicarbofunctionalization of Alkenyl Carbonyl Compounds via Conjunctive Cross-Coupling. *Journal of the American Chemical Society* **2017**, *139*, 10657–10660.

80. Wang, C.; Xiao, G.; Guo, T.; Ding, Y.; Wu, X.; Loh, T.-P., Palladium-Catalyzed Regiocontrollable Reductive Heck Reaction of Unactivated Aliphatic Alkenes. *Journal of the American Chemical Society* **2018**, *140*, 9332–9336.

81. Wang, H.; Bai, Z.; Jiao, T.; Deng, Z.; Tong, H.; He, G.; Peng, Q.; Chen, G., Palladium-Catalyzed Amide-Directed Enantioselective Hydrocarbofunctionalization of Unactivated Alkenes Using a Chiral Monodentate Oxazoline Ligand. *Journal of the American Chemical Society* **2018**, *140*, 3542–3546.
82. Liu, Z.; Li, X.; Zeng, T.; Engle, K. M., Directed, Palladium(II)-Catalyzed Enantioselective *anti*-Carboboration of Alkenyl Carbonyl Compounds. *ACS Catalysis* **2019**, *9*, 3260–3265.
83. Bai, Z.; Zheng, S.; Bai, Z.; Song, F.; Wang, H.; Peng, Q.; Chen, G.; He, G., Palladium-Catalyzed Amide-Directed Enantioselective Carboboration of Unactivated Alkenes Using a Chiral Monodentate Oxazoline Ligand. *ACS Catalysis* **2019**, *9*, 6502–6509.
84. Liu, Z.; Chen, J.; Lu, H.-X.; Li, X.; Gao, Y.; Coombs, J. R.; Goldfogel, M. J.; Engle, K. M., Palladium(0)-Catalyzed Directed *syn*-1,2-Carboboration and -Silylation: Alkene Scope, Applications in Dearomatization, and Stereocontrol by a Chiral Auxiliary. *Angewandte Chemie International Edition* **2019**, *58*, 17068–17073.
85. Seayad, J.; List, B., Asymmetric Organocatalysis. *Organic & Biomolecular Chemistry* **2005**, *3*, 719–724.
86. Bertelsen, S.; Jørgensen, K. A., Organocatalysis—After the Gold Rush. *Chemical Society Reviews* **2009**, *38*, 2178–2189.
87. Allen, A. E.; MacMillan, D. W. C., Synergistic Catalysis: A Powerful Synthetic Strategy for New Reaction Development. *Chemical Science* **2012**, *3*, 633–658.
88. Chen, D.-F.; Han, Z.-Y.; Zhou, X.-L.; Gong, L.-Z., Asymmetric Organocatalysis Combined with Metal Catalysis: Concept, Proof of Concept, and Beyond. *Accounts of Chemical Research* **2014**, *47*, 2365–2377.

89. Afewerki, S.; Córdova, A., Combinations of Aminocatalysts and Metal Catalysts: A Powerful Cooperative Approach in Selective Organic Synthesis. *Chemical Reviews* **2016**, *116*, 13512–13570.
90. Qin, Y.; Zhu, L.; Luo, S., Organocatalysis in Inert C–H Bond Functionalization. *Chemical Reviews* **2017**, *117*, 9433–9520.
91. Breit, B., Controlling Stereoselectivity with the Aid of a Reagent-Directing Group: Hydroformylation, Cuprate Addition, and Domino Reaction Sequences. *Chemistry – A European Journal* **2000**, *6*, 1519–1524.
92. Colby, D. A.; Bergman, R. G.; Ellman, J. A., Rhodium-Catalyzed C–C Bond Formation via Heteroatom-Directed C–H Bond Activation. *Chemical Reviews* **2010**, *110*, 624–655.
93. Mo, F.; Dong, G., Regioselective Ketone α -Alkylation with Simple Olefins via Dual Activation. *Science* **2014**, *345*, 68–72.
94. Dong, Z.; Ren, Z.; Thompson, S. J.; Xu, Y.; Dong, G., Transition-Metal-Catalyzed C–H Alkylation Using Alkenes. *Chemical Reviews* **2017**, *117*, 9333–9403.
95. Gandeepan, P.; Ackermann, L., Transient Directing Groups for Transformative C–H Activation by Synergistic Metal Catalysis. *Chem* **2018**, *4*, 199–222.
96. St John-Campbell, S.; Bull, J. A., Transient Imines as ‘Next Generation’ Directing Groups for the Catalytic Functionalisation of C–H Bonds in a Single Operation. *Organic & Biomolecular Chemistry* **2018**, *16*, 4582–4595.
97. Li, B.; Seth, K.; Niu, B.; Pan, L.; Yang, H.; Ge, H., Transient-Ligand-Enabled *ortho*-Arylation of Five-Membered Heterocycles: Facile Access to Mechanochromic Materials. *Angewandte Chemie International Edition* **2018**, *57*, 3401–3405.

98. Li, B.; Lawrence, B.; Li, G.; Ge, H., Ligand-Controlled Direct γ -C–H Arylation of Aldehydes. *Angewandte Chemie International Edition* **2020**, *59*, 3078–3082.
99. Liu, Z.; Wang, Y.; Wang, Z.; Zeng, T.; Liu, P.; Engle, K. M., Catalytic Intermolecular Carboamination of Unactivated Alkenes via Directed Aminopalladation. *Journal of the American Chemical Society* **2017**, *139*, 11261–11270.
100. Watzke, A.; Wilson, R. M.; O'Malley, S. J.; Bergman, R. G.; Ellman, J. A., Asymmetric Intramolecular Alkylation of Chiral Aromatic Imines via Catalytic C–H Bond Activation. *Synlett* **2007**, *15*, 2383–2389.
101. Beletskiy, E. V.; Sudheer, C.; Douglas, C. J., Cooperative Catalysis Approach to Intramolecular Hydroacylation. *The Journal of Organic Chemistry* **2012**, *77*, 5884–5893.
102. Worthy, A. D.; Joe, C. L.; Lightburn, T. E.; Tan, K. L., Application of a Chiral Scaffolding Ligand in Catalytic Enantioselective Hydroformylation. *Journal of the American Chemical Society* **2010**, *132*, 14757–14759.
103. Zhang, F.-L.; Hong, K.; Li, T.-J.; Park, H.; Yu, J.-Q., Functionalization of C(sp³)–H bonds Using a Transient Directing Group. *Science* **2016**, *351*, 252–256.
104. Park, H.; Verma, P.; Hong, K.; Yu, J. Q., Controlling Pd(IV) Reductive Elimination Pathways Enables Pd(II)-Catalysed Enantioselective C(sp³)–H Fluorination. *Nature Chemistry* **2018**, *10*, 755–762.
105. Liu, M.; Yang, P.; Karunananda, M. K.; Wang, Y.; Liu, P.; Engle, K. M., C(alkenyl)–H Activation via Six-Membered Palladacycles: Catalytic 1,3-Diene Synthesis. *Journal of the American Chemical Society* **2018**, *140*, 5805–5813.

106. Yang, Y. F.; Hong, X.; Yu, J. Q.; Houk, K. N., Experimental-Computational Synergy for Selective Pd(II)-Catalyzed C–H Activation of Aryl and Alkyl Groups. *Accounts of Chemical Research* **2017**, *50*, 2853–2860.
107. Heck, R. F., Palladium-Catalyzed Reactions of Organic Halides with Olefins. *Accounts of Chemical Research* **1979**, *12*, 146–151.
108. Beletskaya, I. P.; Cheprakov, A. V., The Heck Reaction as a Sharpening Stone of Palladium Catalysis. *Chemical Reviews* **2000**, *100*, 3009–3066.
109. Johansson Seechurn, C. C. C.; Kitching, M. O.; Colacot, T. J.; Snieckus, V., Palladium-Catalyzed Cross-Coupling: A Historical Contextual Perspective to the 2010 Nobel Prize. *Angewandte Chemie International Edition* **2012**, *51*, 5062–5085.
110. Dounay, A. B.; Overman, L. E., The Asymmetric Intramolecular Heck Reaction in Natural Product Total Synthesis. *Chemical Reviews* **2003**, *103*, 2945–2964.
111. Mc Cartney, D.; Guiry, P. J., The Asymmetric Heck and Related Reactions. *Chemical Society Reviews* **2011**, *40*, 5122–5150.
112. Gurak, J. A.; Engle, K. M., Practical Intermolecular Hydroarylation of Diverse Alkenes via Reductive Heck Coupling. *ACS Catalysis* **2018**, *8*, 8987–8992.
113. Oxtoby, L. J.; Gurak, J. A.; Wisniewski, S. R.; Eastgate, M. D.; Engle, K. M., Palladium-Catalyzed Reductive Heck Coupling of Alkenes. *Trends in Chemistry* **2019**, *1*, 572–587.
114. Podhajsky, S. M.; Iwai, Y.; Cook-Sneathen, A.; Sigman, M. S., Asymmetric Palladium-Catalyzed Hydroarylation of Styrenes and Dienes. *Tetrahedron* **2011**, *67*, 4435–4441.
115. Friis, S. D.; Pirnot, M. T.; Buchwald, S. L., Asymmetric Hydroarylation of Vinylarenes Using a Synergistic Combination of CuH and Pd Catalysis. *Journal of the American Chemical Society* **2016**, *138*, 8372–8375.

116. Grélaud, S.; Cooper, P.; Feron, L. J.; Bower, J. F., Branch-Selective and Enantioselective Iridium-Catalyzed Alkene Hydroarylation via Anilide-Directed C–H Oxidative Addition. *Journal of the American Chemical Society* **2018**, *140*, 9351–9356.
117. Chen, Y.-G.; Shuai, B.; Xu, X.-T.; Li, Y.-Q.; Yang, Q.-L.; Qiu, H.; Zhang, K.; Fang, P.; Mei, T.-S., Nickel-Catalyzed Enantioselective Hydroarylation and Hydroalkenylation of Styrenes. *Journal of the American Chemical Society* **2019**, *141*, 3395–3399.
118. Saxena, A.; Lam, H. W., Enantioselective Rhodium-Catalyzed Arylation of Electron-Deficient Alkenylarenes. *Chemical Science* **2011**, *2*, 2326–2331.
119. Roy, I. D.; Burns, A. R.; Pattison, G.; Michel, B.; Parker, A. J.; Lam, H. W., A Second-Generation Ligand for the Enantioselective Rhodium-Catalyzed Addition of Arylboronic Acids to Alkenylarenes. *Chemical Communications* **2014**, *50*, 2865–2868.
120. Chen, Z.-M.; Hilton, M. J.; Sigman, M. S., Palladium-Catalyzed Enantioselective Redox-Relay Heck Arylation of 1,1-Disubstituted Homoallylic Alcohols. *Journal of the American Chemical Society* **2016**, *138*, 11461–11464.
121. Yang, Q.; Wang, Y.; Luo, S.; Wang, J., Kinetic Resolution and Dynamic Kinetic Resolution of Chromene by Rhodium-Catalyzed Asymmetric Hydroarylation. *Angewandte Chemie International Edition* **2019**, *58*, 5343–5347.
122. Cherney, A. H.; Kadunce, N. T.; Reisman, S. E., Enantioselective and Enantiospecific Transition-Metal-Catalyzed Cross-Coupling Reactions of Organometallic Reagents to Construct C–C Bonds. *Chemical Reviews* **2015**, *115*, 9587–9652.
123. Rygus, J. P. G.; Crudden, C. M., Enantiospecific and Iterative Suzuki–Miyaura Cross-Couplings. *Journal of the American Chemical Society* **2017**, *139*, 18124–18137.

124. Oxtoby, L. J.; Li, Z. Q.; Tran, V. T.; Erbay, T. G.; Deng, R.; Liu, P.; Engle, K. M., A Transient-Directing-Group Strategy Enables Enantioselective Reductive Heck Hydroarylation of Alkenes. *Angewandte Chemie - International Edition* **2020**, *59*, 8885–8890.
125. Xu, L.; Hilton, M. J.; Zhang, X.; Norrby, P.-O.; Wu, Y.-D.; Sigman, M. S.; Wiest, O., Mechanism, Reactivity, and Selectivity in Palladium-Catalyzed Redox-Relay Heck Arylations of Alkenyl Alcohols. *Journal of the American Chemical Society* **2014**, *136*, 1960–1967.
126. Zhonglin, L.; Lucas, O.; Mingyu, L.; Zi-Qi, L.; Van, T.; Yang, G.; Keary, E., A Transient Directing Group Strategy Enables Enantioselective Multicomponent Organofluorine Synthesis. *Journal of the American Chemical Society* **2021**, *143*, 8962–8969.